The background of the cover is a scanning electron micrograph (SEM) showing a highly porous, interconnected network of fibers or membranes. The structure consists of numerous small, rounded, interconnected voids or cells, creating a complex, sponge-like appearance. The lighting highlights the texture and depth of the porous structure.

Zero-Gap Seawater Electrolysis Flow Cell with Forward Osmosis-Based In-Situ Water Purification

MSc SET Thesis Report

Florian B. J. Popkes

Zero-Gap Seawater Electrolysis Flow Cell with Forward Osmosis-Based In-Situ Water Purification

MSc SET Thesis Report

by

Florian B. J. Popkes

to obtain the degree of Master of Science
at the Delft University of Technology,
to be defended publicly on Tuesday July 9, 2024 at 09:30 am.

Student number: 5731305
Project duration: 13.11.2023 - 09.07.2024
Thesis committee: Dr. ir. David Vermaas, TU Delft, supervisor
Prof. dr. ir. Jules van Lier, TU Delft
Prof. dr. ir. Ruud van Ommen, TU Delft

An electronic version of this thesis is available at <http://repository.tudelft.nl/>.

Abstract

As part of the global energy transition, large amounts of hydrogen will be needed to provide fuel for heavy-duty transport, heat for industrial processes, and as a feedstock in chemical processes. To be environmentally sustainable, this hydrogen has to be generated using electricity via water electrolysis. With an increase in hydrogen production, however, the additional demand for freshwater in water electrolysis will start to compete with other freshwater consumers, especially humans. One approach to lessen the freshwater impact of water electrolysis is to use seawater as the process feed and perform in-situ water purification. Among others, this purification can be done by using forward osmosis membranes. However, previous research on this topic has only been performed at low current densities, while simultaneously demonstrating high cell overpotentials.

Therefore, the overall aim of this thesis is to quantify the attainable current density of the forward osmosis-based purification method, and to optimise the cell performance through use of a zero-gap design. In addition, an evaluation of performance and material degradation is pursued. To this end, tests were conducted to quantify the water flux over the forward osmosis membrane within the given system. Next, a variety of long-term electrochemical tests were performed, both with and without water purification, and at different current densities. Furthermore, the cell voltages before and after testing were broken down into anode, cathode, and membrane contributions to gauge performance degradation and locate its origins. Finally, a variety of testing methods such as SEM, EDX, and XPS were used to evaluate the observed material and performance degradation and its causes.

The maximum current density attainable within the designed system is found to amount to 62.39 mA/cm². Furthermore, an initial performance improvement is found for the zero-gap cell design. This performance improvement is attributed to lower concentration and bubble overpotentials. However, the cell design exhibits strong material and performance degradation under all investigated testing parameters. The performance degradation is caused by increasing anode and membrane overpotentials. The anode overpotential increase is hypothesised to be due to the dissolution of a catalytically-active iron- and nickel-rich anode top layer. The membrane overpotential is hypothesised to be due to membrane blockage by material deposits, and sodium-proton substitution in the membrane. In contrast, stable, or even improving, cathode overpotentials are found. This observation is attributed to the formation of catalytically superior metal phosphates and nickel hydroxide on the cathode surface. Lastly, the root cause of all degradative processes is found to be the use of a selective membrane, which enables a gradual acidification of the anolyte and thus creates a highly corrosive environment at the stainless steel anode.

The results of this thesis allow for a better understanding of the inherent limitations connected to the use of FO membranes in electrolysis cells. It also offers a wide range of opportunities for improving the system and cell design in future research. Specifically, it enables a more careful membrane selection for future cell designs. By highlighting the limited achievable water influx with the given system, it also emphasises the need for larger FO membranes, and thus a different system architecture, or alternatively the need for a switch to a different draw solution or electrolyte.

Acknowledgements

First and foremost, I would like to thank my parents for their endless love and support. I feel thankful every day to have been born into such a loving and supportive family. This acknowledgement also includes my two sisters, both of which have set brilliant examples with their academic careers that I do my best to live up to.

Second, I would like to thank my partner, Caren, for always supporting and inspiring me. This thesis truly would not have been possible without you. I love you and cannot wait to start this next phase of our lives together.

Third, I would like to acknowledge every teacher, professor, mentor, and friend who has helped me throughout my academic career by providing either emotional support or professional advice. There are too many to name individually, but I hope all concerned feel spoken to when reading this.

Lastly, I would like to thank Ai-Yu, my daily supervisor for the past eight months. Working with you has truly been a pleasure, both on a personal and professional level. I could not have wished for a better supervisor and am excited to see what the future holds for you. This acknowledgement also includes Professor David Vermaas, who enabled this research project in the first place, and provided key insights and ideas throughout.

Contents

Nomenclature	viii
1 Introduction	1
1.1 Conventional Water Electrolysis	1
1.1.1 Theoretical Background	1
1.1.2 Alkaline Water Electrolysis	2
1.1.3 Proton-Exchange Membrane Electrolysis	3
1.2 Direct Seawater Electrolysis	4
1.2.1 Fundamental Challenges	5
1.2.2 PTFE Membranes	6
1.2.3 Seawater Vapour	7
1.2.4 Bipolar Membranes	8
1.3 Forward Osmosis	9
1.3.1 Concentration Polarisation	10
1.3.2 Forward Osmosis-Based Direct Seawater Electrolysis	11
1.4 Research Questions	12
2 Methods and Methodology	14
2.1 Test Cell Design	15
2.1.1 Water Mass Flux Test Cell	15
2.1.2 Electrolysis Cell	16
2.2 Water Mass Flux Tests	19
2.3 Galvanostatic Electrolysis Tests	20
2.3.1 Blank Cell Tests	22
2.3.2 Combined Cell Tests	22
2.4 Solution Analysis	23
2.4.1 Conductivity, pH & Weight Measurements	23
2.4.2 Anion Chromatography	24
2.5 Surface Analysis	24
2.5.1 SEM and EDX Analysis	24
2.5.2 XPS Analysis	25
3 Results and Discussion	26
3.1 Water Mass Flux Tests	26
3.2 Galvanostatic Electrolysis Tests	28
3.2.1 Continuous Cell Voltage Measurements	29
3.2.2 Cell Voltage Breakdown Measurements	30
3.3 Solution Investigation	33
3.3.1 Anolyte	34
3.3.2 Catholyte	35
3.3.3 Artificial Seawater	37
3.4 Surface Analysis	38
3.4.1 Anode	38
3.4.2 Cathode	43
3.4.3 Nafion Membrane	48
3.4.4 FO Membrane	50
3.4.5 XPS	51
3.5 Combined Results Analysis	55
4 Conclusion	56

5 Recommendations	58
5.1 Hypotheses Validation	58
5.2 Cell and System Design	59
References	61
A Pourbaix Diagrams	65
B Testing Protocols	66
C Testing Solutions	67
D SEM/EDX Locations	70
E Supplementary Information	74

List of Figures

1.1	Water splitting Pourbaix diagram [8]	2
1.2	Alkaline water electrolyser [12]	3
1.3	Proton-exchange membrane electrolyser [12]	4
1.4	Chloride chemistry pourbaix diagram in artificial seawater [21]	5
1.5	Electrolysis cell using in-situ PTFE-based water purification [25]	6
1.6	PEM electrolyser using seawater vapour [26]	7
1.7	BPM-based seawater electrolysis cell [29]	8
1.8	The forward osmosis process [30]	9
1.9	Internal and external concentration polarisation in an asymmetric forward osmosis membrane [30]	10
1.10	Forward Osmosis-Based Direct Seawater Electrolysis Cell [5]	11
2.1	Testing overview	14
2.2	The water mass flux test cell	15
2.3	The electrolysis cell	16
2.4	Cell part visualisation: (a) Flow Field with RHE; (b) Electrode with outer contact area for electrical connection	17
2.5	Volcano plots: (a) Various catalysts for HER in acidic media [41]; (b) Various catalysts for OER in acidic media [42]	18
2.6	The setup used for all evaporation and water mass flux tests	19
2.7	Galvanostatic electrolysis testing protocol	21
2.8	Blank Cell Electrolysis Test Setup	22
2.9	Combined cell test setup: (a) Overview of complete test setup including pump and liquids; (b) Top view of water mass flux cell and electrolysis cell in serial connection	23
3.1	Water mass flux test results: a) Average draw and feed solution weight changes; b) Chloride concentration in the draw solution before and after testing	26
3.2	Used FO membrane water mass flux test results: a) Draw and feed solution weight changes; b) Chloride concentration in the draw solution before and after testing	27
3.3	Water mass flux test results with pH 3 draw solution: a) Draw and feed solution weight changes; b) Chloride concentration in the draw solution before and after testing	28
3.4	Continuous cell voltage measurement results	29
3.5	Initial and final voltage breakdown of all tests	31
3.6	Blank anode shown in a); Anodes after testing: b) Cell without seawater at 25 mA/cm ² ; c) Cell with seawater at 25 mA/cm ² ; d) Cell without seawater at 62.39 mA/cm ² ; e) Cell with seawater at 62.39 mA/cm ²	38
3.7	SEM results of the anode location 'no corrosion'	40
3.8	SEM results of the anode location 'strong corrosion'	41
3.9	SEM results of the anode location 'brown precipitate (anode)'	42
3.10	Blank cathode shown in a); Cathodes after testing: a) Cell without seawater at 25 mA/cm ² ; b) Cell with seawater at 25 mA/cm ² ; c) Cell without seawater at 62.39 mA/cm ² ; d) Cell with seawater at 62.39 mA/cm ²	43
3.11	SEM results of the cathode location 'light grey'	44
3.12	SEM results of the cathode location 'black'	45
3.13	SEM results of the cathode location 'light green'	46
3.14	SEM results of the cathode location 'brown precipitate (cathode)'	47
3.15	Pristine Nafion membrane shown in a); Nafion membranes after testing: b) Cell without seawater at 25 mA/cm ² ; c) Cell with seawater at 25 mA/cm ² ; d) Cell without seawater at 62.39 mA/cm ² ; e) Cell with seawater at 62.39 mA/cm ²	48

3.16 SEM results of the investigated Nafion membranes	49
3.17 Blank FO membrane shown in a); FO membranes after testing: b) Cell with seawater at 25 mA/cm ² ; c) Cell with seawater at 62.39 mA/cm ²	50
3.18 SEM and EDX results of the investigated FO membrane	51
3.19 Selected XPS data from the blank anode (green) and CwS HC (red)	52
3.20 Selected XPS data from the blank cathode (green) and CwS LC (red)	53
3.21 Selected XPS data from the blank cathode (green) and CwS HC (red)	54
3.22 The degradation cycle governing the corrosion processes	55
A.1 Pourbaix diagrams of: a) Nickel [71]; b) Iron [72]; c) Chromium [73]. The vertical red bars mark the lowest and highest pH values observed in the anolyte and catholyte, respectively. 65	65
B.1 Water mass flux testing protocol	66
B.2 Galvanostatic electrolysis testing protocol	66
C.1 CwoS LC solutions after 40 h test	67
C.2 CwoS HC solutions after 40 h test	68
C.3 CwS LC solutions after 40 h test	68
C.4 CwS HC solutions after 40 h test	69
D.1 Blank anode and cathode SEM/EDX locations	70
D.2 SEM/EDX locations 'no corrosion' (only the spots marked a blue rectangle)	70
D.3 SEM/EDX locations 'strong corrosion' (only the spots marked a blue rectangle)	71
D.4 SEM/EDX locations 'brown precipitate (anode)' (only the spots marked a blue rectangle)	71
D.5 Cathode SEM/EDX location 'light grey' (only the spots marked a blue rectangle)	71
D.6 Cathode SEM/EDX location 'black'	72
D.7 Cathode SEM/EDX location 'light green'	72
D.8 SEM/EDX locations 'brown precipitate (cathode)' (only the spots marked a blue rectangle) 73	73
E.1 316L stainless steel surface composition [43]	74
E.2 Transition metal ion colours [74]	75

List of Tables

2.1 Galvanostatic testing overview	20
3.1 Anolyte solutions before and after testing	34
3.2 Catholyte solutions before and after testing	36
3.3 Artificial seawater solutions before and after testing	37
3.4 EDX results of the anode location 'no corrosion'	40
3.5 EDX results of the anode location 'strong corrosion'	41
3.6 EDX results of the anode location 'brown precipitate (anode)'	43
3.7 EDX results of the cathode location 'light grey'	45
3.8 EDX results of the cathode location 'black'	46
3.9 EDX results of the cathode location 'light green'	47
3.10 EDX results of the cathode location 'brown precipitate (cathode)'	48
3.11 EDX results of investigated Nafion membranes	49

Nomenclature

Abbreviations

Abbreviation	Definition
AEL	Anion Exchange Layer
AWE	Alkaline Water Electrolysis
BPM	Bipolar Membrane
CE	Counter Electrode
CEL	Cation Exchange Layer
CER	Chlorine Evolution Reaction
CTA	Cellulose Triacetate
DI	Deionised Water
DSE	Direct Seawater Electrolysis
ECP	External Concentration Polarisation
ECSA	Electrochemically Active Surface Area
EPDM	Ethylene Propylene Diene Monomer
EDX	Energy Dispersive X-Ray Analysis
FO	Forward Osmosis
HER	Hydrogen Evolution Reaction
ICP	Internal Concentration Polarisation
KOH	Potassium Hydroxide
OER	Oxygen Evolution Reaction
PEEK	Polyether Ether Ketone
PEM	Proton Exchange Membrane
PEMWE	Proton Exchange Membrane Water Electrolysis
PtC	Platinum on Carbon
PTFE	Polytetrafluoroethylene
PTL	Porous Transport Layer
RE	Reference Electrode
RHE	Reversible Hydrogen Electrode
S	Sense Electrode
SEM	Scanning Electron Microscopy
SS	Stainless Steel
WD	Water Dissociation
WE	Working Electrode
XPS	X-Ray Photoelectron Spectroscopy

Symbols

Symbol	Definition	Unit
A	Surface area	[cm ²]
F	Faraday constant	[C/mol]
i	Current density	[A/cm ²]
I	Van't Hoff factor	[-]
M	Molarity	[mol/L]
R	Gas constant	[J/(mol*K)]
T	Temperature	[K]

Symbol	Definition	Unit
U	Voltage	[V]
η	Overpotential	[V]
Π	Osmotic pressure	[Pa]

1

Introduction

In recent decades, global warming has reached unprecedented levels, with the average global surface temperature increase already at 1.1°C [1]. In response to these developments, a global energy transition has begun, which aims to reduce global emissions and thus limit warming levels. This transition is centered around the electrification of most processes, powered by renewable energy from sources such as wind and solar [2]. However, there are a variety of sectors that continue to be difficult to electrify. In most of these sectors, such as for the provision of industrial heat or chemical feedstocks, hydrogen has emerged as a promising solution [3]. In order to be generated sustainably, this hydrogen has to be produced by splitting water via electrolysis. In total, the demand for hydrogen after a full energy transition has been set at 2.3 Gt per year, corresponding to a total freshwater need of 20.5 Gt per year for hydrogen production alone [4]. This additional freshwater demand is set to put significant strain on freshwater resources, especially in regions already suffering from regular droughts. Thus, research increasingly focuses on switching to seawater as a feed in water electrolysis, due to its ubiquity. One of the proposed solutions for this challenge is to combine water electrolysis with in-situ seawater purification using forward osmosis membranes. Previous research on the subject has proved promising [5]. However, the development of FO-based electrolysis cells is still at the very beginning, with a variety of research gaps that limit the improvement of the underlying system. Therefore, this thesis aims to fill some of the research gaps on the topic.

This chapter contains all relevant background information needed to understand the scientific context of the research topic and its main mechanisms. First, subsection 1.1 provides information on conventional water electrolysis methods and their theoretical foundation. Next, subsection 1.2 specifically focuses on currently researched direct seawater electrolysis methods. Afterwards, subsection 1.3 singles out the forward-osmosis process used for the in-situ water purification investigated in this thesis. This subsection also includes an in-depth introduction of the current state-of-the-art forward osmosis-based electrolysis cell. Finally, the motivation and aims of this research project, combined with the research questions derived from them, are presented in subsection 1.4.

1.1. Conventional Water Electrolysis

This section starts by introducing the underlying chemical reactions governing water electrolysis: the hydrogen evolution reaction (HER) and the oxygen evolution reaction (OER). Afterwards, a description of the two most widespread types of water electrolyzers is given, starting with alkaline water electrolyzers (AWE), followed by proton exchange membrane water electrolyzers (PEM). To this end, the basic design of the electrolyzers is shown, and their central advantages and drawbacks discussed.

1.1.1. Theoretical Background

Water electrolysis describes the process in which water is split into hydrogen and oxygen by applying electrical energy [6]. The electrical energy required for the process to take place is provided by applying an external voltage that must exceed the equilibrium voltage of water splitting. Generally, this standard equilibrium voltage of water splitting amounts to 1.229 V at standard conditions [7]. The two reactions

responsible for the generation of hydrogen and oxygen under application of this potential are commonly referred to as the hydrogen evolution reaction and oxygen evolution reaction, respectively. The exact distribution of electrode potentials required for either reaction to take place depends, among other factors, on temperature and pH of the electrolyte. Figure 1.1 shows the evolution of the HER and OER electrode potentials at different pH values for a fixed temperature of 298 K in a Pourbaix diagram.

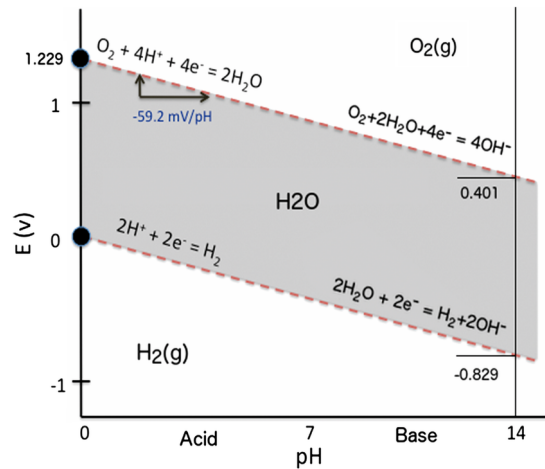
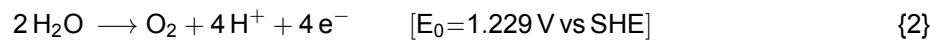


Figure 1.1: Water splitting Pourbaix diagram [8]

At the far left of the Pourbaix diagram, approaching a pH of zero, the HER is described by the following process:

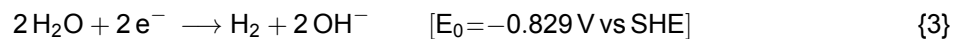


The complementary OER is governed by the mechanism given below [9]:



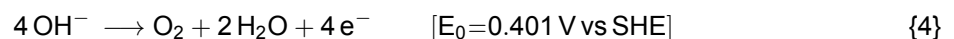
The OER mechanism under acidic conditions is challenging due to its generation of protons. Thus, the reaction leads to a localised acid-shift at the anode. Furthermore, the oxygen evolution reaction based on water oxidation as shown in reaction 2 has been found to also dominate under pH-neutral conditions [10].

In contrast, when following the Pourbaix diagram to the far right side, or approaching extremely alkaline conditions, the HER switches to a different mechanism:



Similar to the acid-shift observed at the anode under reaction 2, the alkaline HER is challenging due to its generation of hydroxide ions, leading to an alkali-shift close to the cathode. In neutral conditions, the HER is dominated by the reduction of water shown as shown in reaction 3 [10].

Finally, under alkaline conditions, the OER proceeds as follows [9]:



1.1.2. Alkaline Water Electrolysis

Alkaline water electrolysis constitutes the most mature type of water electrolyser [7]. The technology has been in use for more than 120 years and has proven to be safe and reliable, with electrolyser life

spans reaching up to fifteen years [11]. In figure 1.2, the basic layout of an alkaline water electrolyser is shown.

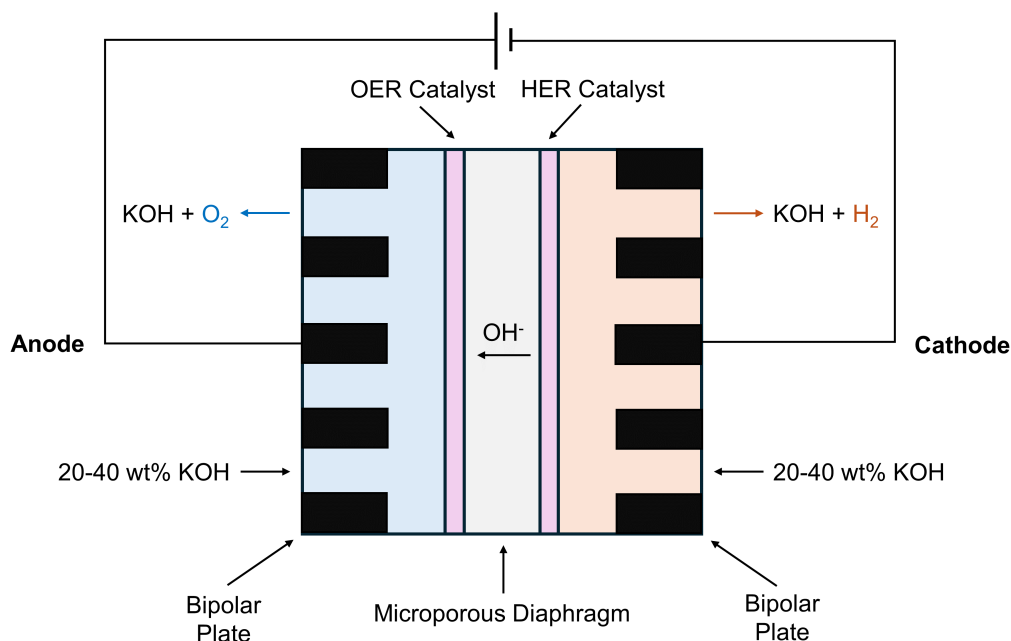


Figure 1.2: Alkaline water electrolyser [12]

The figure shows two electrodes separated by a microporous diaphragm and electrolyte. The alkaline electrolyte, commonly 20-40 wt% potassium hydroxide (KOH), is flown to both cathode and anode, where HER and OER are taking place as governed by reactions 3 and 4, respectively. Typically, abundant materials such as nickel-coated perforated stainless steel are used as a catalyst for either reaction [7]. Furthermore, the electrolyser is operated in a window between 70-90°C depending on the electrolyte concentration, to take advantage of the optimal electrolyte conductivity.

Most of the advantages of AWE are coupled to its use of potassium hydroxide aqueous electrolyte, which enables the use of relatively cheap and abundant catalysts and cell materials without compromising efficiency and durability of the electrolyser [7]. Moreover, alkaline water electrolyzers exhibit a very low degradation rate, commonly described by change in applied potential over time, of less than 3 $\mu\text{V/h}$ [13].

Nevertheless, the use of AWE also presents a number of significant drawbacks. First, due to its electrolyte gap, alkaline water electrolysis suffers from decreased conductivity and consequently increased cell overpotential caused by bubble generation at either electrode [7]. The electrolyte gap also prevents AWE from reaching comparably high current densities due to ohmic losses caused by the liquid electrolyte [13]. Second, the microporous diaphragm poses a risk in terms of product crossover between the compartments. This impacts both operational safety, as the crossover can lead to the formation of an explosive oxygen-hydrogen gas mixture, as well as cell performance due to potential oxygen reduction at the cathode and lowered gas product purity [13]. Lastly, AWEs require several hours to reach steady-state operation in terms of electrolyte flow, temperature and current density, rendering them unsuitable for the coupled use with intermittent renewable energy sources [7].

1.1.3. Proton-Exchange Membrane Electrolysis

While most water electrolyzers are still based on alkaline electrolysis, recent years have seen a strong increase in the use of proton-exchange membrane (PEM) electrolyzers [14]. The PEM is commonly made out of a perfluorosulfonic acid polymer, also known as Nafion. Figure 1.3 shows the design of a typical PEM electrolyser.

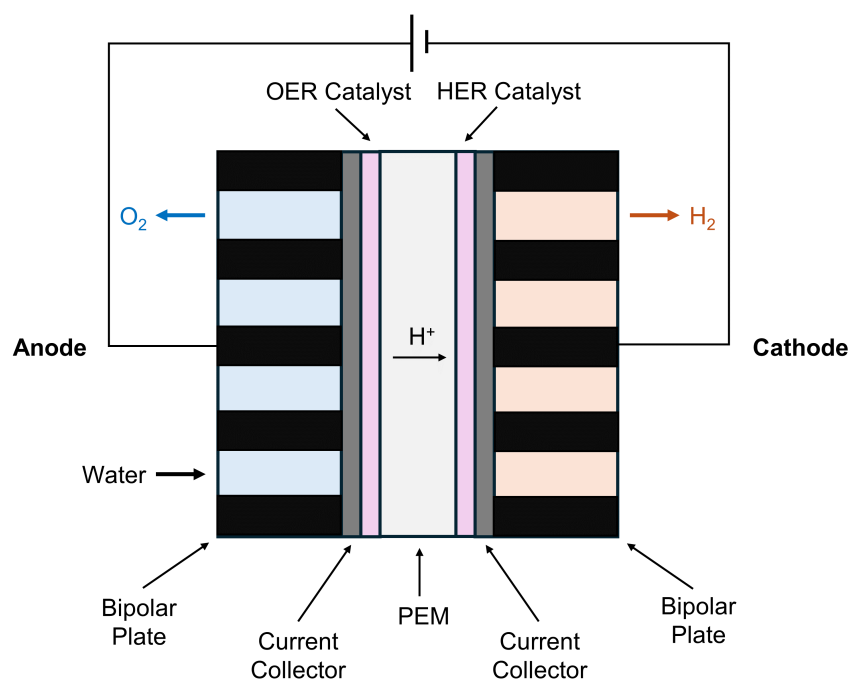


Figure 1.3: Proton-exchange membrane electrolyser [12]

A PEM electrolyser follows the mechanisms described in reactions 1 and 2. Purified water is fed to the cell anode and split to oxygen and protons (see 2). The water splitting is commonly facilitated by the use of iridium as an OER-catalyst. While the gaseous oxygen leaves the cell, the protons travel through the proton-exchange membrane to the cathode. There they are reduced to hydrogen, typically using platinum as a HER-catalyst (see 1). This movement of protons through the PEM is accompanied by water transport due to electroosmosis [15].

PEM electrolyzers offer a variety of advantages compared to alkaline water electrolyzers. First, PEMWE can operate at very high current densities of more than 2 A/cm^2 , which lowers their operational cost [13]. Second, PEM electrolyzers exhibit very low gas crossover rates at a variety of current densities. This allows for safe operation under changing power input, as is required for electrolyzers that are coupled to intermittent renewable energy sources [13]. Finally, the use of a PEM enables the electrolyser to be built in a compact and structurally strong shape, which facilitates the operation under high pressures. As such, PEM electrolyzers have been tested successfully at more than 170 bar of differential pressure for thousands of hours [16]. Operating under such high pressures allows for the electrochemical compression of hydrogen, reducing the required energy input for mechanical hydrogen compression later on.

Nonetheless, the use of PEM electrolyzers also entails a distinct disadvantage. The highly corrosive acidic environment necessitates the use of corrosion-resistant materials for cell parts such as the catalyst layers, current collectors and bipolar plates [13]. Furthermore, for the targeted current densities of more than 2 A/cm^2 to come into effect, these materials must simultaneously resist corrosion under high applied voltages. Only few materials are eligible for use under these conditions. Current collectors and bipolar plates, for example, have to be made of expensive titanium, while only noble catalysts such as platinum and iridium exhibit the required combination of efficiency and stability [7]. Among these, the use of iridium is particularly problematic, as the element is one of the rarest on Earth. Lastly, even when using such corrosion-resistant metals and catalysts, PEMWE still exhibits a significantly higher degradation rate than AWE of roughly $14 \mu\text{V/h}$ [13].

1.2. Direct Seawater Electrolysis

This chapter aims to give an overview of common challenges in direct seawater electrolysis (DSE) and to provide an introduction to some of the previously investigated mechanisms for DSE. As such, sub-

chapter 1.2.1 starts by listing fundamental anode and cathode challenges in DSE. Next, chapters 1.2.2 to 1.2.4 present an overview of three proposed mechanisms for direct seawater electrolysis: the use of PTFE membranes, seawater vapour electrolysis, and the use of bipolar membranes. All mechanisms are introduced by showing their basic design, followed by an explanation of the underlying mechanism, and finally a characterisation of the process with regard to performance and degradation.

1.2.1. Fundamental Challenges

Compared to conventional water electrolysis using purified water, seawater electrolysis faces a variety of challenges that severely limit its practicability. These challenges can be separated into two categories: those affecting the anode and those affecting the cathode.

At the cathode, the main challenge revolves around the precipitation of carbonaceous and hydroxylated species based on the dissolved calcium and magnesium cations in seawater. This is especially true for alkaline water electrolysis, where the generation of hydroxide ions leads to an alkali-shift close to the cathode (see reaction 3). A similar alkali-shift, though to a lower extent, can also be observed in acidic water electrolysis, caused by the consumption of protons at the cathode (see reaction 1) [17]. Under sufficiently high current densities, this alkali-shift will then lead to the precipitation of $\text{Ca}(\text{OH})_2$ and $\text{Mg}(\text{OH})_2$ [18]. Likewise, considering the existence of dissolved carbon dioxide in seawater, carbonates of these cations such as CaCO_3 and MgCO_3 can form. Crucially, all four of these compounds are only sparingly soluble in water, leading to irreversible degradation of the electrode surface and increasing cathode overpotential [5].

At the anode, the presence of chloride and its potential oxidation reactions constitute the biggest problems. The latter problem is aggravated by the fact that the thermodynamic standard potentials for some of these oxidation reactions are close to the standard potential of the OER [19]. While other halide ions, such as bromide, can also be found in seawater, the oxidation of chloride is of paramount concern, as it is present in a comparably large concentration (around 0.5 M) [20]. Figure 1.4 depicts the chloride chemistry in artificial seawater in a Pourbaix diagram.

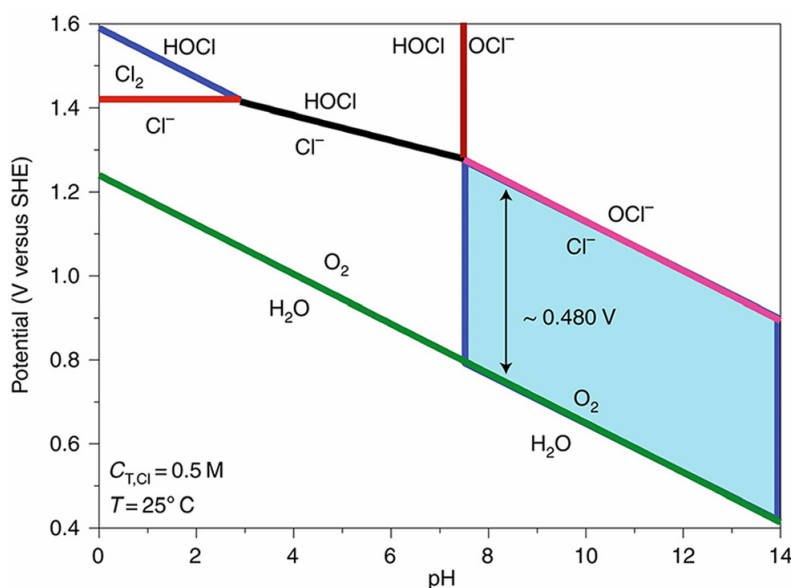


Figure 1.4: Chloride chemistry pourbaix diagram in artificial seawater [21]

The Pourbaix diagram shows that there are three main reaction products from chloride ions based on the solution pH. Up to a pH of approximately 3, the chlorine evolution reaction (CER), i.e., the oxidation of chloride to chlorine gas, is the dominant reaction. Between a pH of 3 and roughly 7.5, the reaction mechanism switches to the formation of hypochlorous acid. Lastly, starting from a pH of 7.5 up to highly alkaline conditions, chloride anions are oxidated to hypochlorite. Of these three regions, both the CER

and the formation of hypochlorite constitute oxidation reactions [18]. Finally, while the Pourbaix diagram shows either oxidation reaction to be thermodynamically less favourable compared to the OER, both OER reactions are four-electron reactions that require a high overpotential (see reactions 2 and 4). In contrast, the CER and the formation of hypochlorite are two-electron reactions and thus exhibit a kinetic advantage [22].

The potential oxidation reactions of chloride are problematic as they compete with the OER, thus lowering Faradaic efficiency of the anodic reaction. This effect, however, is often of lesser concern, as water electrolysis is performed primarily for the production of hydrogen, whereas oxygen is merely considered a byproduct. Nonetheless, there are some cases in which the generation of pure oxygen from water electrolysis might be desirable [19]. Furthermore, the hypothetical production of chlorine gas poses a safety problem, as chlorine gas is very poisonous [23]. Of similar concern is the general presence of chloride ions, as chloride is known to lead to severe corrosion of various metals. Crucially, this also includes corrosion of otherwise corrosion-resistant alloys, as chloride is capable of breaking down the passive film that forms on these metal alloys, triggering corrosion processes of the underlying metals [24].

1.2.2. PTFE Membranes

A recently proposed mechanism for in-situ seawater purification uses the water vapour pressure difference across a polytetrafluoroethylene (PTFE) membrane to draw out water from seawater while blocking the passage of dissolved ions [25]. The basic structure of the system that was used to evaluate this mechanism is shown in figure 1.5.

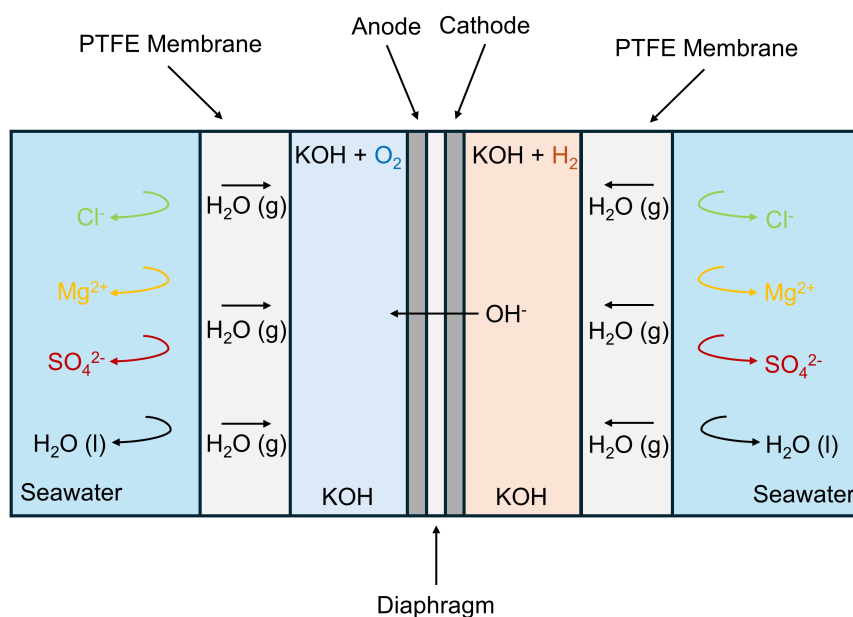


Figure 1.5: Electrolysis cell using in-situ PTFE-based water purification [25]

At the outermost part of the cell, liquid seawater is flowed along a PTFE membrane. Due to the hydrophobicity of the membrane, liquid water, as well as its dissolved ions, are unable to cross the membrane barrier. In contrast, water vapour is able to pass the membrane through the small pores in its structure that serve as gas channels. By using a suitable electrolyte with a comparatively lower water vapour pressure, such as highly concentrated potassium hydroxide (KOH), a water vapour pressure difference is created across the membrane that transports purified water from the seawater to the electrolyte. After passing the membrane, the water vapour condenses and is absorbed by the potassium hydroxide electrolyte via hydration. This mechanism allows for an in-situ purification of seawater and, as long as the absorbed water vapour is consumed during electrolysis, a stable water flux due to the consistent water vapour pressure difference across the membrane. Inside the cell, water is split under highly alkaline conditions following the reactions shown in 3 and 4. To facilitate the reactions, catalysts

are used for both electrodes - a mixture of nickel and molybdenum on nickel foam at the anode, and platinum on a nickel mesh at the cathode. Finally, a diaphragm separates the two cell compartments to prevent the mixture of oxygen and hydrogen, while simultaneously allowing for the movement of hydroxide ions from cathode to anode.

Using the setup shown in figure 1.5, researchers were able to perform seawater electrolysis for 72 hours at 250 mA/cm^2 and 400 mA/cm^2 on a lab-scale cell, observing cell voltages of 1.95 V and 2.3 V, respectively. During these tests, real seawater was used. With regard to performance degradation, the cell voltages remained approximately constant throughout the entire testing period at both current densities. Lastly, only trace amounts of seawater impurity ions, such as hypochlorite, sulfate, and magnesium ions, were found in the KOH solution after 72 hours of continuous operation. The concentration of all of these impurity ions stayed below 0.1% of the corresponding ion concentration in seawater, showcasing the efficacy of the PTFE membrane as an ion barrier. To demonstrate their stability improvement, the researchers also ran the same cell design on liquid seawater without in-situ purification. In that case, the cell failed within 1 h of operation.

1.2.3. Seawater Vapour

As an alternative, the use of seawater vapour for water electrolysis has been suggested [26]. Seawater vapor excludes a range of contaminants, such as various ions and microorganisms, that are commonly found in liquid seawater. Furthermore, the relative humidity of air directly above seawater is commonly in the range of 75-85%, thus making it a potentially useful feed for water electrolysis, without any additional energy input for purification.

Previous research has shown the general practicability of using water vapour as feedstock in PEM electrolyzers [27]. Figure 1.6 shows the basic setup of a cell used to investigate the proposed mechanism by Kumari et al. [26].

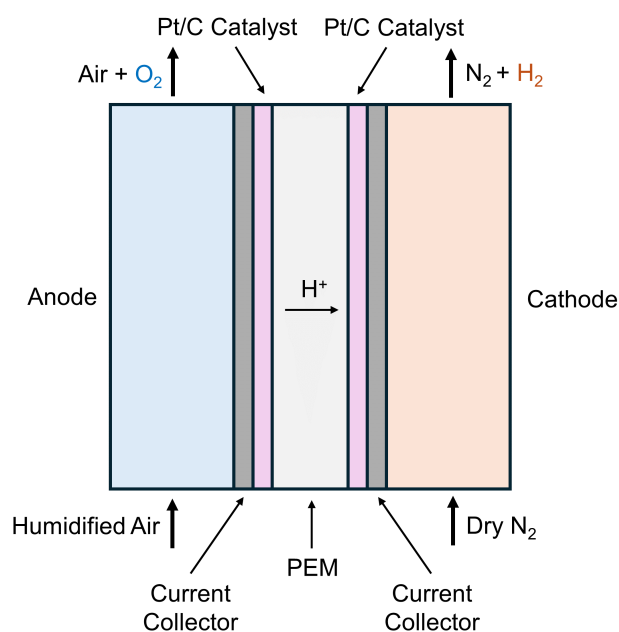


Figure 1.6: PEM electrolyser using seawater vapour [26]

At the anode, seawater vapour is fed to the electrolysis cell. The seawater vapour is previously obtained by bubbling air in real seawater. The water molecules of the vapour are then split at the platinum on carbon (PtC) anode catalyst layer according to reaction 2, and the produced oxygen gas swept out with the air feed. Simultaneously, dry nitrogen gas is fed to the cathode side of the cell, where the protons that originate at the anode and travel through the Nafion membrane recombine to form hydrogen gas as governed by reaction 1. Again, PtC is used as a catalyst to accelerate this recombination reaction. Likewise, the hydrogen gas is swept out by the cathode feed. By feeding the humidified air only to

the anode, efficiency losses stemming from the thermodynamically favored reduction of oxygen at the cathode are avoided [26].

Using such an integrated seawater vapour electrolysis cell, electrolysis at a stable current density of 6-7 mA/cm² under an applied voltage of 1.6 V has been reported [26]. With regard to degradation, the same tests showed an unchanged current density before and after 50 hours of continuous operation when using seawater vapour. In comparison, the current density dropped by 99.6% over the same testing duration when using liquid seawater in the same cell and under identical testing parameters instead. However, some performance degradation is still observed when using seawater vapour, with the maximum attainable current density dropping by approximately 27%. No detailed analysis was done as to the causes of this performance degradation or the exact composition of the seawater vapour feed. Lastly, it was found that changing the relative humidity or the mass flow rate of the water vapour significantly influences the attainable current density, suggesting a quick onset water transport limitations when using water vapour.

1.2.4. Bipolar Membranes

Another technology that has been tested for the use in direct seawater electrolysis are bipolar membranes (BPM). Bipolar membranes are membranes consisting of a cation-exchange layer (CEL) and an anion-exchange layer (AEL), separated by a catalyst that allows for the dissociation of water into protons and hydroxide ions [28]. BPMs are a promising technology for direct seawater electrolysis because they offer the chance to simultaneously limit ionic diffusion and migration within the cell via the CEL and AEL, as well as micro-managing local pH environments at both electrodes to, for example, favour the OER over chloride oxidation at the anode. Figure 1.7 shows the BPM direct seawater electrolysis cell design tested by Marin et. al [29]:

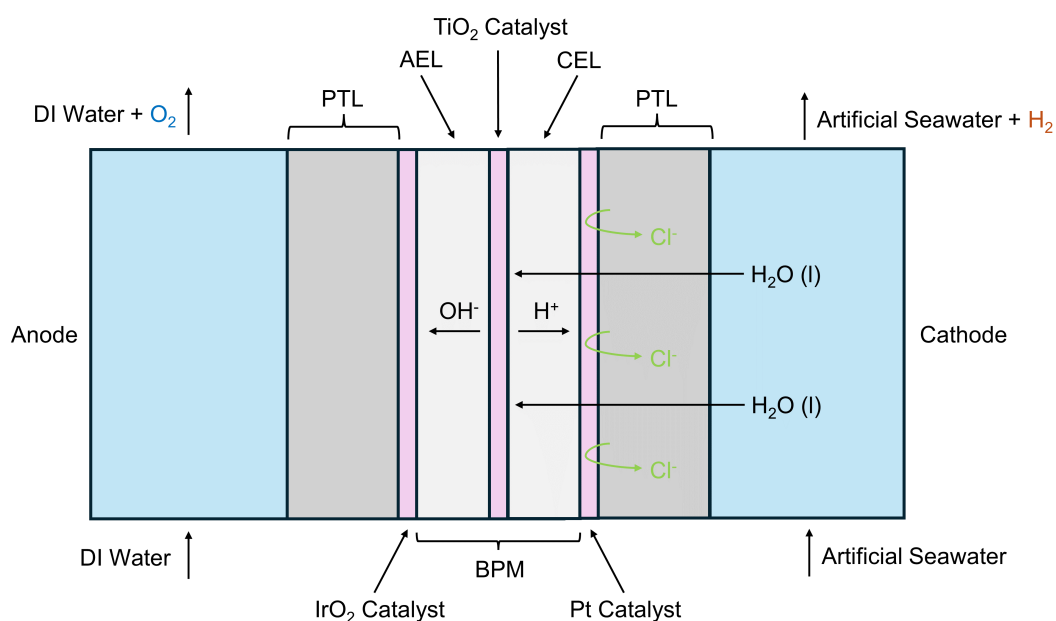


Figure 1.7: BPM-based seawater electrolysis cell [29]

In their design, seawater is fed to the cathode. There, it passes a porous transport layer (PTL) and enters the BPM via its cation-exchange layer to reach the water dissociation (WD) catalyst layer. At the WD layer, the water is split into protons and hydroxide ions facilitated by a titanium oxide catalyst. Then, the protons and hydroxide ions migrate through the ion-exchange layers toward the cathode and anode, respectively. These migration processes cause a local pH shift at anode and cathode, alkalinising the anolyte and acidifying the catholyte - thus decreasing the overpotentials required for the OER and HER to take place. At the anode, the hydroxide ions are oxidised to create gaseous oxygen and water, as governed by reaction 4, and facilitated by an iridium oxide catalyst. Conversely, the protons are reduced to hydrogen at the cathode (see reaction 1) via a platinum catalyst. By feeding

the seawater only to the cathode, diffusion and migration of chloride to the anode is prevented by the cation-exchange layer of the BPM.

The researchers tested their cell design both by using artificial seawater (0.5 M NaCl) as the cathode feed, as well as using real seawater. All tests were performed on the BPM cell shown in figure 1.7, followed by a regular PEM electrolyser for comparison. Using artificial seawater, the cell voltage degradation rates of the BPM cell was found to be 28 mV/h over 6 hours of continuous testing at 250 mA/cm², starting at an initial cell voltage of 2.75 V. In comparison, the PEM cell showed a lower initial overpotential of 2.12 V, but also a higher degradation rate of roughly 35 mV/h. However, the standard deviation of the degradation measurements was found to be so large that no clear determination could be made as to which cell degrades faster. When using real seawater, electrolysis tests were performed at a current density of 250 mA/cm² for the duration of 100 hours. Over this period, the BPM cell voltage increased from an initial 2.75 V to approximately 3.8 V, equalling a degradation rate of 10.5 mV/h. In comparison, the PEM cell started at a significantly lower cell voltage of roughly 1.65 V, but failed within the first 50 hours of operation. With regard to degradation causes, the researchers assume that the accelerated cell voltage degradation of the PEM cell is caused by the formation of corrosive free chlorine species at the anode. In comparison, most of the BPM cell degradation contribution is assumed to be caused by degradation of the AEL [29].

1.3. Forward Osmosis

This chapter begins by introducing the concept of forward osmosis. Afterwards, two of the main challenges occurring in forward osmosis processes are explained: external concentration polarisation (ECP) and internal concentration polarisation (ICP). Finally, previous research on the use of forward osmosis membranes in direct seawater electrolysis is presented and the current state-of-the-art forward osmosis electrolysis cell design and performance analysed.

Forward osmosis describes the process of water movement from a solution of low solute concentration, or low osmotic pressure, to a solution of high solute concentration, or high osmotic pressure, through a semipermeable membrane that connects the two [30]. The semipermeable membrane allows only solvent molecules to pass, whereas, ideally, all solute molecules are rejected. The process is illustrated in figure 1.8.

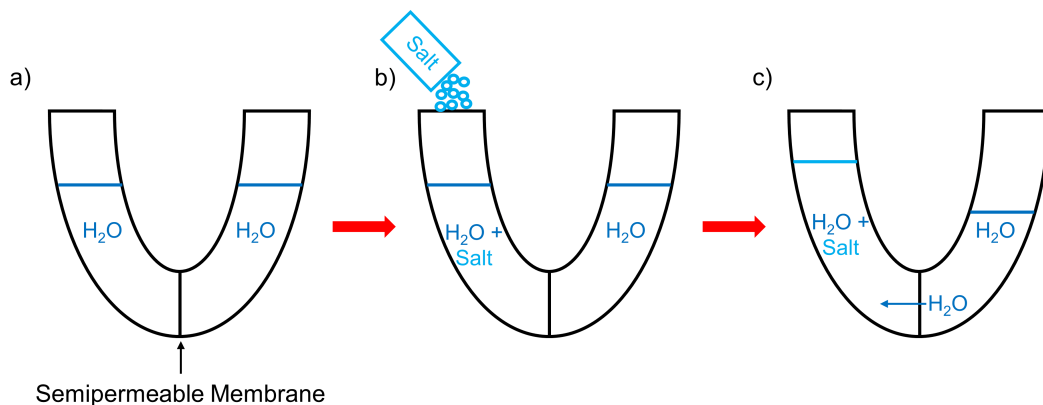


Figure 1.8: The forward osmosis process [30]

Under a) two water volumes are shown that are separated by some type of semipermeable membrane. Next, in b), a salt is added to one of the two solutions, increasing its osmotic pressure relative to the pure water volume (see 1.1). This solution of higher osmotic pressure is commonly called the draw solution, whereas the solution or liquid of lower osmotic pressure is called the feed solution. Then, as a consequence of the difference in osmotic pressure, water molecules are drawn out of the water volume and pass through the membrane into the water-salt solution, as is shown in c). This process continues

until the hydrostatic pressure exerted on the membrane by the rising water column of the feed solution equals the osmotic pressure between the two solutions.

The osmotic pressure of a dilute solution can be calculated via the van't Hoff equation [31]:

$$\Pi = I \cdot M \cdot R \cdot T \quad (1.1)$$

where:

- Π = Osmotic pressure in Pa
- I = Van't Hoff factor
- M = Molarity in mol/L
- R = Gas constant in J/(mol*K)
- T = Temperature in K

Where R denotes the universal gas constant, T the temperature of the solution, M the number of solute moles divided by the total solution volume, also called the solution molarity, and i the so-called van't Hoff factor, which describes into how many dissolved particles a solute molecule dissociates. As is evident from the formula, osmotic pressure is a colligative property. As such, it does not depend on the chemical nature of the solute, but only on the number of dissolved molecules.

1.3.1. Concentration Polarisation

Commonly, forward osmosis membranes are made out of two layers: a dense active layer, and a porous support layer. The former is the layer responsible for water movement and salt rejection, whereas the latter provides mechanical support for the membrane structure [30]. However, this asymmetric structure entails a considerable disadvantage, as it leads to a phenomenon known as concentration polarisation. There are two kinds of concentration polarisation effects that negatively impact the water movement across the membrane: external concentration polarisation (ECP) and internal concentration polarisation (ICP). Figure 1.9 shows an overview of these two different processes.

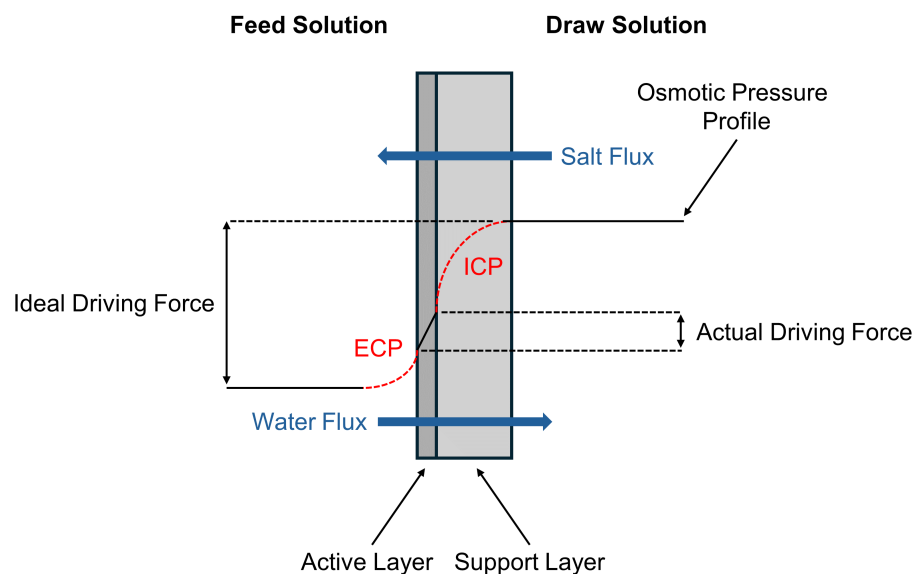


Figure 1.9: Internal and external concentration polarisation in an asymmetric forward osmosis membrane [30]

When the active layer of an asymmetric FO membrane faces the feed solution, there is an increase in solute molecule concentration at the interface between solution and active layer due to the water flux from the feed to the draw solution. This localised concentrative effect is referred to as concentrative

external concentration polarisation. As it leads to a localised increase in osmotic pressure at the active layer, it decreases the driving force for the water movement and has a negative effect on the observed water flux. On the other side of the membrane, the water movement from the feed to the draw solution leads to a dilution of the draw solution inside the porous support layer. This dilutive effect is called dilutive internal concentration polarisation. Same as for concentrative ECP, dilutive ICP causes a decrease in the driving force behind the forward osmosis process and thus negatively impacts observed water flux.

While both external and internal concentration polarisation impact water flux, dilutive ICP is by far the more detrimental process. As such, it can decrease the observed water flux by up to 80% [32]. The relative dominance of ICP over ECP is due to two factors decreasing the importance of ECP in forward osmosis. First, the external concentration polarisation can be managed effectively by optimising flow velocity and turbulence at the feed-active layer interface [33]. Second, as forward osmosis processes do not typically operate under any hydraulic pressure, there is a natural limit to the solute build-up at the active layer [30].

As shown in the figure, asymmetric forward osmosis membranes are typically oriented such that the active layer faces the feed solution, whereas the support layer faces the draw solution. This orientation is due to the main application of forward osmosis membranes in seawater purification. If the porous support layer was facing the seawater feed solution during purification, the microorganisms and bacteria this seawater typically contains would lead to swift fouling of the support layer. If the porous support layer is facing the draw solution, however, special care can be taken to assure that this draw solution poses a low biofouling threat to the layer.

1.3.2. Forward Osmosis-Based Direct Seawater Electrolysis

Due to its use in water filtration, the application of forward osmosis membranes in direct seawater electrolysis has been proposed and tested by researchers [5]. The general idea behind the use of forward osmosis is that it enables in-situ water purification by using an electrolyte with a sufficiently high osmotic pressure compared to seawater. The structure of one such system is shown in the figure below:

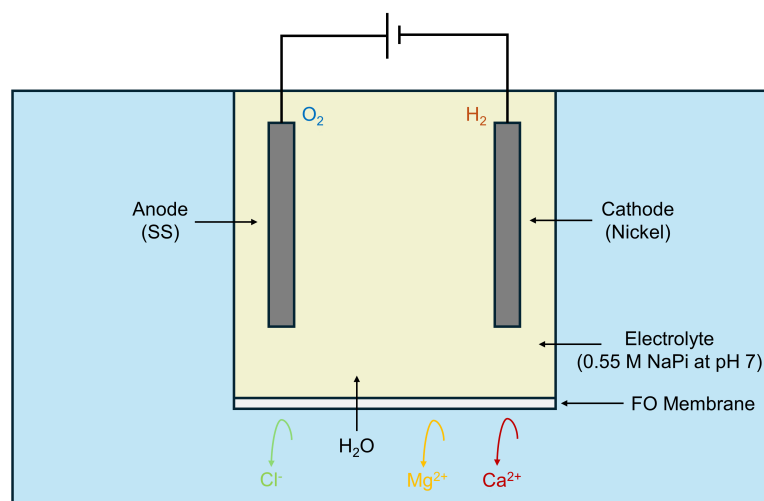


Figure 1.10: Forward Osmosis-Based Direct Seawater Electrolysis Cell [5]

An electrolysis cell consisting of a stainless steel mesh (SS) anode and nickel mesh cathode is placed in a container filled with seawater. The two electrodes are separated by a pH 7 sodium phosphate buffer. In between the cell and the seawater container, a forward osmosis membrane is placed that separates the cell electrolyte from the surrounding seawater. Due to the osmotic pressure difference between the draw solution (the cell electrolyte) and the feed solution (seawater), water moves into the cell. This process allows for the replenishment of water consumed during electrolysis. Simultaneously,

the forward osmosis membrane purifies the seawater by blocking unwanted ionic species, such as chloride, as well as magnesium and calcium ions, from passing into the cell.

Operating such a direct seawater electrolysis cell, Veroneau et al. were able to perform water electrolysis at a current density of 25 mA/cm^2 over a period of five days using real seawater. During this period, the observed overpotentials were 0.63 V and 0.83 V for the cathode and anode, respectively. Furthermore, despite the consumption of roughly 1 ml of water per day via electrolysis, the total cell volume increased over the five days of testing. Based on this observation, the researchers assume that the water influx via the FO process exceeded the water outflux during electrolysis, demonstrating the general feasibility of the proposed replenishment process. However, no measurements were performed to quantify the water influx into the cell via the forward osmosis process.

The tests also showed the FO membrane to be an imperfect ion barrier. As such, phosphate leached out of the cell and into the seawater at a pace of roughly $0.11 \text{ mmol per day}$, compared to a considerably faster influx of chloride from the seawater at $0.92 \text{ mmol per day}$. Furthermore, hypochlorite ions, the chlorine oxidation product predicted by the corresponding Pourbaix diagram at neutral pH (see Figure 1.4), slowly accumulated in the cell at a rate of $1 \text{ } \mu\text{mol per day}$. Despite of the loss of electrolyte and the gradual accumulation of chloride, the electrolysis cell showed no loss in Faradaic efficiency for either OER or HER and no observable change in overpotential for either electrode over the tested period. The researchers attribute this observation to three factors. First, the relatively high selectivity of the used FO membrane. Second, the use of a sodium phosphate buffer which has been reported to promote the OER over chloride oxidation reactions [19]. And third, the use of a buffer electrolyte which reduces pH gradients at both electrodes.

Finally, a number of potential system improvements is given by the researchers. For example, the inclusion of an anion or cation exchange membrane to prevent mixing of the gaseous hydrogen and oxygen products. Furthermore, they mention potential improvements on the cell compartment design, including a separation of the hydrogen and oxygen product streams, as well as controlling the electrolyte flow along each electrode. Also, the researchers did not attempt to quantify the water flux occurring across the forward osmosis and into their cell. By observing a slightly increased cell volume after testing, they merely assume that water influx exceeded water consumption during operation at the chosen current density. However, by not measuring the water flux, no general conclusion is made as to the maximum current density that the cell could sustain before the water consumption exceeds the water influx and the electrolyte composition starts changing. Thus, the observed water mass flux across a FO membrane within the chosen system is a crucial piece of information that is missing to assess the FO-based water electrolysis potential.

1.4. Research Questions

As introduced in the previous subsection, the general viability of the use of forward osmosis membranes in water electrolysis cells for in-situ water purification has already been demonstrated. However, in previous research these electrolysis cells were only tested up to a very low current density of 25 mA/cm^2 . Furthermore, no attempt was made to quantify the water influx into the cell with the chosen feed and draw solutions. Thus, a knowledge gap exists with regard to the maximum sustainable current density attainable during operation within the chosen system. Lastly, the current state-of-the-art forward osmosis cell exhibits high anode and cathode overpotentials, despite only having been tested at low current density. Thus, this thesis aims to optimise the existing forward-osmosis cell design by Veroneau et al. by designing and testing a zero-gap electrolysis cell with FO-based water purification. A central goal of this optimisation procedure is to quantify the maximum current density enabled by the purification process. Another research objective is to analyse the cell design for performance and material degradation during testing. Based on these research goals, the following research questions are formulated:

1. What is the maximum current density at which a FO seawater electrolysis cell can be operated sustainably?
2. Does a zero-gap forward-osmosis cell design pose an improvement on the current state-of-the-art FO electrolysis cell with regards to observed overpotentials and cell performance?
3. Does the zero-gap forward-osmosis cell degrade during operation at this maximum current density and, if so, what causes the degradation processes?

To answer these research questions, chapter 2 first introduces the methods and methodology used throughout the research project, including cell designs, testing setups and protocols, and degradation investigation methods. Next, chapter 3 presents all electrochemical and degradation testing results and discusses their significance. Afterwards, chapter 4 summarises the key findings and provides answers to the research questions stated above. Finally, chapter 5 provides recommendations for future research on the topic based on the findings of the research project.

2

Methods and Methodology

In this chapter, the methods and methodology used to answer the research questions are presented in detail. In general, the approach to answer the research questions followed the logic shown in figure 2.1.

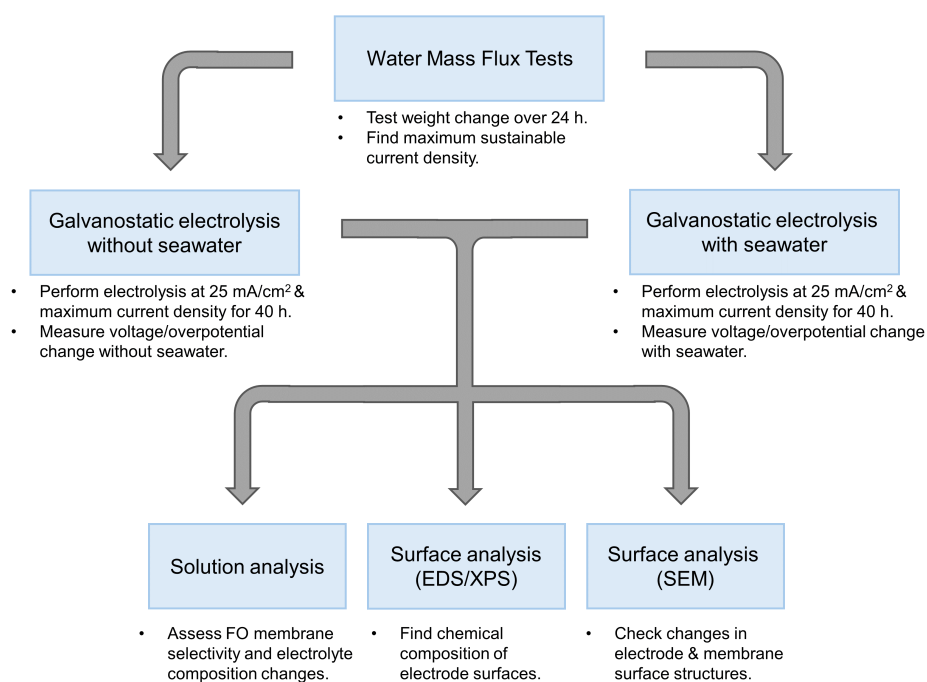


Figure 2.1: Testing overview

First, water mass flux measurements were conducted to quantify the rate at which water moves through the FO membrane with the given draw and feed solutions. From this measurement, the maximum sustainable current density was calculated. Naturally, this test and all subsequent tests required some form of electrochemical cell to be performed on. The design of these cells is introduced in section 2.1. Afterwards, the setup of the water mass flux experiment and the method used to calculate the current density are described in section 2.2. Next, long-term galvanostatic electrolysis tests were performed on an electrolysis cell at a current density of 25 mA/cm², which corresponded to the maximum current density at which the current state-of-the-art FO electrolysis cell had been tested, as well as at the previously calculated maximum current density. These galvanostatic tests were both conducted solely with the electrolyte (see subsection 2.3.1) and with seawater (see subsection 2.3.2). In the latter case,

the seawater was filtered in-situ via the FO membrane in an additional cell. Following these tests, the electrodes, membranes, and solutions were analysed individually in a variety of testing methods to analyse the system degradation in depth. The methodologies used in these tests are described in subsections 2.4 and 2.5.

2.1. Test Cell Design

To answer the research questions, a suitable electrochemical test cell was required. In fact, two complementary cell designs were needed: one to test the water mass flux over the forward osmosis membrane, and one to perform water electrolysis. This section introduces both of these cells and describes the reasoning behind their design. Both cells are based on the commercial Micro Flow Cell by ElectroCell A/S [34].

2.1.1. Water Mass Flux Test Cell

Since the forward osmosis process was used to replenish the water consumed during electrolysis, the water transportation across the membrane was quantified in advance. This information was crucial as it later determined the maximum current density at which the electrolysis cell could be run sustainably. To measure the water mass flux, the following cell construction was used:

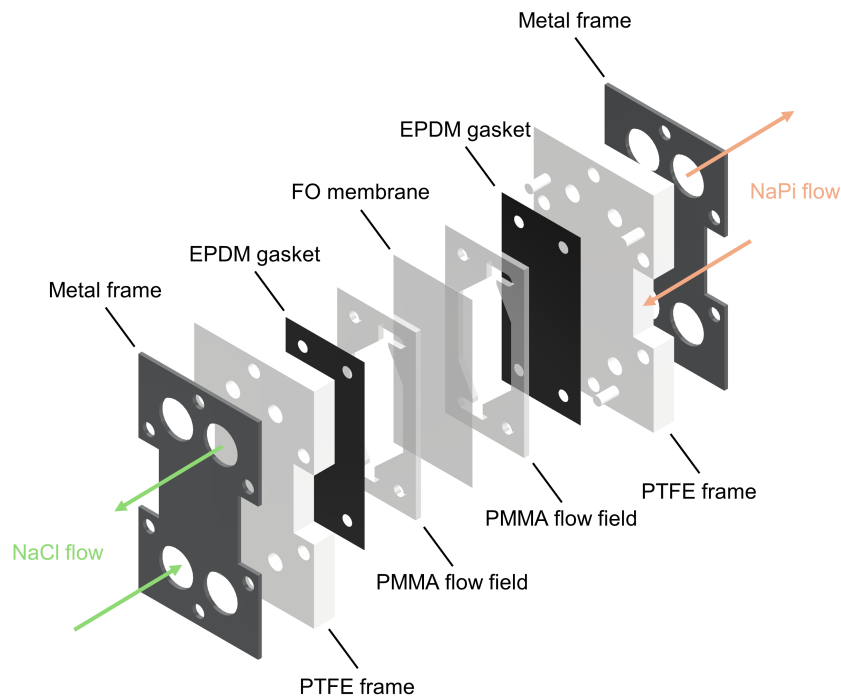


Figure 2.2: The water mass flux test cell

As can be seen in figure 2.2, the water mass flux test cell has a symmetrical design with the forward osmosis membrane as the mirror axis. Each cell half consists of an outer metal frame with openings for six small openings for screws and four large openings for tubing connectors. Directly behind the metal frame follows the PTFE frame, which also contains openings for screws and tubing connectors. One of the outer PTFE frames also contains four guide pins, with corresponding depressions on the second PTFE frame, which ensure alignment of all cell parts during construction. The PTFE frame is followed by a simple EPDM gasket and a flow field made of PMMA. Finally, the two cell halves are separated by the forward osmosis membrane. In order to attain a reproducibly leakage-free test cell, the cell is screwed together using a torque wrench set to 4 Nm.

For all tests, flat-sheet forward osmosis membranes made of cellulose triacetate (CTA) by the manufacturer FTS H2O were used [35]. Thus, the same forward osmosis membranes were used as in

the current state-of-the-art FO electrolysis cell introduced in subsection 1.3.2. In between tests, the membranes were stored in DI water, which was replaced at least once a week to avoid the onset of membrane fouling, as advised by the manufacturer. The membranes are designed for operation at temperatures up to 50 °C and in an pH environment between 3-7.

For all water mass flux tests, as well as all later electrolysis tests, only two types of solutions were used. First, real seawater was approximated by the use of artificial seawater in the form of a 0.5 M NaCl solution. This relatively simple seawater recipe was used for two reasons. First, including chloride ensures that both the problem of chloride oxidation reactions, as well as chloride-induced metal corrosion mentioned in subsection 1.2.1 can be observed in the chosen system. Second, by not using real seawater, the analysis of the degradation results is facilitated. For example, had real seawater been used, additional membrane fouling would likely have occurred. Real seawater contains a multitude of microorganisms and bacteria that can cause biofouling, as is often observed in reverse osmosis desalination systems [36]. However, biofouling of membranes is a complex biological-chemical process that would warrant a separate investigation.

The second used solution was the cell electrolyte. As for the current state-of-the-art FO seawater electrolysis cell, the cell electrolyte consisted of a pH 7, 0.55 M sodium phosphate buffer solution (see figure 1.3.2). This solution was attained by mixing disodium phosphate, which acts as a weak base, and monosodium phosphate, which acts as a weak acid. The buffer was prepared using an open-source pH calculator designed by Robert J. Beynon from the University of Liverpool [37]. Despite the comparably low activity of both OER and HER catalysts at neutral pH [18], there are a variety of reasons why to use neutral sodium phosphate buffer as an electrolyte. First, sodium phosphate buffer is known to favour the OER over the various chloride oxidation reactions shown in figure 1.4 [19]. Second, using a buffer solution helps lowering the local pH shifts that are occurring at both anode and cathode and that, in real seawater, would facilitate the deposition of hydroxylated cation species on the cathode. Next, using a neutral buffer solution also ensures that the limited pH window of 3-7 for the FO membrane is not exceeded drastically. Finally, the 0.55 M sodium phosphate buffer dissociates to a degree that is high enough to ensure a larger osmotic pressure than that of the used artificial seawater. Thus, the buffer solution can act as the draw solution in the targeted forward osmosis process.

2.1.2. Electrolysis Cell

The second cell needed to answer the research questions was the electrolysis cell. Figure 2.3 shows the design that was used for all electrochemical tests.

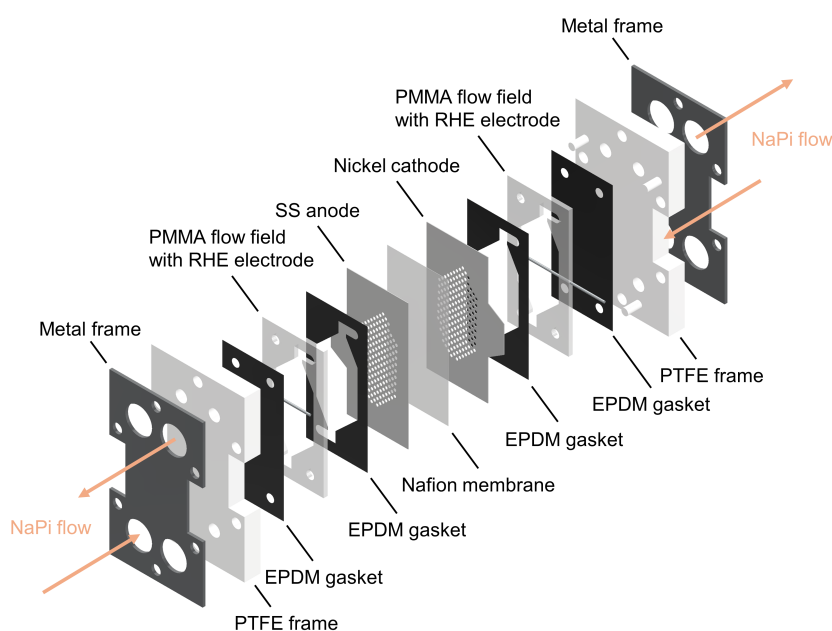


Figure 2.3: The electrolysis cell

Same as for the water mass flux cell, the electrolysis cell consists of two symmetrical cell halves with different electrode materials. However, compared to the cell design shown in 2.2, there are a few fundamental changes.

First, the flow field guiding the electrolyte through the cell has a small opening on one side in which a reversible hydrogen electrode (RHE) is placed. The shaft of the RHE is made of polyether ether ketone (PEEK) and glued into the frame of flow field using an acrylic glue [38]. Furthermore, the reference electrode is placed horizontally to the direction of the flow and approximately two millimeter away from the opposite end of the flow frame. A horizontal position is chosen to minimise the probability of bubble attachment to the porous front part of the electrode. The shaft is not placed even closer to the opposite flow field frame in order to avoid infringing on any sort of boundary wall flow that is not representative of the flow conditions in the rest of the cell. A visualisation of the placement of the reversible hydrogen electrode within the flow field can be seen under (a) in the figure below:

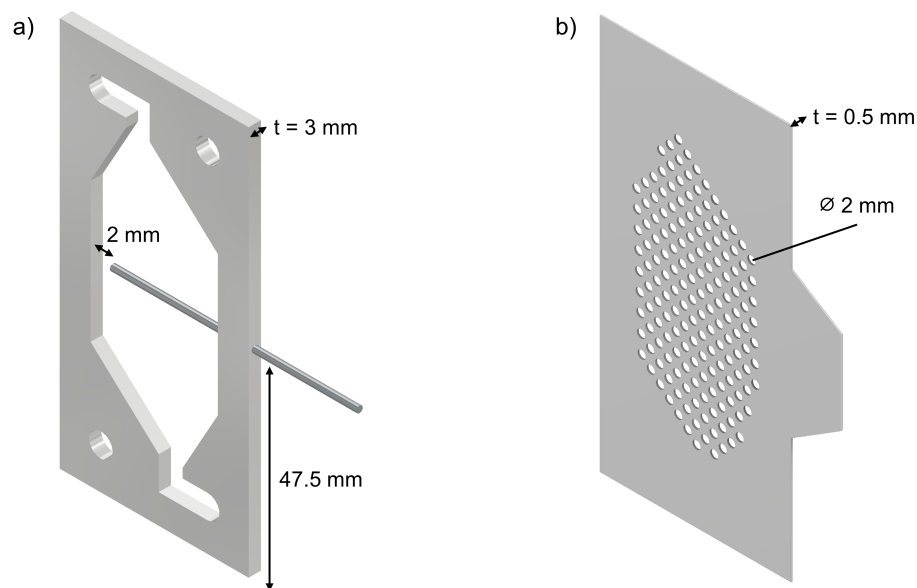


Figure 2.4: Cell part visualisation: (a) Flow Field with RHE; (b) Electrode with outer contact area for electrical connection

Placing the RHE inside the flow field close to anode and cathode allows for separate readouts of anode and cathode overpotential next to the total cell voltage. Furthermore, using reversible hydrogen electrodes, as opposed to any other type of reference electrode, allows for an easy conversion of the measured potential to the observed overpotential for HER and OER. Also, a RHE directly accounts for changes in the pH of the electrolyte, as its potential changes with pH [39]. Thereby, it eliminates the need for pH correction of the measured potentials.

Second, the PMMA flow fields now border on perforated metal plates serving as the electrodes of the electrolysis cell. Since the cell design targets being an improvement on the state-of-the-art forward osmosis seawater electrolysis cell introduced in section 1.3.2, the same electrode materials were used: 316 stainless steel for the anode, and nickel for the cathode. Volcano plots can illuminate why these materials are used despite not being the optimal catalysts for either targeted reaction.

Volcano plots, which are also referred to as Sabatier plots, display the activity of different catalyst materials against their reactivity for a given chemical reaction [40]. Reactivity indicates how strongly the reaction intermediate in the catalytic reaction binds to the surface of the catalyst. Low reactivity values indicate that the intermediate does not bind to the catalyst surface long enough for the reaction to proceed. High reactivity values, on the other hand, signal that the products that are formed on the

catalyst surface are bound too strongly and cannot desorb, thus effectively blocking the catalyst surface. Similarly, the activity describes how effectively the catalysis reaction proceeds, usually by measuring the amount of charge that is consumed by the target reaction per catalyst surface area. Naturally, activity and reactivity are strongly linked. When plotting reactivity and activity of various catalysts in a volcano plot, a typical volcano shape appears, with the optimal catalysts for each reaction being located at the top of the shape.

Figure 2.5 shows the volcano plots for both HER and OER in an acidic environment for a variety of catalysts.

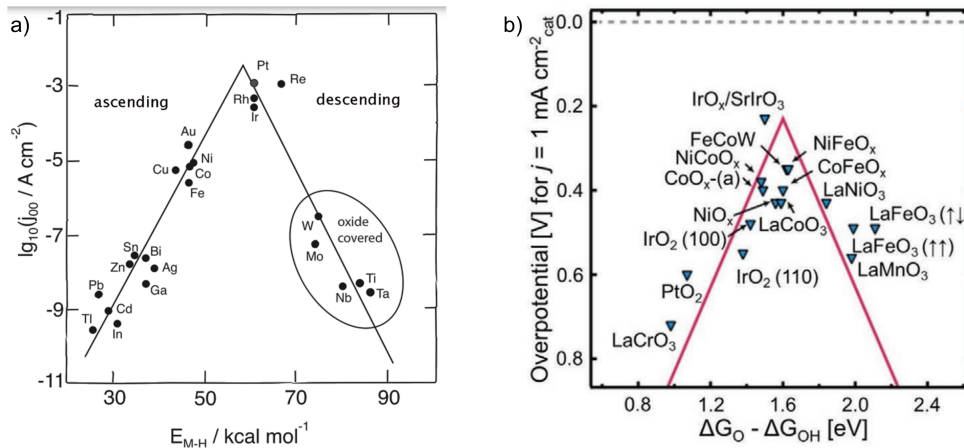


Figure 2.5: Volcano plots: (a) Various catalysts for HER in acidic media [41]; (b) Various catalysts for OER in acidic media [42]

As is evident from figure 2.5, neither SS nor nickel represent the optimal catalysts for their respective reactions. However, as can be seen in part (a) of figure 2.5, nickel actually exhibits comparably good catalytic behaviour, while also being a cheap and abundant metal. To achieve better catalytic performance, rarer and thus considerably more expensive metals such as iridium or platinum would have to be used. Similarly, part (b) of figure 2.5 shows an iridium oxide compound as the optimal catalyst for the OER in acidic media. However, other compounds such as iron-nickel oxide also provide good catalytic performance without the need for rare elements. Coincidentally, these iron-nickel oxide compounds are present on the surface of 316 SS, making it a good HER catalyst choice in acidic environments [43].

While the electrode material choices remain unchanged, there is another crucial difference between the two electrode designs. This change consists of the use of perforated plate electrodes for the new cell design, compared to mesh electrodes for the state-of-the-art cell. The use of perforated plates instead of mesh electrodes stems from the commonly observed problem of bubble entrapment in mesh electrodes at low current densities [44]. While no problem for the previous design, where the electrolyte did not flow and only low current densities were tested, the attempted control of flow in the new cell design combined with testing at higher current densities favoured the use of perforated plate electrodes instead.

A digital model of the used electrodes can be found under (b) in figure 2.4. Each perforation has a diameter of 2 mm. This diameter size was chosen based on two factors. First, a lower diameter size was set to 1.2 mm based on previous research that found that smaller opening diameters lead to the entrapment of oxygen bubbles [45]. While this research was conducted on alkaline water electrolysis, it was nonetheless considered a good starting point for the design process. However, a hole diameter

of 1.2 mm was found to be impractical, as each electrode was water-cut from a metal sheet, and hole diameters below 2 mm did not yield satisfactory manufacturing results. The same consideration also determined the electrode thickness, as any thickness below 0.5 mm was found to lead to excessive bulging of the metal plate during water-cutting. After water-cutting, all electrodes were deburred and cleaned with DI water. The total geometric area of the electrode facing the Nafion membrane (and excluding the manifolds) amounts to 16.21 cm². This value was used for all current density calculations.

Finally, a conductive membrane is used to separate anolyte and catholyte. As the system operates under neutral pH conditions and is supposed to be protected from large pH swings by the buffer, the decision what type of membrane to use was not dictated by the system pH. Instead, Nafion was chosen as the cell membrane based on two other considerations. First, the forward osmosis membrane, which in seawater electrolysis is in contact with the anolyte, has a limited pH range from 3-7. Therefore, the cell could not be operated in an alkaline environment. However, in light of possible optimisation later on, the forward osmosis membrane does theoretically enable operation in a more acidic environment. Thus, the use of a cation-exchange membrane as opposed to an anion-exchange membrane widens the options for potential cell optimisation later on. Second, Nafion is already widely used in electrolysis cells as the most common membrane in PEM electrolyzers, and its behaviour and limitations thus well studied and understood. In addition, Nafion offers a very high proton conductivity of roughly 0.1 S/cm, therefore making it an attractive first choice in order to lower total cell voltage and increase the system efficiency [46]. Lastly, Nafion is known to be highly stable even in very aggressive chemical environments and thus exhibits a comparably low degradation rate, making it a logical choice for the use in potentially highly degradative seawater electrolysis systems [47]. As a pretreatment, all Nafion membranes were soaked in DI water for 24 hours before testing.

2.2. Water Mass Flux Tests

The first step in assessing the performance of a forward-osmosis seawater electrolysis cell consisted of measuring the water mass flux across the forward osmosis membrane. This measurement was crucial as it allowed calculating the maximum current density at which the cell can be operated. In general, it consisted of a simple experiment where the draw and feed solutions are pumped around two compartments separated by a FO membrane, and their weight measured before and after a specified period of time. By comparing the evaporation- and ion diffusion-corrected weights before and after testing, the water mass flux was obtained. Accounting for ion diffusion is of significance, as previous research has reported cellulose triacetate forward osmosis membranes to be imperfect ion barriers [48]. In this section, the chosen setup and tests protocols used for measuring all quantities are shown and described in depth.

When measuring any type of solution weight change, the cell shown in figure 2.2 was used. This cell's inlets and outlets were always connected to the feed and draw solutions as shown in figure 2.6.

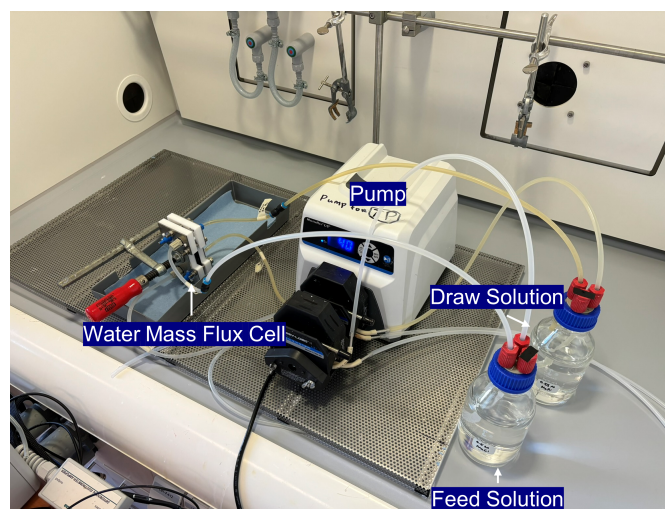


Figure 2.6: The setup used for all evaporation and water mass flux tests

For all water mass flux tests, a testing protocol was followed that can be found in the appendix under list B.1). As mentioned in the protocol, the volume for both draw and feed solution was set to 250 ml. This value was chosen based on a trade-off between minimising changes in the osmotic driving force and ensuring testing practicability. Generally, the draw solution is gradually diluted during testing, whereas the feed solution is gradually concentrated. These processes lead to a decrease in the osmotic driving force, thus making it difficult to measure a constant water mass flux (compare to ECP and ICP in figure 1.9). In contrast, during electrolysis a steady-state operation should be obtained, where all the water that enters the cell through the FO membrane is consumed during water oxidation. Therefore, a minimisation of the decrease in driving force needed to be ensured in order to attain transferable testing results. As is evident from the van't Hoff equation shown in 1.1, the driving force is directly dependent on the solution molarity. Thus, making the draw and feed solution volumes as large as possible should have minimised the change in driving force by minimising the observed changes in solution molarity. By choosing solution volumes of 250 ml for both draw and feed solution, the molarity change of either solution stayed below 5%. This observed change was considered marginal enough to allow for the observation of a near-constant water mass flux over the FO membrane during testing. To quantify the setup evaporation, water mass flux tests were performed while replacing the FO membrane shown in figure 2.2 by an EPDM gasket and following the protocol shown under figure B.1.

Finally, the anion concentrations in the feed and draw solutions were measured before and after testing. Considering the used solutions, the two anions of interest were chloride, which was expected to diffuse from the seawater to the buffer solution, and phosphate, which was expected to diffuse in the opposite direction. The change in sodium concentration, the sole cation in the system, was not measured as the sodium concentration difference between the two testing solutions was comparably small. Furthermore, the accuracy of the chosen concentration measurement method decreases with increasing ion concentration. This complicated getting accurate data on the sodium concentration change, as it was present in high concentration in either solution. For the same reason, the concentration change of either anion was always measured using the solution that contained it in a lower concentration. Thus, the anion concentration of chloride was measured using the sodium phosphate buffer, whereas the seawater was used to quantify the phosphate diffusion. A description of the device used for these tests, as well as of the sample preparation and testing approach is provided in subsection 2.4.2.

2.3. Galvanostatic Electrolysis Tests

As previously shown in the testing logic of figure 2.1, once the water mass flux had been determined and the corresponding maximum current density calculated, galvanostatic water electrolysis tests were performed next. These tests were done to attain used cell parts that could subsequently be analysed further, and to gauge cell voltage, anode overpotential, and cathode overpotential changes under continuous operation.

In total, four different galvanostatic electrolysis tests were performed. An overview of these tests and their testing parameters are given in table 2.1.

Table 2.1: Galvanostatic testing overview

Test ID	Current Density [mA/cm ²]	Seawater Contact
CwoS LC	25	No
CwS LC	25	Yes
CwoS HC	62.39	No
CwS HC	62.39	Yes

To be able to discern whether any of the observed changes in performance parameters and cell part structures were due to the use of seawater for electrolysis, galvanostatic measurements were first performed on a blank cell, i.e., an electrolysis cell that did not come into contact with seawater. Thus, the baseline degradation occurring in the system without the use of seawater was identified. Two tests

at different current densities were performed on this blank cell. The first current density of 25 mA/cm^2 was chosen with regard to research question 2, as the current state-of-the-art forward osmosis seawater electrolysis cell had been tested up to this current density. The second current density of 62.39 mA/cm^2 marked the maximum current density attained by the water mass flux results. Afterwards, a combined cell setup with in-situ water purification was tested under the same conditions to measure additional degradation caused by the use of seawater. Again, galvanostatic measurements at two different current densities were performed on this combined cell.

The tests including seawater and those without differed in their setup, so that their experimental approaches are shown and explained separately. First, subsection 2.3.1 displays the chosen setup for tests with the blank electrolysis cell. Afterwards, subsection 2.3.2 explains the experimental configuration for the electrolysis tests with in-situ seawater purification. After assembly of the testing setups, both experiments followed the same testing protocol shown in figure 2.7. Another, more detailed version of the testing protocol can be found in the appendix under figure B.2.

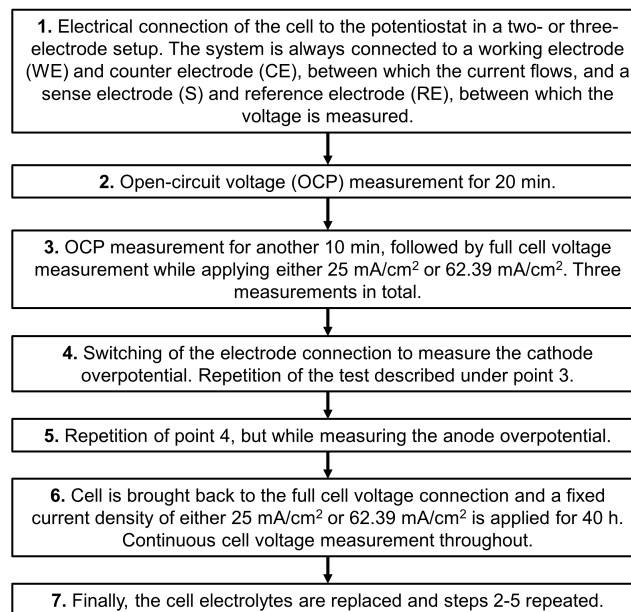


Figure 2.7: Galvanostatic electrolysis testing protocol

2.3.1. Blank Cell Tests

For all blank cell tests, the electrolysis cell displayed in figure 2.3 was used. After assembly of the cell, its inlets and outlets were subsequently connected to the electrolyte solutions as shown in figure 2.8.

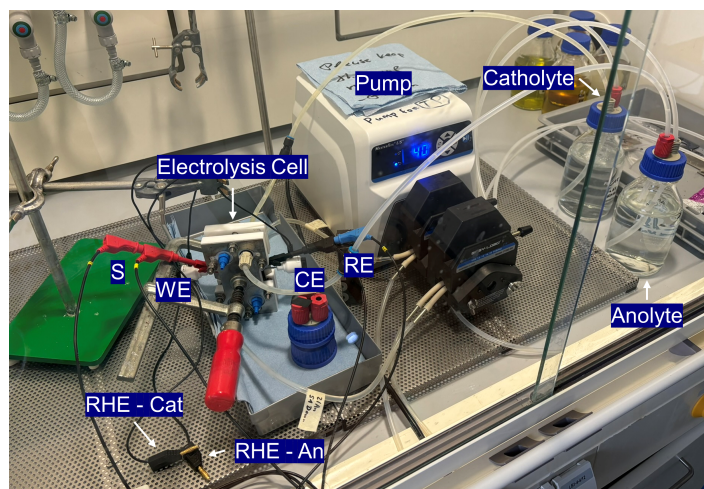


Figure 2.8: Blank Cell Electrolysis Test Setup

The figure shows the testing setup in two-electrode configuration, with WE & S connected to the SS anode, and CE & RE connected to the nickel cathode. After connecting the tubes to the cell inlets and outlets, the peristaltic pump was turned on and sodium phosphate buffer started circulating through each cell compartment. Both solutions were circulated through different bottles in order to avoid mixing of the gaseous hydrogen and oxygen products. Afterwards, electrochemical tests were performed on the cell as described in testing protocol B.2.

For the blank cell tests, both electrolyte solutions had a volume of 500 ml. This volume size was chosen to minimise changes in the solution concentrations during testing. As the blank cell design did not have any sort of external water flux into the system, water was continuously consumed during electrolysis. As such, the anolyte was expected to continuously lose water due to the water oxidation reaction, increasing its concentration. Based on a calculation of the expected water consumption, and aiming for the anolyte molarity change to stay below 5%, the chosen anolyte volume was attained.

2.3.2. Combined Cell Tests

After performing tests on the blank cell, the next step consisted of performing water electrolysis with artificial seawater. However, in order to do so, the in-situ water purification cell introduced in figure 2.2 had to be combined with the water electrolysis cell shown in figure 2.3. This connection was done by connecting the outlet of the electrolyte compartment of the water mass flux cell to the inlet of the anolyte compartment of the electrolysis cell. Thereby, the anolyte acted as a draw solution in the forward osmosis process, causing the water consumed during electrolysis to be continuously replenished. Afterwards, electrolysis tests were performed as detailed in testing protocol B.2. The entire test setup is shown in part (a) of figure 2.9. A top view of the serial connection of the two cells is provided in part (b) of the same figure.

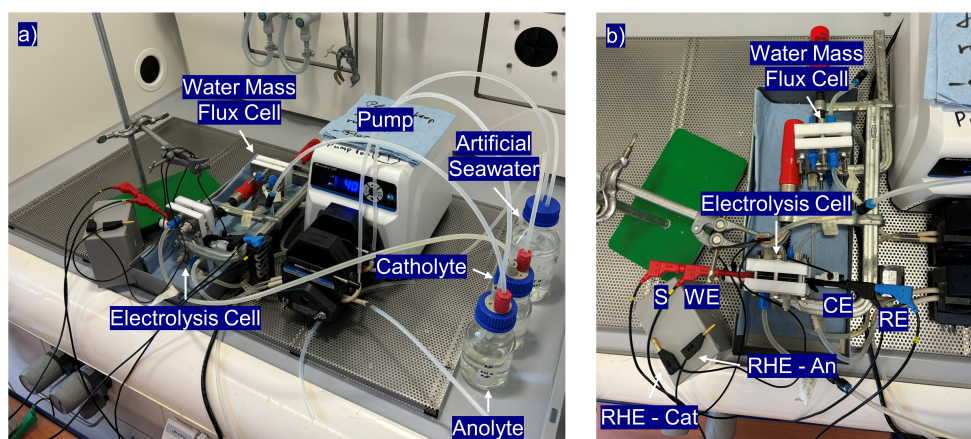


Figure 2.9: Combined cell test setup: (a) Overview of complete test setup including pump and liquids; (b) Top view of water mass flux cell and electrolysis cell in serial connection

As can be seen in part (a), artificial seawater was circulated along an FO membrane in one of the cell halves of the water mass flux cell. Simultaneously, sodium phosphate buffer was pumped through the other cell half. This buffer solution then left the water mass flux cell and subsequently entered the anodic flow chamber of the electrolysis cell. Likewise, sodium phosphate buffer was circulated through the cathodic flow chamber of the electrolysis cell. Again, both buffer solutions were fed back into separate bottles to avoid mixing gaseous hydrogen and oxygen.

During this process, the artificial seawater feed solution continuously lost water in the forward osmosis process. In order to prevent the feed solution from being concentrated too much during operation, the volume of the artificial seawater bottle was set to 500 ml. In comparison, the volume of both anolyte and catholyte were set to 250 ml, as both solutions were not expected to exhibit large molarity changes during testing. By using 500 ml of feed solution, and based on the expected water mass flux measured before, the feed solution molarity change was ensured to stay below 5%. This relative change was then considered to have a negligible impact on the driving force of the forward osmosis process (compare to section 2.2).

2.4. Solution Analysis

Both before and after testing, a variety of analysis tests were run on the solutions used during the galvanostatic tests. Every test described in this section was performed on each solution that had been used during the tests listed in table 2.1. First, subsection 2.4.1 introduces the methods used to measure pH, conductivity and weight of the solutions. Subsequently, subsection 2.4.2 focuses on the anion chromatography method used to measure changes in select ion concentrations for each solution. As such, the anion chromatography method is briefly explained, followed by an account of how the samples were prepared and analysed.

2.4.1. Conductivity, pH & Weight Measurements

Initially, the pH value and conductivity of each solution was measured using a Thermo Scientific Orion Star A200. Information on changes in pH levels were both valuable for attaining a clear picture on migration and diffusion processes that were taking place inside the cell, as well as to evaluate the observed corrosion mechanisms. Furthermore, information on conductivity changes was crucial in assessing shifts in the observed ohmic drop of the Nafion membrane. Before the initial use, the pH and conductivity probes were calibrated.

Next, the weight change of each solution was measured based the following considerations. First, information on solution weight changes allowed for the analysis of migration and diffusion processes during testing. Furthermore, measuring the weight changes also enabled comparing the observed mass flux over the FO membrane to the measured results during the water mass flux tests. To attain the weight changes, each solution weight was measured before and after testing using a two-digit

KERN PCB scale.

2.4.2. Anion Chromatography

For all tests a Metrohm 881 Compact IC Pro ion chromatograph with an anion column was used. The device has a lower ion detection limit of 0.5 parts per million (0.5 ppm) and an upper limit of 300 ppm. First, the device was calibrated for the detection of chloride, phosphate, and sulfate using standard solutions. These three anions were picked for observation for different reasons. Chloride was investigated as it is a key ion in corrosion processes, as specified in 1.2.1. The changes in phosphate concentration were measured to check for leaching processes through the FO membrane from the anolyte to the artificial seawater feed. Lastly, measuring sulfate allowed to identify for signs of Nafion membrane dissolution. Furthermore, both anions allowed for an investigation of migratory and diffusive processes within the tested cell. As already described in section 2.2, the concentration changes in sodium were not measured as it is present in high concentration in all used solutions.

Next, 10 ml samples were taken of either solution and diluted using DI water. The dilution was necessary for two reasons. First, to ensure staying below the upper detection limit of the device. Therefore, if the targeted ion concentration of the examined solution was expected to be above this threshold, it was diluted until the ion concentration fell below 300 ppm. Second, the used ion chromatograph had a limited pH operating window from 3-12. Therefore, if the investigated sample lay outside this pH range, it was similarly diluted until its pH value fell within the given boundaries.

Then, after placing the samples on the chromatograph, an initial DI water sample was tested. This was done both to clean the anion column from ion remnants of previous tests and to measure any background ions that might have been introduced into the sample during dilution. Finally, the diluted samples were placed on the chromatograph and tested for their anion concentration.

2.5. Surface Analysis

In order to attain in-depth information on the cell part surface changes that are evident after the galvanostatic electrolysis tests, scanning electron microscopy (SEM), energy dispersive X-ray analysis (EDX), and X-ray photoelectron spectroscopy (XPS) were performed on all electrodes, as well as some of the membranes used in the four tests. Additionally, these methods were also performed on the fresh electrodes and membranes, to compare the initial surface composition with that after testing. All three methods provided insight into the different compounds and species that deposited on the cell parts, which in turn helped to identify and differentiate the corrosion mechanism that caused the degradative processes.

First, subsection 2.5.1 briefly explains the working principle of SEM and EDX, describes the preceding sample preparation, and introduces the subsequent data analysis approach. Afterwards, subsection 3.4.5 provides a similar introduction into the XPS method with regard to data collection and analysis.

2.5.1. SEM and EDX Analysis

A scanning electron microscope operates by sweeping an electron beam across the surface of a small sample and measuring the signal response in form of either secondary or backscattered electrons [49]. By combining the information on the electron beam position with the receiver signal intensity, SEM allows for the generation of surface images at extremely small scales of down to 1 nm.

SEM is often combined with another method, called energy dispersive X-ray analysis. The combination of the two methods is logical, as EDX also uses a high-energy electron beam. In EDX, the electron beam is focused a small area of a sample, which causes the emission of X-rays from the investigated bulk material. The energy of these X-rays photons is characteristic for different atomic structures and thus allows for the identification of individual elements [49]. As EDX analyses X-rays that are generated in roughly 2 μm depth of the sample, it is generally considered a bulk characterization technique [50].

A JMS-IT700HR field emission microscope was used to analyse all samples. Before examining the metal electrodes using SEM/EDX, they were cleaned manually using DI water and isopropanol. This was done in order to remove water-soluble salt deposits that formed after disassembly of the cell, and which were not originally part of the electrode surface during testing. Lastly, all examined membranes were dried for 24 hours under a fume hood.

2.5.2. XPS Analysis

X-ray photoelectron spectroscopy is a widely used method to investigate the chemical composition of surfaces. XPS works by exposing a sample surface to monochromatic X-rays and analysing the energy of the electrons that are subsequently emitted by the sample. The X-ray photons used in XPS usually penetrate the sample up to a depth of between 1-10 micrometers [51]. As the energy of the emitted electron depends on the binding energy of the atomic orbital from which it is emitted, and as each element has a characteristic set of these binding energies, the method enables the identification of different elements in the investigated sample, similarly to the EDX method described in subsection 2.5.1. However, opposed to EDX, XPS also provides information on the chemical state of the elements, i.e., what other elements they are bonded to. It does so by analysing slight shifts in the binding energy of different elements that are due to variations in their chemical state, also referred to as chemical shift [52]. Thereby, the method allows for the identification of the different compounds that the sample surface consists of.

For all tests, a Thermo Scientific K-Alpha X-ray photoelectron spectrometer system was used. As sample preparation, 1x1 cm pieces were cut from the electrodes using a press brake. Next, the electrode pieces were fixed on a background metal plate using carbon tape, and the background metal clamped to a test plate. This test plate, containing all the investigated samples, was then placed in the machine for testing, with each sample being investigated separately. Inside the machine, each XPS sample was briefly etched for 30 s via an ion beam to eliminate influences from surface contaminations. After testing, the obtained results were analysed using different online databases and research papers.

3

Results and Discussion

This chapter presents and describes all results attained during the water mass flux tests introduced in section 2.2 and the electrochemical tests shown in table 2.1. First, the water mass flux test results are described in section 3.1. Afterwards, the electrochemical test results are presented in section 3.2. Finally, the analysis results of all solutions and cell parts following the electrochemical tests are introduced in sections 3.3 and 3.4.

3.1. Water Mass Flux Tests

Figure 3.1 shows the results attained during the initial water mass flux tests. Part (a) of the figure shows the average change in weight for both draw and feed solution over the three performed tests. Part (b) shows the average chloride concentration as measured in the draw solution before and after testing. While the phosphate concentrations were measured as well, they were found to be below the detection limit for all three feed solutions and are thus not displayed. Considering the sample dilution, the phosphate concentration thus stayed below 50 ppm for all tests. The results displayed in part (a) have already been corrected for weight changes caused by setup evaporation and ion diffusion.

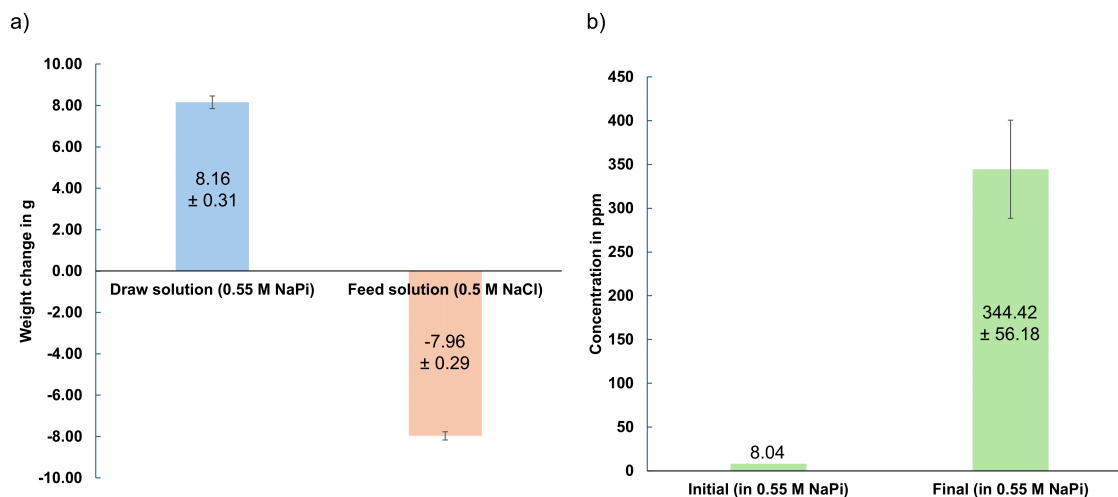


Figure 3.1: Water mass flux test results: a) Average draw and feed solution weight changes; b) Chloride concentration in the draw solution before and after testing

As is evident from part (a) of figure 2.2, the draw solution exhibits an average weight change of roughly 8.16 g over 24 hours. Conversely, the feed solution shows an average weight change of -7.96 g over 24 hours. The difference of approximately 0.2 g between the two solutions is expected to have been

caused by different amounts of liquid remaining in the test cell and setup tubing between the two solutions. Overall, the testing values show a relatively low variability, with relative errors staying below 4% for either solution.

Part (b) of figure 3.1 shows that there is a considerable change in chloride concentration in the draw solution. Compared to an initial concentration value of 8.04 ppm, the chloride concentration rises on average by around 336.38 ppm to 344.42 ppm. Here, the relative error is relatively large. Still, even when accounting for the standard deviation, the chloride concentration increases many times over. Thereby, an initial assumption is confirmed: the forward osmosis membrane does not represent a perfect ion barrier. However, judging from the considerably higher diffusion of chloride compared to phosphate, the selectivity of the membrane does seem to correlate with the size of the ion. Consequently, larger ions such as phosphate are effectively blocked from passing [53].

As shown in figure 2.1, the water mass flux test results were used to attain the maximum current density that the forward osmosis process can sustain. By taking the average draw solution weight change value shown in figure 3.1, this maximum current was calculated according to the equation below.

$$i_{max} = \frac{m_W \cdot F \cdot 2}{A_{geo} \cdot 3600 \left[\frac{s}{h}\right] \cdot 24[h] \cdot M_W} \approx 62.39 \frac{A}{cm^2} \quad (3.1)$$

where:

i_{max} = Maximum current density in A/cm²
 m_W = Water mass flux over 24 hours in g
 F = Faraday constant in C/mol
 A_{geo} = Geometric electrode area in cm²
 M_W = Molar mass of water in g/mol

An additional water mass flux test was performed using the FO membrane of the test with seawater at maximum current density. This particular FO membrane was used, as it shows visible signs of degradation after testing, as presented later in subsection 3.4. The results of this singular water mass flux test are shown in figure 3.2:

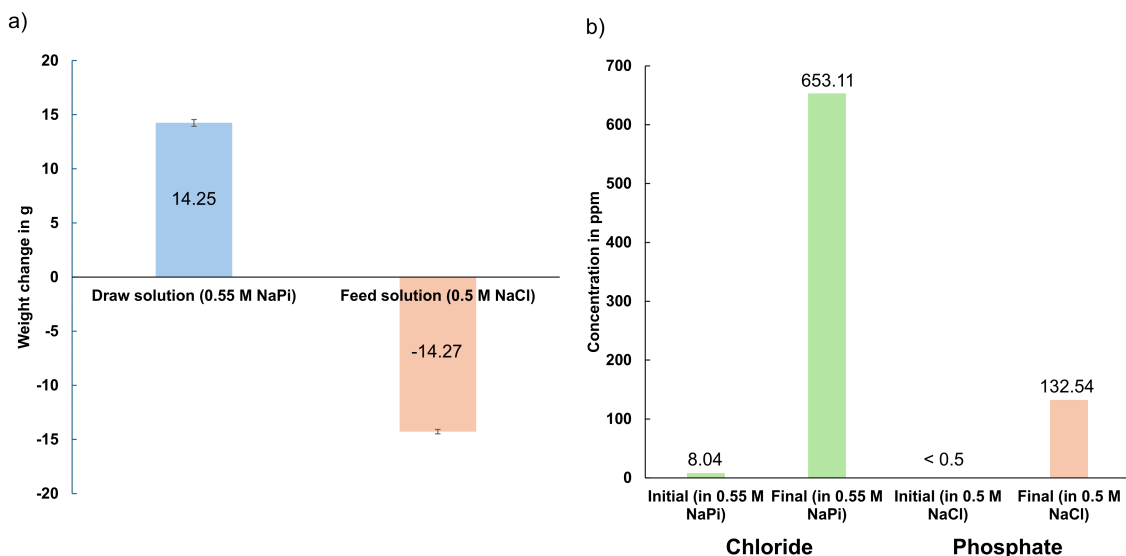


Figure 3.2: Used FO membrane water mass flux test results: a) Draw and feed solution weight changes; b) Chloride concentration in the draw solution before and after testing

As is evident from the figure, the observed water migration still occurred in the targeted direction, i.e., from the feed to the draw solution. However, at an observed draw weight increase of 14.25 g over

24 hours, this water influx was almost 75% larger than the average value observed for the fresh membranes used in figure 3.1. When looking at the anion chromatography results, the observed chloride influx to the draw solution has increased similarly. Compared to the test with fresh FO membranes, the chloride influx is almost 90% larger. Also, a comparably small concentration of phosphorus can now be measured in the seawater solution. Thus, the membrane pore size seems to have increased over the course of testing, as it shows an accelerated transfer of both water molecules and ions.

Finally, a water mass flux test was performed using an acidic draw solution made of 0.55 M sodium phosphate buffer at pH 3 and a new FO membrane. This test was designed to check if the FO membrane provides some sort of effective barrier for the diffusion of protons. Furthermore, the test served to check to what degree the water transport connected to proton diffusion impacts the targeted water mass flux. The results of the water flux test are shown in figure 3.3.

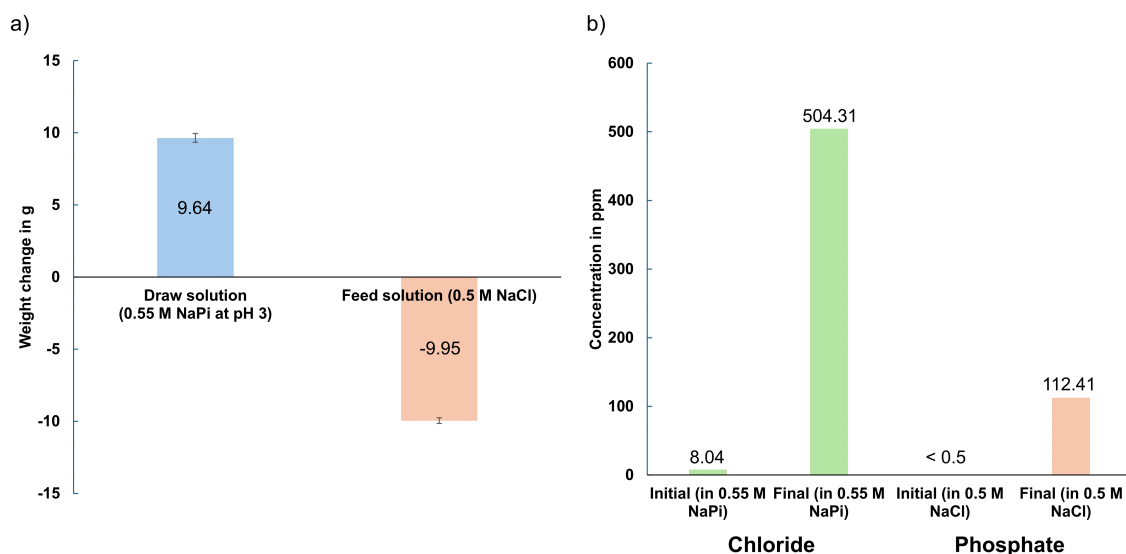


Figure 3.3: Water mass flux test results with pH 3 draw solution: a) Draw and feed solution weight changes; b) Chloride concentration in the draw solution before and after testing

Looking at the draw solution weight change shown in figure 3.3, the water mass flux still takes place from feed to draw solution. The total draw solution increase amounts to 9.64 g and is thus slightly larger than the average value found in test 3.1. This slight increase might be due to the larger osmotic pressure of the draw solution, caused by an increased concentration of protons or a change in buffer dissociation. Similarly, the chloride concentration after testing is larger than for the water mass flux tests with neutral buffer solution. As such, the chloride concentration has increased by roughly 496.27 ppm after 24 hours. Again, a comparably small concentration of phosphorus was detected in the final feed solution. Lastly, after testing the draw solution pH was found to be 3.15, compared to an initial pH level of 3.01. Similarly, the feed solution pH amounted to 3.45 after testing, compared to 6.65 before. Thus, the pH values of the two solutions are aligning. Consequently, the FO membrane does not pose a barrier for the exchange of protons between draw and feed solution. However, the proton exchange does not seem to impact the observed water mass flux in the system. At the same time, the chosen draw solution pH of 3 means that the proton concentration is still comparably small compared to the presence of other ions in the system.

3.2. Galvanostatic Electrolysis Tests

After attaining the maximum sustainable energy density, a variety of electrochemical tests were performed on the cells (see table 2.1). First, the continuous 40 h cell voltage measurements of these tests are shown and discussed in subsection 3.2.1. Afterwards, the cell voltage and its anode, cathode, and membrane contributions before and after testing are displayed and analysed in subsection 3.2.2.

3.2.1. Continuous Cell Voltage Measurements

This section introduces all electrochemical test results attained by following the test protocol introduced in B.2. Figure 3.4 shows the continuous voltage measurement for all four tests:

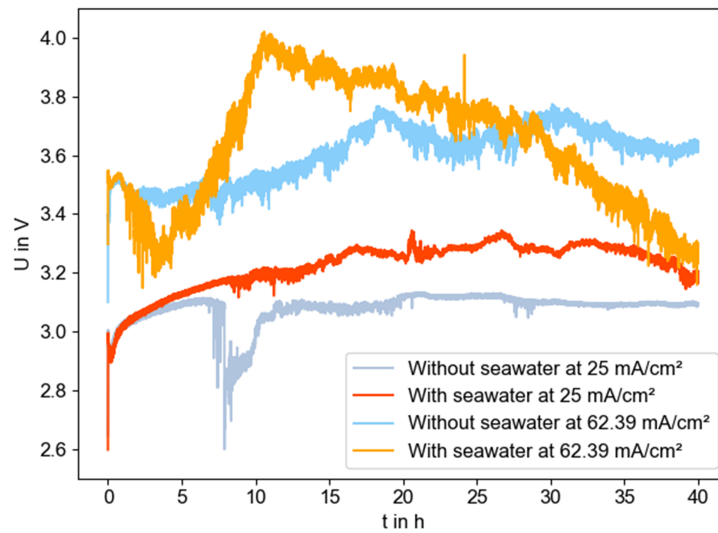


Figure 3.4: Continuous cell voltage measurement results

As is evident from figure 3.4, all four tests exhibit different cell voltage behaviours. Initially, both tests at low current density display rising cell voltages for roughly the first 7.5 hours. However, afterwards their behaviours diverge. While the test with seawater displays a continued cell voltage rise for circa 17 hours, the test without seawater shows a sudden drop in cell voltage. At its maximum, this drop amounts to roughly 0.5 V, or one-sixth of the total cell voltage. The entire drop is recovered within around four hours. After this point, the cell voltage remains stable until the end of the test. In comparison, the test with seawater shows a stable voltage for roughly 16 hours, after which it starts to decrease moderately by approximately 0.15 V. Overall, the cell voltage of the test without seawater rises from an initial 3 V to a final value of slightly below 3.1 V. The test with seawater exhibits a moderately larger increase from an initial 3 V to about 3.15 V.

Possibly, the sudden voltage drop observed by the test without seawater can be explained by the so-called blanketing effect sometimes observed in zero-gap electrolyzers. The blanketing effect describes that part of the electrode area facing the membrane becomes inactive due to coverage by a gas film trapped between electrode and membrane [54]. If this effect occurs, the cell voltage rises due to the reagents having to take a longer path through both the Nafion membrane and the liquid electrolyte before reacting. This might explain the initial rise in cell voltage observed during the first 7 hours of testing. Then, when part of the gas film coverage escapes suddenly, the cell voltage drops instantly due to additional, and energetically more favourable electrode area becoming available. Afterwards, the cell voltage slowly starts rising back to its original value, as the blanketing layer is reformed. Perhaps, this effect on a smaller scale can also explain the other, smaller voltage spikes and drops observed throughout testing.

Looking at the two tests at maximum current density displayed in figure 3.4, a considerably higher starting voltage is discernible for both tests. This increase in initial cell voltage was expected, as the cells are now operated at a higher current, which, among others, entails larger ohmic drops, as well as bubble and concentration overpotentials. However, the divergence in cell voltage behaviour is even stronger for these two tests. Initially, the two tests agree well with an initial brief cell voltage increase for the first two hours of testing. Afterwards, the cell without seawater exhibits a stationary period of roughly three hours. Then, its cell voltage starts climbing at a relatively constant rate from approximately 3.45 V to almost 3.8 V within the next fifteen hours. Following this period, the system settles into a steady state with periodic voltage fluctuations. These fluctuations are of an amplitude of roughly 0.2 V. At the end

of the test, the cell voltage has increase slightly from an initial 3.5 V to about 3.6 V. In comparison, the cell with seawater follows its initial brief voltage rise experiences by a voltage decrease of roughly 0.3 V during the next three hours of testing. Afterwards, the cell voltage starts rising rapidly for approximately 7 hours by more than 0.8 V. This rapid rise is followed by a consistent cell voltage decline of similar size. This final test is the only one exhibiting a smaller final than initial cell voltage, starting out at around 3.5 V and ending at approximately 3.3 V.

While no sudden voltage drop as for the lower current density can be observed, there are still considerable short-lived voltage drops throughout the entire testing period of around 0.1 V. Generally, the data is more noisy compared to the tests at low current density. This noise is attributed to the increased bubble formation at higher current density and the corresponding cycles of bubble formation and detachment.

Generally, only limited comments can be made on the causes of the different observed cell voltage trends. This is due to a lack of insight into the overpotential evolution of individual cell parts. While the test cell generally allows for anode and cathode overpotentials to be measured continuously and separately from the full cell voltage, time- and equipment constraints only allowed for the shown measurements of the full cell voltage. Still, some hypothesis can be formed as to the causes of the cell voltage changes.

Overall, the cell voltage breakdown tests before and after testing introduced in subsection 3.2.2 show a cell voltage increase for all tests. However, this final cell voltage differs from the final continuous cell voltage measurement in all cases. As the only change between the final continuous measurement and the voltage breakdown tests consisted of the change of electrolyte, some of the observed changes must be due to changes in the electrolyte pH and conductivity. Generally, for both tests at high current density the full cell voltage after changing the electrolyte is higher than before, whereas it is lower for both tests at low current density. As presented later on in section 3.3, large pH swings and conductivity changes are indeed observed for all tests. These conductivity increases are larger for the tests at high current density. This might be part of the explanation of why the cell voltages of the tests at high current density increase after exchanging the electrolyte.

Furthermore, the initial overpotential rise observed for all tests is attributed to a dissolution of the iron- and nickel-rich top layer of the stainless steel anode, and a decrease in membrane conductivity, both of which are discussed in-depth in subsection 3.2.2. In contrast, the later stagnation or even drop in total cell voltage is assumed to be due to the formation of a catalytically superior layer on the cathodes, similarly discussed in subsection 3.2.2. Naturally, the latter process occurs with a delay compared to the former, as it depends on the previous dissolution and migration of metal cations.

Another factor potentially influencing the voltage drop-off for the tests with seawater is the accumulation of chloride in the anolyte. As already shown in section 3.1, the FO membrane was found to be an imperfect ion barrier. Similarly, after the galvanostatic tests, comparably high chloride concentrations were found in the anolyte for both tests with seawater (see table 3.1). As can be seen in the chloride Pourbaix diagram in figure 1.4, at low pH values and positive applied potentials, this chloride undergoes oxidation reactions. These parasitic oxidation reactions are potentially more favourable energetically compared to the OER, explaining the observed decreases in cell voltage towards the end of the test, after chloride has gradually accumulated in the anolyte.

3.2.2. Cell Voltage Breakdown Measurements

Next, figure 3.5 presents the data of the measured cell voltages before and after testing, as well as their breakdown into anode, cathode, membrane, and thermodynamic contributions. Not all final cell voltage values shown in the figure correspond to the final cell voltages of figure 3.4. To explain these differences, it is crucial to remember that the cell voltage measurements in figure 3.4 were influenced by changes in the anolyte and catholyte conductivity. In contrast, the cell voltage in figure 3.5 was measured using fresh electrolyte. Likewise, it is important to note that the membrane overpotential, unlike the anode and cathode overpotentials, is a calculated value. This value was attained by subtracting the anode and cathode overpotentials, as well as the thermodynamic water splitting potential, from the measured cell voltage, as shown in equation 3.2.

$$\eta_M = U_{cell} - U_{th} - \eta_A - \eta_C \quad (3.2)$$

where:

η_M = Membrane overpotential
 U_{cell} = Cell voltage
 η_A = Anode overpotential
 η_C = Cathode overpotential
 U_{th} = Thermodynamic water splitting potential

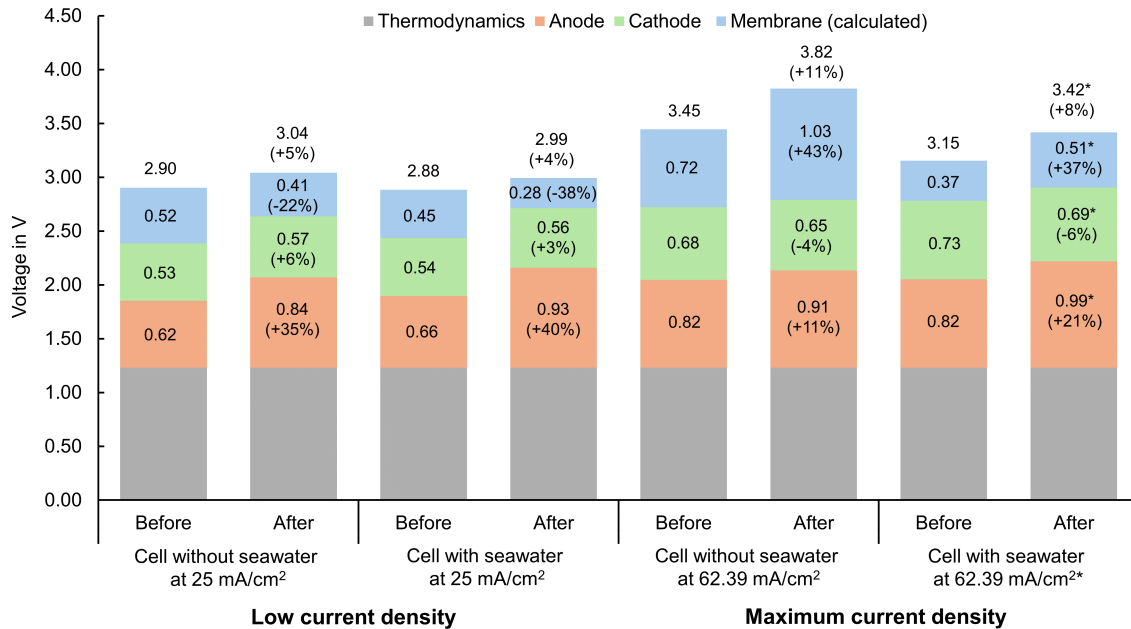


Figure 3.5: Initial and final voltage breakdown of all tests

The test results of the test with seawater at maximum current density are marked by an asterisk. Later on in subsection 3.3.3, significantly higher chloride concentrations were found for this test than anticipated. These high concentrations were attributed to an erroneous preparation of the artificial seawater solution used in this test. Thus, more chloride entered the anolyte than with a regular seawater solution. Consequently, the degradation results of this test should be treated with caution, as they potentially contain additional degradation caused by the abnormally high chloride concentration.

Evidently, both tests at low current density exhibit similar overpotential and voltage changes. For example, the anode overpotential increases in either case. The increase is slightly larger for the cell with seawater by an additional 5%. In contrast, the cathode overpotentials barely change for both tests. As such, the overpotentials increase only moderately, with the increase being an additional 3% bigger for the cell without seawater. Furthermore, either test exhibits an improvement for the membrane overpotential. For the test with seawater, this improvement is almost twice as large. Finally, the total cell voltage increase of the test without seawater is around 1% larger than for the setup with in-situ water purification. Generally, the cell voltage increases for both tests.

Crucially, the test with seawater at low current density initially exhibited lower overpotentials for both OER and HER compared to the previous state-of-the-art FO water electrolysis cell at equal current density. In the previous cell, overpotentials of 0.63 V and 0.83 V were observed for HER and OER, respectively [5]. These improvements were attributed to improved flow conditions, decreasing bubble and concentration overpotentials. After testing, only a cathode overpotential improvement remains.

Same as for the tests at low current density, both tests at the maximum current density exhibit an increase in anode overpotential. However, in comparison, the change in anode overpotential is almost twice as large for the test with seawater purification. In contrast, both tests show a decreasing cathode overpotential. The decrease is approximately 2% larger for the seawater test. Nonetheless, the

improvement in cathode overpotential is considerably smaller than the deterioration of the anode overpotential for either test. Next, both tests display similar increases in membrane overpotential. With an increase of around 37% for the test with seawater, and about 43% for the test without, these increases are also considerably outpace the observed growth anode overpotentials. Finally, the total voltages of both cells increase by 8% for the test with in-situ purification, compared to 11% for the test without.

Comparing the initial cell voltages of the test at maximum current density with seawater shown in figures 3.4 and 3.5, this test is the only one with a significant difference in starting voltage between the two datasets. However, these two values should coincide as they are both tested with fresh electrolyte. At a closer look, the initial cell voltage of part (b) matches well with the cell voltage attained after around 3 hours of testing. Thus, bubble formation that occurred as part of the voltage breakdown tests before continuous testing might have caused this difference in starting values.

Furthermore, comparing the initial and final cell voltages between the two tests at maximum current density in figure 3.5, both cells evidently exhibit an initial voltage difference of roughly 300 mV. However, initially both cells operate under the same conditions and should thus not differ in their starting voltages. The voltage shift remains throughout testing and is also visible in the final cell voltages. Here, the difference has grown to 400 mV, which might be due to the difference in voltage degradation. The offset between cell voltages is also represented in the difference in absolute membrane losses for the two tests. This is due to the membrane losses being a calculated value (see equation 3.2). Thus, the test with a larger cell voltage automatically displays larger membrane losses, provided anode and cathode overpotentials remain similar.

Generally, the constant shift in cell voltages is assumed to be due to inconsistencies in the manual assembly of the cell. During assembly, the perforated electrodes presented in figure 2.4 can shift slightly so that the holes of the two plates overlap to varying degrees. Ideally, the electrodes should overlap perfectly to ensure that the protons have the shortest conductive path through the membrane and to the electrochemically active electrode site. As the electrodes start shifting, however, this conductive path increasingly entails a lateral component and thus grows. Consequently, the ohmic losses by the membrane increase. This argument is also supported by the fact that the initial anode and cathode overpotentials of the two tests show only minor deviations.

Overall, high cell voltages can be observed even at low current densities. These high cell voltages are assumed to be at least partially influenced by the simultaneous occurrence of water oxidation and water reduction at anode and cathode, respectively. This is due to the partial proton migration displacement by migrating sodium cations. As shown in equation 2 and 3, the simultaneous occurrence of both processes causes the required cell voltage for water splitting to increase beyond 1.23 V up to a theoretical maximum of 2.058 V. The exact effect is difficult to gauge, however, as a mixture of proton reduction and water reduction occurs at the cathode. Therefore, the thermodynamic impact on cell voltage was still set to the original 1.23 for all tests.

In summary, all four tests exhibit a rise in total cell voltage. The voltage rise for the tests at higher current density are on average twice as large as for the tests at lower current density. This additional cell voltage increase was expected, as conditions for corrosion and other side reactions improve at higher applied voltages. Next, all tests exhibit a significant anode overpotential growth. The relative growth rates are considerably larger for the tests at lower current density.

Generally, the increase in overpotential of the anodes is assumed to be due to the dissolution of the nickel- and iron-rich top layer of the stainless steel electrode. While the tests at maximum current density exhibit stronger macroscopic corrosion, the SEM results shown later in subsection 3.4.1 clearly show that all electrodes experience extensive surface etching. The dissolution of metal cations into solution is also demonstrated by the change of anolyte colour after testing (addressed in subsection 3.3.1), as well as by the presence of iron on the nickel cathode after testing (see subsection 3.4.2). Lastly, figure E.1 in the appendix shows the elementary surface composition of 316L stainless steel. As is evident from that figure, the initial 100 nm of the SS surface are dominated by nickel, iron and oxygen. Based on this information, the nickel- and iron-based compounds which were previously found to be good catalysts for the acidic OER (see 2.5), are assumed to be etched away during testing. The remaining SS anode surface is assumed to contain a much larger chromium content, as predicted by figure E.1. However, nickel, iron, and their metal oxides are specifically the elements that cause SS

to exhibit good catalytic properties for OER (see 2.5). In comparison, chromium and chromium oxide are significantly worse OER catalysts. As such, researchers have shown that it is possible to improve the SS OER catalysis properties by removing chromium from its surface [55]. In consequence, the catalytic properties of the SS surface worsen and the anode overpotential rises. This hypothesis was confirmed by the XPS analysis results later introduced in subsection 3.4.5.

Similarly, all tests show either a significantly lower overpotential growth for the cathode, as is the case for the tests at low current density, or even a moderate decrease in overpotential, as is the case for the tests at high current density. Generally, cathode overpotentials were expected to increase during testing, as different species deposit on the electrode during reduction. Indeed, based on the SEM and EDX results shown later on in subsection 3.4.2, a variety of compounds form on the nickel cathode surface. These findings were confirmed, and in some cases corrected, by an additional XPS analysis in subsection 3.4.5. Overall, evidence was found for the formation of iron- and nickel phosphate, iron- and nickel-hydroxide, and iron oxide hydroxide. Among these, superior HER-catalysis properties have been reported for nickel hydroxide [56] and both metal phosphates [57][58]. For example, Mehdi et al. tested nickel phosphate nanowires for HER catalysis under alkaline conditions. The nickel phosphate nanowires also exhibited lower reaction overpotentials compared to bare nickel electrodes [58]. Thus, the much smaller increase or even decrease in cathode overpotential is attributed to the formation of a mixture of iron- and nickel-based compounds on the cathode surface. The greater improvement in cathode overpotential for the tests at higher current density is assumed to be due to the increased precipitate formation on the cathode.

Finally, the biggest difference between the two current density groups can be found in the membrane overpotential change. Generally, the tests at low current density exhibit a significant decrease in membrane overpotential. In contrast, the tests at high current density present an even larger increase in membrane overpotential. Overall, the test are in good agreement within each current density group, except for the difference in membrane overpotential at high current density, the reason for which has already been addressed.

Generally, the membrane overpotential was expected to grow during testing. This assumption was based on the fact that sodium, which is present in large concentrations in the used electrolyte, has been reported to lead to a decrease in Nafion proton conductivity [59]. This effect is due to the substitution of hydrogen on the Nafion sulfonic acid group by sodium cations. As explained in depth when addressing the observed anolyte weight changes in subsection 3.3.1, the large initial sodium to proton concentration ratio in the anolyte, combined with the presence of an electric field, are assumed to have lead to a large sodium flux from anolyte to catholyte. Thus, based on this sodium flux, the membrane overpotential was expected to increase for all tests, albeit in a smaller degree for the lower current density tests. Also, the occurrence of extensive membrane blockage by precipitate for all tests should have lead to an additional rise in ohmic drop. This additional drop is due to a shrinkage in active membrane surface through which the ions can migrate. These factors, however, only increase the conductivity decrease observed for the tests at high current density.

At low current density, the conductivity improvement might have been due to the acidification of the anolyte during testing. Nafion membranes are sometimes pre-treated in an acid bath to increase the degree of protonation, leading to a conductivity increase [60]. However, for the test in this research, the Nafion membranes are only soaked in water as a pre-treatment. Thus, the membranes might encounter increased protonation caused by the contact with the acidified anolyte. In that case, the decrease in conductivity observed for the test at maximum current density would be due to other factors, such as increase membrane blockage, outweighing the underlying conductivity increase. This hypothesis, however, requires additional research.

3.3. Solution Investigation

This subsection presents and discusses the results of all tests that were performed on the solutions before and after electrochemical testing. First, the results of the different anolyte solutions are introduced in subsection 3.3.1. Afterwards, subsection 3.3.2 compares the measurement results of the catholytes. Finally, subsection 3.3.3 discusses the seawater solutions used during the tests with in-situ seawater purification. Pictures of the solutions can be found in the appendix under figures C.1 to C.4.

Generally, all solution results of the test with seawater at maximum current density are marked by an asterisk. Later on in subsection 3.3.3, the chloride concentration in the seawater solution for this tests was found to be approximately twice as large as expected. This high concentration was attributed to an erroneous preparation of the artificial seawater solution used in this test. Thus, more chloride entered the anolyte than with a regular seawater solution. This change in testing conditions is important to note when evaluating the solution test results of the corresponding test.

3.3.1. Anolyte

Table 3.1 displays the pH, conductivity, weight, and ion concentration results for all anolyte.

Table 3.1: Anolyte solutions before and after testing

	Initial	CwoS LC	CwS LC	CwoS HC	CwS HC
Quantity:					
pH	7	1.67	1.62	1.67	1.27*
Conductivity [mS/cm]	44.13	22.09	28.09	25.55	51.58*
Weight [g] (without seawater)	535.7	466.11	-	441.69	-
Weight [g] (with seawater)	267.85	-	224.28	-	123.68*
Chloride [ppm]	25.19	9.81	579.5	8.6	9107.15*
Phosphate [ppm]	15553.01	14893.45	16619.28	16419.34	24841.91*
Sulfate [ppm]	0	6.53	12.47	5.97	35.53*

As is evident from the table, all anolytes experience a large negative pH swing during testing. This acidification leads to pH values ranging from 1.67 for the two tests without seawater down to 1.27 for the test with seawater at maximum current density. Furthermore, except for the test with seawater at maximum current density, all anolytes exhibit a considerable loss in conductivity. Between the three tests, this loss in conductivity amounts to almost half of the initial value. In contrast, the anolyte conductivity of the test with seawater at maximum current density increases slightly.

This conductivity anomaly for the test with seawater at maximum current density can be explained by the erroneous seawater concentration, which lead to a larger chloride influx into the anolyte. This is also confirmed by the much larger chloride concentration observed for the corresponding anolyte in table 3.1. Similarly, the concentration difference is assumed to have lead to a sodium influx into the anolyte. These combined effects explain the observed conductivity anomaly for the test with seawater at maximum current density.

Additionally, all anolytes show a weight loss over the course of testing. This weight loss is especially large for the test with seawater at maximum current density, where the final weight is approximately half of the starting value. The large weight loss of the anolyte for the test with seawater at maximum current density can also be explained by the erroneous seawater solution. At twice the targeted concentration, the seawater solution turned into the draw solution in the FO process due to its high solute concentration. Thereby, the water consumed in the anolyte during water oxidation was not replenished via forward osmosis in this test.

Generally, the occurrence of anolyte acidification can be explained by the ion migration within the cell. While the used Nafion membrane is optimised for the transfer of protons, it also provides a good conductivity for sodium cations. For this reason, Nafion is also used in chlor-alkali electrolysis, where sodium cations are the main migrating ion species [61]. Furthermore, sodium cations initially outweigh the concentration of protons in the pH 7 buffer electrolyte by a factor of roughly 10^6 . Thus, once a

voltage is applied to the cell and an electric field forms, the migration of sodium through the Nafion competes with the migration of protons through the membrane. Consequently, not all of the protons forming during water oxidation at the anode are able to leave the anolyte, leading to acidification of the solution. The weight loss observed for all anolytes is likewise attributed to the migration of hydrated sodium and hydronium cations.

Furthermore, considering the solution dilution during sample preparation, only the two tests with seawater show final chloride concentrations that exceed the lower detection limit of the anion chromatograph. The final chloride concentration of these tests ranges from around 580 ppm for the test at lower current density up to more than 9100 ppm for the test at maximum current density. However, the latter value is clearly influenced by the erroneous seawater solution preparation. None of the anolytes contains significant amounts of sulfate after testing. Additionally, the phosphate concentration differs slightly between the anolytes after testing. While the test without seawater at low current density displays a slight phosphate concentration loss, all other tests show either small or large phosphate concentration increases. The increase is especially large for the test with seawater at maximum current density. However, the large concentration increase is probably due to the relatively large weight loss of this solution during testing. Generally, no chemical explanation was found for the observation of a decreasing phosphate concentration for the test without seawater at low current density. Since the Nafion separating anolyte and catholyte is not conductive for anions, phosphate cannot be exchanged between the two solutions. Furthermore, the anolyte weight decreases for all tests, which should lead to a general increase in phosphate concentration. Thus, the deviation of this test is attributed to the relatively large inaccuracy of anion chromatography measurements at high ion concentrations.

Finally, the colour changes of all anolytes can be analysed. Pictures of the anolytes can be found in the appendix under figures C.1 to C.4. Generally, the anolyte colour after testing ranges from yellow for the test without seawater at low current density up to a dark orange for the test with seawater at maximum current density.

The anolyte discoloration after testing is assumed to be caused by dissolved metal cations. Figure A.1 in the appendix shows the Pourbaix diagrams for nickel, iron, and chromium - the three main components of the 316 SS anode. Under the observed strongly acidic conditions and a positive applied voltage above the OER line, nickel is expected to dissolve as Ni^{2+} . According to the colour scheme for transition metal ions shown in figure E.2, these nickel cations have a greenish colour. However, nickel is present at only relatively low concentrations in 316 SS (see figure 3.5). Next, according to the Pourbaix diagram of iron, it should react to iron oxide at the given pH values. However, assuming that locally the pH changes to even lower values, Fe^{3+} cations are formed. As iron is by far the most abundant element in 316 SS, these cations are also assumed to be the dominant species in solution. According to figure E.2, these Fe^{3+} cations have a yellow colour in solution, explaining the observation of yellow solutions. Lastly, chromium is expected to form chromic acid. In chromic acid, chromium ions are present as Cr^{6+} cations which, according to E.2, have a dark orange colour. The observed yellow colour at lower current densities is thus attributable to the high concentration of iron cations in solution. The stronger the observed corrosion, however, the more chromic acid is formed as the chromium-rich layers below the SS surface are dissolved (see figure E.1 in the appendix). Thus, anolytes increasingly start turning into a deep orange colour caused by the chromic acid as corrosive processes intensify. Furthermore, the solution colours generally intensify for the anolytes with a smaller volume due to the higher concentration of dissolved metal cations.

3.3.2. Catholyte

Next, table 3.2 displays the testing results for the initial and final catholytes.

Table 3.2: Catholyte solutions before and after testing

	Initial	CwoS LC	CwS LC	CwoS HC	CwS HC
Quantity:					
pH	7	11.39	12.82	12.1	12.91
Conductivity [mS/cm]	44.13	55.27	67.59	58.24	75.03
Weight [g] (without seawater)	535.7	579.22	-	595.12	-
Weight [g] (with seawater)	267.85	-	294.08	-	302.76
Chloride [ppm]	25.19	11.97	20.67	34.9	636.17
Phosphate [ppm]	15553.01	16973.04	14563.14	15789.09	14816.64
Sulfate [ppm]	0	7.8	4.67	11.31	10.89

Similar to the anolytes, all catholytes experience a large pH swing during testing. In case of the catholytes, however, this pH swing is positive and thus leads to an alkalisation of the solutions. Thus, the final pH values of the catholytes range from 11.39 for the test without seawater at low current density up to 12.91 for the test with seawater at maximum current density. In contrast to most of the anolytes, all catholytes exhibit a conductivity improvement during testing. This conductivity improvement is especially large for the tests with seawater purification, and largest for the one at maximum current density. Likewise, all catholytes show an increase in weight after the tests. The weight increase is larger for the tests at high current density compared to those at low current density.

The alkalisation of the catholytes is traced back to the same effect that causes the acidification of the anolyte. Since part of the proton transfer over the membrane is partially blocked by sodium cations, the HER reaction either starts consuming protons from the aqueous electrolyte or shifts to water reduction. In case of the former, protons are consumed and the pH balance thus shifted towards the alkaline. In case of the latter, water reduction leads to the formation of hydroxide ions, which similarly leads to an alkalisation of the catholyte. This process is aggravated by the fact that the Nafion membrane is not conductive for anions, thus trapping the hydroxide ions in the catholyte.

With regard to the ion concentrations after testing, almost all chloride and sulfate concentrations that were measured are below the anion chromatograph detection limit. There is one notable exception though. The test with seawater at maximum current density contains almost 600 ppm of chloride. This finding is surprising, as chloride is supposed to be unable to pass the negatively charged Nafion membrane. Two hypothesis are formed for this observation. Either, the concentration of chloride is evidence for a very small perforation of the Nafion membrane that occurs during testing. However, the observation that the pH shift between anolyte and catholyte is largest for this test, weakens this hypothesis. Second, chloride contamination might have taken place either during mixing of the solutions, or preparation of the anion chromatography samples. As all catholytes increase in weight, and as phosphate is unable to transfer between the two electrolytes, the phosphate concentration should generally decrease for all tests. However, the two tests without seawater both exhibit an increase in phosphate concentration. Again, this deviation from theory is attributed to the inaccuracy of anion chromatography measurements at high ion concentrations.

Finally, none of the catholyte solutions exhibits a significant discoloration after testing. While the catholyte solutions shown in figures C.2 and C.4 appear orange, this colour is due to suspended precipitate. When this precipitate eventually settled, the catholyte colours were likewise observed to be virtually unchanged. After a while, brownish precipitate can be recognised at the bottom of the catholyte

for multiple solutions, especially for the two at maximum current density. This precipitate is assumed to originate from the material depositing on the cathodes, some of which is washed off during electrolyte circulation. The composition of the precipitate is closer examined later on in subsection 3.4.2.

3.3.3. Artificial Seawater

Finally, table 3.3 introduces the solution testing results for the artificial seawater feeds:

Table 3.3: Artificial seawater solutions before and after testing

	Initial	CwS LC	CwS HC
Quantity:			
pH	6.65	2.34	1.84*
Conductivity [mS/cm]	51.89	51.92	89.21*
Weight [g]	509.45	511.93	584.22*
Chloride [ppm]	17389.054	16771.21	29978.29*
Phosphate [ppm]	0	91.73	223.686*
Sulfate [ppm]	0	10.90	8.211*

Similar to the anolytes, both seawater solutions experience a negative pH shift. However, this shift is not as large as the corresponding anolyte shifts. For example, while the anolyte for the test at low current density ends up with a pH of 1.62, the corresponding seawater solution reaches at a pH of 2.34. The same can be observed for the test at maximum current density, where the seawater attains a final pH value of 1.84 compared to 1.27 for the anolyte. Generally, the acidification of the seawater feed is unsurprising. As mentioned before in subsection 3.1, water mass flux tests already showed that the FO membrane does not pose a significant barrier for proton diffusion. Furthermore, the conductivity of the seawater of the test at low current density remains virtually unchanged over the course of testing. In comparison, the seawater feed of the test at maximum current density displays a significant conductivity increase. This conductivity increase was attributed to the massively increased chloride concentration caused by erroneous solution preparation. Finally, both seawater solutions experience an increase in weight. The weight increase is minimal for the test at low current density. For the test at maximum current density, however, the increase is substantial at almost 15%.

With regard to changes in ion concentration, small phosphate concentration increases can be observed for both tests. However, especially for the test at low current density, these values are at the lower limit of the detection range. As expected, the reverse diffusion of phosphate is relatively low compared to chloride, as already observed during the water mass flux tests. Looking at the chloride concentration changes, however, a large divergence can be observed between the two tests. The test at low current density sees a moderate decrease in chloride concentration. In contrast, the chloride concentration of the test at maximum current density almost doubles. As mentioned before, this observation is attributed to erroneous mixing of the seawater during the solution preparation.

Generally, the weight of both seawater solutions was initially assumed to decrease. As the solutions serve as feed solutions in the FO process, they were expected to continuously lose water to the anolyte. The weight increase of the test at maximum current density is easy to explain, considering the erroneous solution preparation. Due to the doubled molarity, and consequently the increase in osmotic pressure,

this solution turned into the draw solution for the FO process. Thus, the water started flowing out of the anolyte and into the seawater.

However, the artificial seawater solution also shows a slight weight increase for the test at low current density. This observation is hypothesised to be due to sodium migration within the cell. While the sodium concentration of the solutions was not measured, it should have exhibited a significant change between anolyte and catholyte during testing. As described before, the high initial sodium versus proton concentration in the anolyte, combined with the electric field over the Nafion membrane caused migration of sodium cations from the anolyte to the catholyte. This effect appears to be large enough to counteract the other effects that serve to increase the anolyte solute concentration, such as metal dissolution and water oxidation. For the test at low current density, this mechanism appears to align the osmotic pressures of the two solutions, as evident in the virtually unchanged seawater weight after testing.

3.4. Surface Analysis

After testing, all cell electrodes and membranes were investigated using SEM and EDX. With regard to the electrodes, SEM was used to examine changes in surface morphology, which might indicate changes of the electrochemically active surface area (ECSA). Furthermore, SEM allowed examining the membranes for surface changes such as fissures. In comparison, EDX was used to check for changes in the surface bulk composition of the electrodes and membranes. The central goal was to identify new chemical compounds that might explain changes in the catalytic properties of either type of electrode. Finally, all electrodes were investigated using XPS. This additional investigation was done to strengthen the findings of the EDX measurements. Furthermore, XPS allowed for the targeted composition investigation of a far smaller thickness of the surface areas.

3.4.1. Anode

First, the anodes are presented and analysed. Figure 3.6 shows the anodes of all four tests after testing, as well as the initial blank anode. It is important to note that these pictures were taken directly after disassembly of the cell, therefore the anodes had not yet been cleaned. Both membrane- and electrolyte-facing electrodes sides are shown.

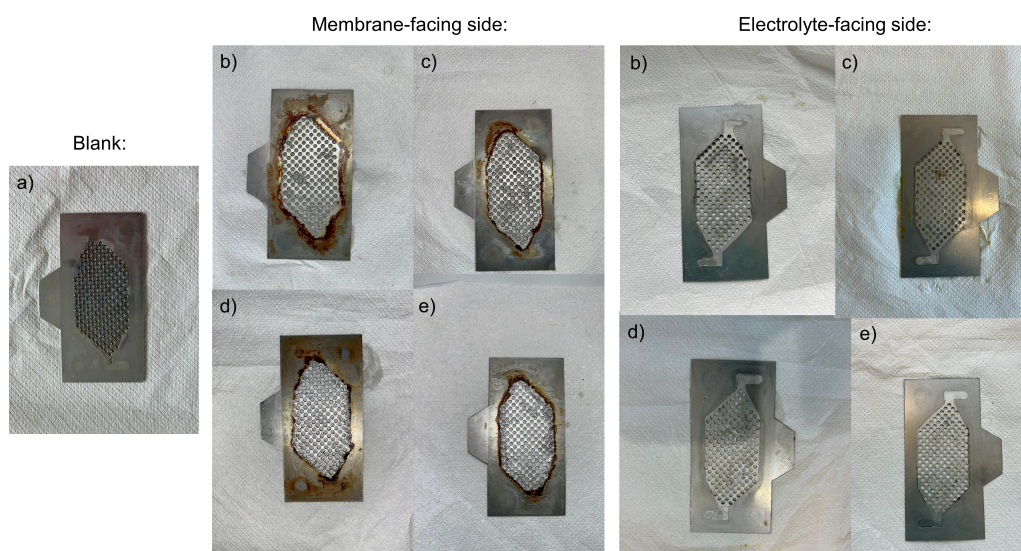


Figure 3.6: Blank anode shown in a); Anodes after testing: b) Cell without seawater at 25 mA/cm²; c) Cell with seawater at 25 mA/cm²; d) Cell without seawater at 62.39 mA/cm²; e) Cell with seawater at 62.39 mA/cm²

As is evident from figure 3.6, all four anodes show similar changes, albeit to varying degrees. As such, all anodes display signs of metal dissolution, usually concentrated along the edges of the flow field. Only for the anode of the test without seawater at low current density shown in part (a) of figure 3.6 does this metal dissolution concentrate at a location inside the flow field. While metal dissolution also

appears inside the flow field for some of the others tests, such as those shown in parts (c) and (d) of figure 3.6, this observed corrosion is merely in addition to the stronger edge-based dissolution. Lastly, the metal dissolution almost exclusively appears on the membrane-facing side of the anodes.

Generally, it is logical that most of the observed corrosion takes place at the flow field edges and on the membrane-facing side. Within the cell, the front side of the metal anode is supposed to sit flatly on the Nafion membrane. However, electrolyte is still able to flow through small openings between electrode and membrane. Otherwise, no metal dissolution could take place at the edges of the electrode. At the edges of the electrode, however, the electrolyte is assumed to be exchanged at a lower rate compared to the rest of the electrolyte pumped over the anode. This slower exchange is attributed to a comparably smaller gap between electrode and membrane at the electrode edges, caused by the cell frame which tightly seals the cell edges and allows for only minimal wiggle room between parts. Next, assuming that water electrolysis is nonetheless taking place at these locations, a gradual process of acidification and solute concentration takes place while water is consumed and protons formed during the OER. In case of the tests without seawater, this local pH shift enables the break-down of the passivation layer on top of the stainless steel. In case of tests with seawater, a mixture of the acidification combined with locally high concentrations of chloride accelerates this process. This hypothesis is also supported by the observation that both anodes of the tests with seawater exhibit stronger metal dissolution than their current-equivalent counterparts without seawater. Both corrosion processes are boosted by the general acidification of the anolyte, described and explained later in subsection 3.3.1.

Furthermore, for all tests there is brownish precipitation along the edges of the flow field, where the gasket separated the electrode from the frame and the manifolds. While is some variation in the size of the affected area, as can be seen by comparing part (a) and (d) of figure 3.6, none of the tests exhibit brownish deposition within the flow field.

Based on the SEM and EDX results of the affected anodes introduced later in figure 3.9 and table 3.6, this brownish deposition layer is assumed to be made of iron(III) oxide. Generally, the observation of an iron oxide layer close to the metal dissolution spots is to be expected, as the proximity allows for a relatively quick and stable cation diffusion between oxidation and reduction locations. Furthermore, plenty of oxygen is available at the anode for the metal cation reduction to take place. Nonetheless, it seems surprising that none of the brownish precipitate is present inside the flow field, where most of the oxygen is expected to form. Possibly, the continuous flow across the electrode does not allow the oxygen to be present long enough for the reduction to take place inside the flow field. In comparison, the oxygen bubbles might remain longer at the electrode edges, where additional surface area is present for the bubble to remain attached to.

Next, to evaluate the surface structure changes appearing on the cell parts, and to characterise the identity of the brownish precipitate, EDX and SEM tests were performed. A total of three types of spots were investigated for each anode.

The first location, henceforth referred to as 'no corrosion', was chosen at anode locations seemingly unscathed by metal dissolution. Thus, the expectation was to find a comparably unchanged metal surface morphology and composition. These locations also served to check if metal dissolution exclusively appeared at the macroscopic etching spots that are clearly visible in figure 3.6. Figure 3.7 displays the SEM results for the anode locations 'no corrosion'. Table 3.5 displays the corresponding EDX results. The exact locations on the anodes that were investigated can be found in the appendix under figure D.2.

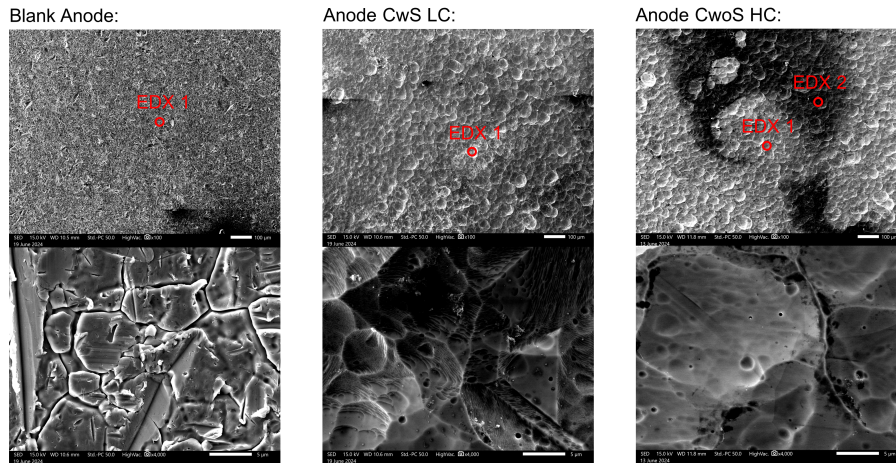


Figure 3.7: SEM results of the anode location 'no corrosion'

First, looking the blank anode morphology shown in figure 3.7, the SS anode initially consists of a complex surface structure with an uneven surface. As such, no clear patterns can be distinguished. After testing, a markedly different surface structure can be recognised, showing evidence for widespread metal etching. Therefore, as opposed to the initial expectation, metal dissolution does not exclusively appear in the macroscopic etching structures seen in figure 3.6. Furthermore, comparing the SEM pictures of the tested anodes with the blank anode, the metal surface changes from a fissured and complex morphology to a comparably smooth one.

Table 3.4: EDX results of the anode location 'no corrosion'

	EDX Spot:						
	Blank - EDX 1	Blank - Area	CwS LC - EDX 1	CwS LC - Area	CwoS HC - EDX 1	CwoS HC - EDX 2	CwoS HC - Area
Element [in Atom%]:							
Fe	62.11±0.79	60.46±0.78	61.50±0.77	54.83±0.71	65.50±0.88	58.63±0.82	56.65±0.79
Cr	16.21±0.33	16.18±0.33	16.93±0.33	15.30±0.31	18.47±0.39	16.15±0.36	14.92±0.33
Ni	8.28±0.37	8.64±0.38	7.95±0.36	7.78±0.34	8.59±0.41	7.46±0.38	7.31±0.37
O	-	4.37±0.25	4.80±0.25	9.23±0.31	-	13.36±0.40	8.53±0.33
C	10.68±0.35	8.04±0.31	6.19±0.27	6.59±0.27	5.42±0.28	-	9.44±0.35
P	-	-	-	1.28±0.09	-	1.72±0.11	1.26±0.09
Na	-	-	-	2.26±0.18	-	-	-
Mo	1.39±0.08	1.12±0.07	1.13±0.07	0.96±0.06	1.31±0.08	1.24±0.08	-
Si	0.76±0.09	0.74±0.09	0.83±0.09	0.87±0.09	0.71±0.10	0.56±0.09	0.99±0.10
Mn	0.56±0.11	0.45±0.11	0.68±0.11	0.92±0.12	-	0.88±0.13	0.89±0.13

Next, analysing the EDX results of the blank anode, the surface layer initially consists of an alloy of iron, chromium, and nickel. Of the three elements, iron is by far the most common element with atomic percentages above 60%. Iron is followed in frequency of occurrence by chromium at around 16%, and nickel with in slightly above 8%. This composition is in line with the expectation for 316 stainless steel. Furthermore, significant quantities of carbon and oxygen are present. While the carbon content is much higher than expected for stainless steel, carbon is a common contaminant in surface analyses due to its general ubiquity. Also, the samples are fixed to the sample mount using carbon tape, thus adding another potential carbon detection source. Therefore, the carbon contents are generally ignored in the analysis of this research.

After testing, the oxygen content of either examined anode has approximately doubled. Additionally, an EDX area scan shows decreased concentrations of iron, chromium, and nickel for either sample after testing. In general, the area EDX results of the two tested anodes agree quite well within the given standard deviations. Furthermore, the anode of the test without seawater at high current density

displays significantly darker surface spots. Based on the EDX results, these spots contain a higher oxygen content than the brighter surface areas. Thus, the dark colour is attributed to a higher degree of metal oxidation at these locations. The small amounts of sodium and phosphorus that are measured after testing are assumed to be caused by salt formation. However, as the used sodium phosphate buffer is soluble in water, these salts are assumed to have formed after testing.

The second investigated location was chosen at the clearly visible etching spots on all anodes. This location is thus referred to as 'strong corrosion'. Due to the strong etching of the material, a decrease in iron and nickel concentration were expected at this location. Also, an increase in chromium content was assumed. These hypotheses were based on the typical surface layer composition of 316L SS shown under figure E.1 in the appendix. Figure 3.8 displays the SEM results for the anode location 'strong corrosion'. Again, the corresponding EDX results are provided separately in table 3.6. The exact locations at which the analyses were performed can be found in the appendix under D.3.

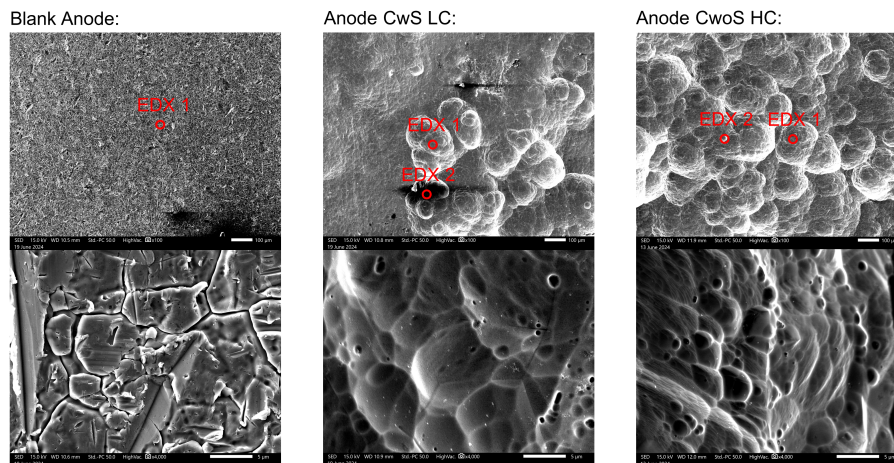


Figure 3.8: SEM results of the anode location 'strong corrosion'

Compared to the results shown in figure 3.7, the SEM pictures of figure 3.8 exhibit much larger etching diameters. Furthermore, looking at the SEM pictures at highest magnification, the surface structure has again changed from a fissured and complex morphology to a more coherent one. As such, round structures of a range of sizes can be distinguished.

Table 3.5: EDX results of the anode location 'strong corrosion'

Element [in Atom%]:	EDX Spot:								
	Blank - EDX 1	Blank - Area	CwS LC - EDX 1	CwS LC - EDX 2	CwS LC - Area	CwoS HC - EDX 1	CwoS HC - EDX 2	CwoS HC - Area	
Fe	62.11±0.79	60.46±0.78	66.00±0.86	68.63±0.88	60.34±0.78	65.90±0.90	64.64±0.87	62.10±0.86	
Cr	16.21±0.33	16.18±0.33	18.77±0.38	18.98±0.38	16.73±0.34	18.74±0.39	18.32±0.38	17.47±0.38	
Ni	8.28±0.37	8.64±0.38	7.83±0.38	9.43±0.42	8.18±0.37	8.27±0.41	8.39±0.40	8.95±0.42	
O	-	4.37±0.25	-	-	5.12±0.26	-	-	-	
C	10.68±0.35	8.04±0.31	5.07±0.26	-	6.04±0.27	4.14±0.25	6.65±0.30	8.57±0.35	
P	-	-	-	-	0.61±0.0700	-	-	-	
Mo	1.39±0.08	1.12±0.07	1.34±0.08	-	1.17±0.07	1.31±0.08	1.12±0.08	1.03±0.07	
Si	0.76±0.09	0.74±0.09	-	0.58±0.09	0.78±0.09	0.86±0.10	-	0.67±0.10	
Mn	0.56±0.11	0.45±0.11	1.00±0.14	1.30±0.15	1.02±0.13	0.78±0.14	0.88±0.14	1.22±0.15	
S	-	-	-	1.09±0.08	-	-	-	-	

Looking at the accompanying EDX results, both tests display a complete lack of surface oxygen at the heavily etched locations. While an area EDX scan for the test with seawater at low current density does find evidence for oxygen, this oxygen is probably present in the uncorroded upper left part of the

SEM picture. This assumption is backed by the observation that, when analysing the etched locations individually, no trace of oxygen was found. Thus, with increasing depth of the surface etching, the material appears to lose its oxidised layer, which then does not re-form. At the locations with heavy corrosion, both tests also contain higher amounts of both chromium and iron, compared to the blank anode. Finally, while the corresponding area scans do not show a significantly higher iron content, their chromium concentration is increased, albeit only moderately.

Combining the findings of the locations 'no corrosion' and 'strong corrosion', the anode surface was found to be etched to a far larger extent than originally expected (see figure 3.7). Typically, these etching processes should be accompanied by higher chromium contents, as well as lower iron and nickel contents, as predicted by figure E.1. Higher chromium contents, however, were only found for the location 'strong corrosion', and also there only to a small degree. The general lack of evidence for the hypothesis was attributed to the investigation method. As mentioned before, EDX is commonly considered a bulk characterisation method and as such samples signals up to a depth of 2 μm . However, the expected changes in surface composition are expected at around one-tenth of that depth. Therefore, the EDX results cannot be considered representative of only the immediate top layer composition. This explanation is also supported by the XPS findings later introduced in subsection 3.4.5. When analysing the 'no corrosion' location via XPS, which only analyses the immediate surface layer, lower nickel and iron concentrations and a higher chromium content are found.

The final investigated anode location is henceforth referred to as 'brown precipitate (anode)'. This location was chosen at the brownish deposit that had formed around the edges of each tested anode. Before the investigation, the brown precipitate was assumed to be made of iron oxide due to its strong rust resemblance. Figure 3.9 and table 3.6 present the SEM and EDX results taken at the anode location 'brown precipitate (anode)', respectively. The exact anode locations can be found in the appendix under D.4.

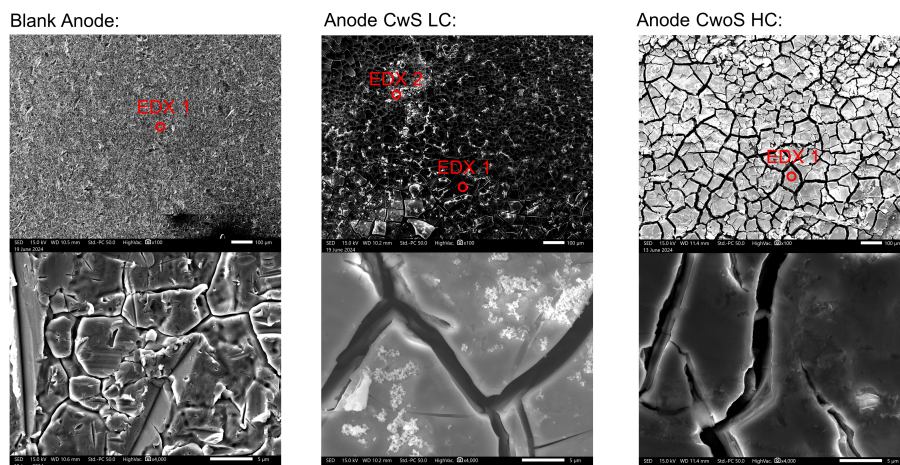


Figure 3.9: SEM results of the anode location 'brown precipitate (anode)'

The SEM pictures shown in figure 3.9 show a markedly different surface morphology compared to the etched locations. As such, the surface consists of a relatively homogeneous but fissured top layer with smaller bright spots all across. At higher magnification, these bright spots appear to be salt crystals. This assumption is also confirmed by the EDX results shown in table 3.6, which show comparably high concentrations of phosphorus, sodium, and oxygen for the bright spots. While the surface morphologies of the two investigated locations agree quite well, they exhibit a significant difference in contrast. This difference in contrast is attributed to the higher presence of bright salt crystals for the test with seawater at lower current density. A higher presence of these bright crystals causes the SEM software to automatically adjust the contrast level, letting the background appear darker.

Table 3.6: EDX results of the anode location 'brown precipitate (anode)'

Element [in Atom%]:	EDX Spot:		CwS LC - EDX 1	CwS LC - EDX 2	CwS LC - Area	CwoS HC - EDX 1	CwoS HC - Area
	Blank - EDX 1	Blank - Area					
Fe	62.11±0.79	60.46±0.78	16.75±0.32	6.79±0.16	17.03±0.33	20.80±0.40	21.93±0.41
Cr	16.21±0.33	16.18±0.33	0.88±0.07	1.35±0.06	1.91±0.09	-	0.49±0.06
Ni	8.28±0.37	8.64±0.38	0.46±0.08	0.61±0.06	0.57±0.09	3.11±0.20	3.28±0.20
O	-	4.37±0.25	67.85±0.60	65.38±0.49	65.11±0.60	67.49±0.65	58.43±0.64
C	10.68±0.35	8.04±0.31	-	7.33±0.21	-	-	6.53±0.25
P	-	-	9.10±0.15	10.87±0.13	8.61±0.15	3.08±0.11	3.13±0.11
Na	-	-	4.26±0.16	7.12±0.15	5.99±0.20	4.59±0.20	4.00±0.19
Mo	1.39±0.08	1.12±0.07	-	-	-	-	-
Si	0.76±0.09	0.74±0.09	-	-	-	0.40±0.05	1.00±0.07
Mn	0.56±0.11	0.45±0.11	0.70±0.07	0.30±0.04	0.79±0.08	0.52±0.07	0.44±0.07
Ca	-	-	-	0.25±0.03	-	-	-
Mg	-	-	-	-	-	-	0.76±0.08

As is evident from the EDX results of table 3.6, the surface of both tests is characterised by very high contents of oxygen when compared to the blank anode. Furthermore, the area scans of both tests show significant amounts of iron, phosphorus, and sodium. Assuming the phosphorus and sodium to be present in the form of salt crystals, this indicates the formation of an iron oxide layer with additional salt precipitation. This assumption is supported looking at the Pourbaix diagram of iron (part (b) of figure A.1 in the appendix). Under highly acidic conditions with a pH between 1-2, which are observed for all test analytes, and high positive potentials, the formation of iron(III) oxide is favoured. The potential formation of iron(III) oxide also fits to the observed dark-brown colour of the deposited layer.

3.4.2. Cathode

After focusing on the anodes, figure 3.10 presents the cathodes of all four tests after testing compared to the initial blank nickel electrode. Again, it is important to note that these pictures were taken directly after disassembly of the cell, therefore the cathodes had not yet been cleaned.

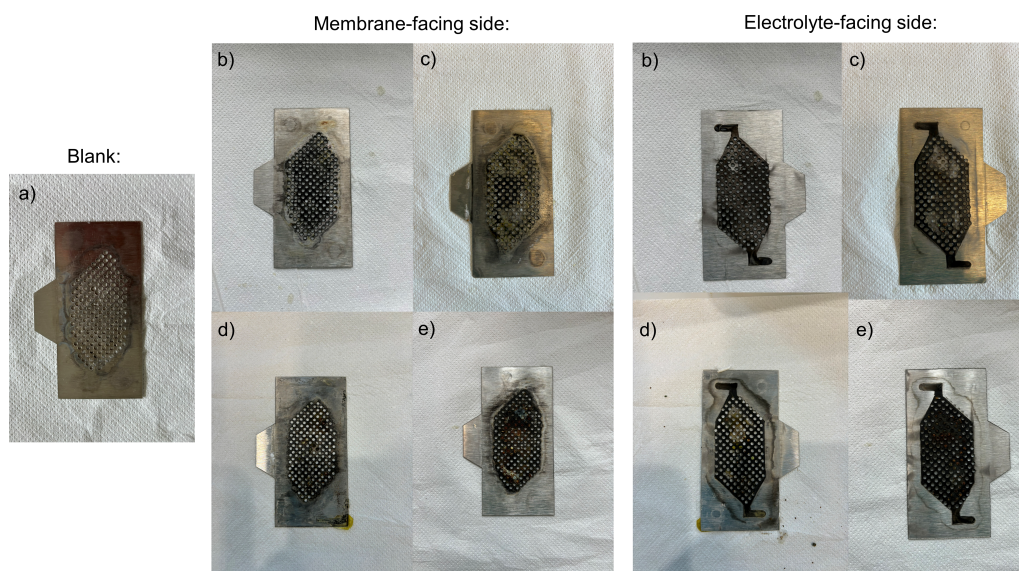


Figure 3.10: Blank cathode shown in a); Cathodes after testing: a) Cell without seawater at 25 mA/cm²; b) Cell with seawater at 25 mA/cm²; c) Cell without seawater at 62.39 mA/cm²; d) Cell with seawater at 62.39 mA/cm²

Generally, all four tests exhibit similar behaviour. For all tests, the changes to the cathode surface concentrate on the area inside the flow field. Unlike for the anodes in figure 3.6, there is no discernible

difference at the flow field edges of the electrodes. In general, a black layer has formed over most of the pure nickel after testing on both the membrane- and electrolyte-facing sides. At those areas where no black precipitate is visible, such as for part (b) of figure 3.10, this is due to the precipitate having remained on the Nafion after separation of the two parts (see figure 3.15). At the locations where the black layer has been removed, a slightly greenish layer can be recognised. For both tests at low current density presented in part (a) and (b) of figure 3.10, the perforations show little deposition and remain largely unblocked. In contrast, the two tests at higher current density contain blocked holes. The number of blocked perforations is largest for the test with seawater at high current density shown in part (d). Generally, the holes are blocked by deposited material whose colour ranges from black and dark brown to yellow-green.

Again, the most interesting locations of all cathodes were investigated using SEM and EDX. In total, four locations were examined. First, those nickel cathode locations after testing with a slight grey colour were investigated. These locations are henceforth referred to as 'light grey'. Due to their resemblance to the pristine nickel cathode, these locations were expected to show little signs of corrosion, but possibly additional elemental nickel deposition. Figure 3.11 displays the SEM results for the location 'light grey'. Table 3.7 provides the corresponding EDX results of the marked spots. Lastly, figure D.5 in the appendix shows the exact investigated locations.

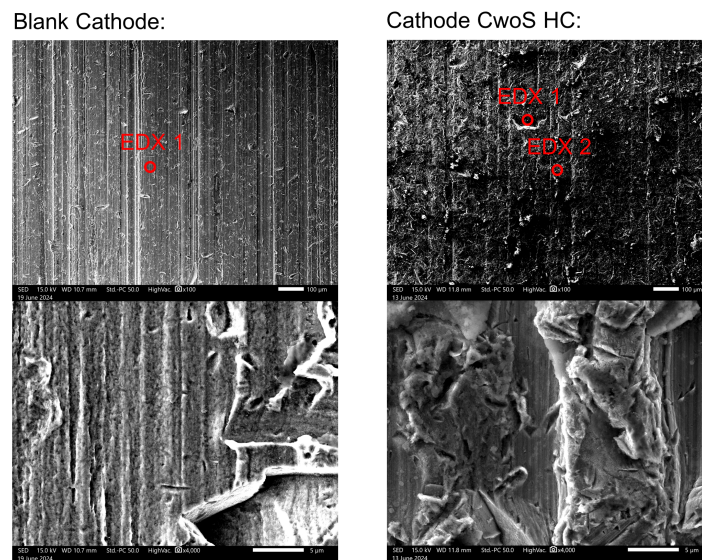


Figure 3.11: SEM results of the cathode location 'light grey'

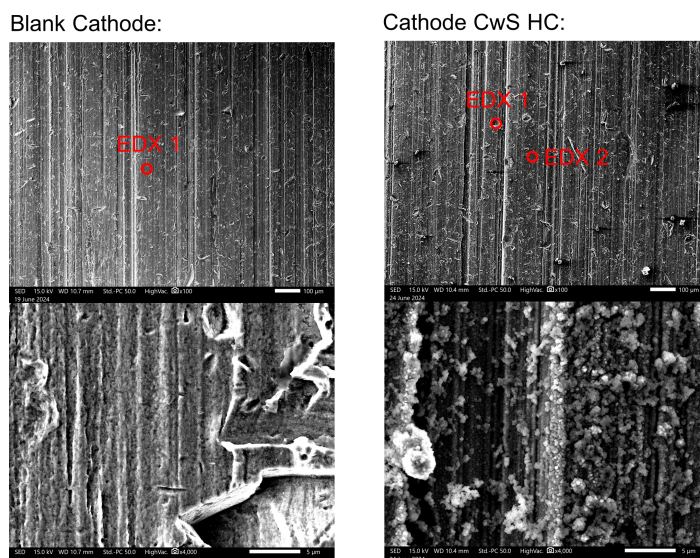
As is evident from the SEM pictures of figure 3.11, the cathode initially exhibits a relatively homogeneous surface, divided by vertical stripes of varying depth. After testing, the surface morphology of the cathode has changed into a much more rugged one with complex three-dimensional structures, which indicates the formation of additional surface area.

Table 3.7: EDX results of the cathode location 'light grey'

	EDX Spot:				
	Cathode - EDX 1	Cathode - Area	CwoS HC - EDX 1	CwoS HC - EDX 2	CwoS HC - Area
Element [in Atom%]:					
Ni	91.30±1.21	83.07±1.12	85.68±1.24	33.28±0.61	54.96±0.89
C	6.57±0.32	13.76±0.44	-	11.84±0.34	7.89±0.33
O	2.13±0.18	2.57±0.19	12.53±0.40	48.93±0.62	32.86±0.58
Fe	-	-	1.15±0.12	2.87±0.14	2.18±0.14
Cr	-	-	-	0.34±0.05	-
P	-	-	0.65±0.08	2.05±0.09	1.55±0.10
Si	-	0.59±0.09	-	0.69±0.07	0.56±0.08

Analysing the blank cathode composition shown in table 3.7, EDX area analysis shows a surface layer concentration of nickel ions of above 83%. Locally, the nickel concentration reaches even higher purities. Lastly, some impurities such as carbon, oxygen, and silicon are present. After testing, significantly larger oxygen concentrations are present compared to the blank cathode. These results suggest that a large amount of nickel oxide has formed on the surface compared to the initial cathode. Also, some small amounts of iron and phosphate are present. Crucially, the detection of iron on the previously iron-free nickel cathode means that during operation iron cations have had to dissolve into the anolyte, migrate through the Nafion, and finally deposit on the cathode.

Next the black layer clearly visible on all cathodes in figure 3.10 was examined. Initially, the layer was assumed to be made of a mixture of iron and nickel oxides. Figure 3.12 presents the SEM results of the location 'black' shown in the appendix under figure D.6. Furthermore, table 3.8 displays the accompanying EDX data.

**Figure 3.12:** SEM results of the cathode location 'black'

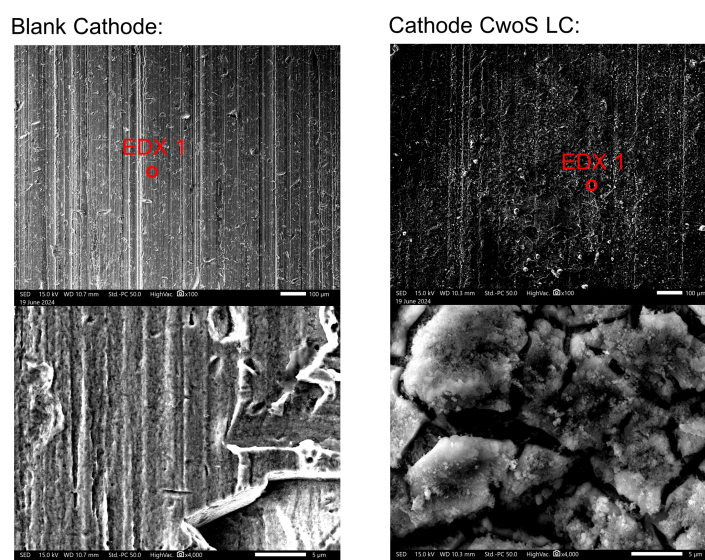
As evident from figure 3.12, the surface morphology has changed after testing. As such, the surface is now covered by small crystalline shapes of varying size. However, the underlying nickel structure is still clearly visible, as are the vertical stripes marking the initial surface.

Table 3.8: EDX results of the cathode location 'black'

Element [in Atom%]:	EDX Spot:				
	Cathode - EDX 1	Cathode - Area	CwS HC - EDX 1	CwS HC - EDX 2	CwS HC - Area
Ni	91.30±1.21	83.07±1.12	49.06±0.80	27.13±0.54	26.46±0.52
C	6.57±0.32	13.76±0.44	-	-	5.15±0.22
O	2.13±0.18	2.57±0.19	30.88±0.52	47.85±0.57	45.26±0.55
Fe	-	-	16.52±0.36	16.49±0.33	14.90±0.30
Cr	-	-	-	0.51±0.06	0.49±0.06
P	-	-	2.20±0.11	3.87±0.12	3.81±0.11
Na	-	-	-	2.60±0.17	2.66±0.17
Si	-	0.59±0.09	-	-	-
S	-	-	1.34±0.08	1.35±0.07	1.27±0.07
Mn	-	-	-	0.20±0.05	-

Looking at the EDX results of table 3.8, the nickel concentration after testing has dropped massively. Simultaneously, the oxygen content has increased strongly. Remarkably, the location displays the highest iron concentration of all investigated cathode locations. The presence of both sodium and phosphate at some spots further confirms the formation of salt crystals. Originally, the combination of these findings were attributed to the formation of a mixture of nickel- and iron oxides, including, possibly, the formation of combined nickel iron oxides. However, based on the XPS results of the same location introduced in chapter 3.4.5, the black layer is made of a mixture of iron- and nickel hydroxide, as well as iron- and nickel oxide hydroxide.

Next, the SEM results of the location henceforth referred to as 'light green' are shown in figure 3.13. As indicated by the name, this location was chosen on the green cathode spots after testing. Judging from the colour of the precipitate, these spots were assumed to provide evidence for the formation of nickel oxide on the cathode. The corresponding EDX results are given in table 3.9. The exact locations can be found under figure D.7 in the appendix.

**Figure 3.13:** SEM results of the cathode location 'light green'

After testing, the surface morphology of the cathode has changed into a fissured structure. Zooming into the picture, large surface structures can be identified that are made of smaller individual units and separated by comparably large gaps. As no evidence of sodium was found in the EDX results given under table 3.9, the smaller top units visible in the structures are not attributed to salt formation.

Table 3.9: EDX results of the cathode location 'light green'

	EDX Spot:			
	Cathode - EDX 1	Cathode - Area	CwS LC - EDX 1	CwS LC - Area
Element [in Atom%]:				
Ni	91.30±1.21	83.07±1.12	20.76±0.43	30.53±0.55
C	6.57±0.32	13.76±0.44	-	5.60±0.23
O	2.13±0.18	2.57±0.19	71.82±0.62	57.93±0.61
Fe	-	-	3.09±0.13	2.53±0.12
P	-	-	4.32±0.11	3.42±0.11
Si	-	0.59±0.09	-	-

In comparison with the blank cathode, the oxygen content locally exceeds 70% and almost reaches 60% for the entire area. This oxygen content is the highest observed for any of the cathode spots that were investigated. Combined with the green colour, which is typical for nickel oxides, and the lack of other significant metal concentrations, this indicates the formation of a thick nickel oxide layer. The presence of phosphorus without the presence of sodium in similar concentration might also indicate the formation of metal phosphates. However, due to the limitations of the EDX analysis method in analysing the chemical state, these hypotheses should be treated with caution.

Lastly, the brown precipitate forming on some of the cathodes was investigated. These locations are subsequently referred to as 'brown precipitate (cathode)'. Based on the colour of the precipitate, they were hypothesised to be made of metal phosphates. Figure 3.14 introduces the SEM results of the location 'brown precipitate', with the accompanying EDX data listed under table 3.10. The exact cathode locations are provided under figure D.8 in the appendix.

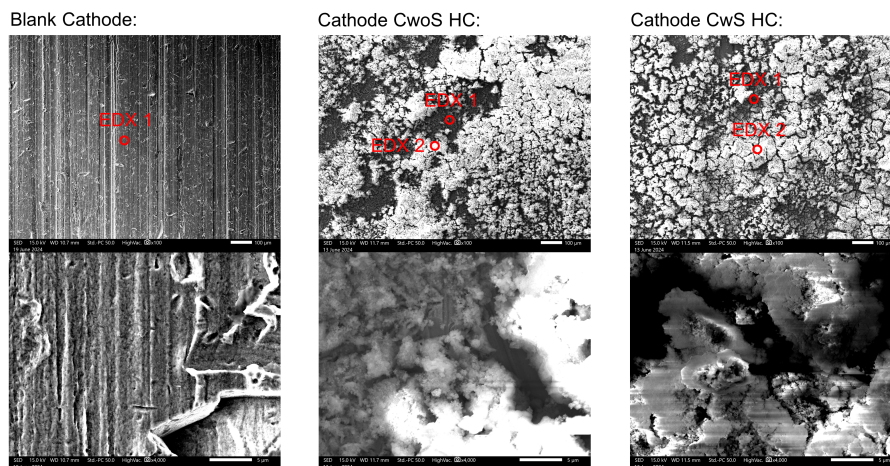


Figure 3.14: SEM results of the cathode location 'brown precipitate (cathode)'

These investigated cathode locations show a markedly changed surface morphology. Compared to the initially relatively smooth nickel surface, the surface after testing is covered by a fissured top layer

of alternating bright and dark spots. The SEM surface pictures at highest magnification also display locally flat and smooth surfaces areas.

Table 3.10: EDX results of the cathode location 'brown precipitate (cathode)'

Element [in Atom%]:	EDX Spot:							
	Cathode - EDX 1	Cathode - Area	CwoS HC - EDX 1	CwoS HC - EDX 2	CwoS HC - Area	CwS HC - EDX 1	CwS HC - EDX 2	CwS HC - Area
Ni	91.30±1.21	83.07±1.12	8.92±0.32	10.66±0.39	12.76±0.41	11.13±0.35	7.58±0.31	15.38±0.47
C	6.57±0.32	13.76±0.44	-	-	4.88±0.24	-	-	-
O	2.13±0.18	2.57±0.19	67.33±0.67	64.60±0.72	58.77±0.70	67.63±0.68	68.35±0.71	62.35±0.74
Fe	-	-	12.02±0.29	18.21±0.40	15.80±0.36	10.31±0.27	11.41±0.30	12.30±0.33
Cr	-	-	0.44±0.05	-	0.84±0.08	0.68±0.07	0.71±0.07	1.13±0.09
P	-	-	9.06±0.17	6.52±0.17	5.89±0.15	8.55±0.17	9.25±0.18	7.19±0.18
Na	-	-	2.23±0.14	-	1.06±0.12	1.70±0.13	2.22±0.15	1.35±0.14
Si	-	0.59±0.09	-	-	-	-	-	-
Ca	-	-	-	-	-	-	0.48±0.05	0.30±0.05

No clear explanation was found for the difference between darker and lighter regions based on the EDX data shown in table 3.10. While the lighter spots are marked by comparably high nickel and iron concentrations for one cathode, the lighter region of the other cathode is characterised by lower nickel but higher iron contents. Furthermore, both examined locations contain phosphorus. Previously, the phosphorus presence was attributed to the formation of sodium phosphate salts. However, for these locations the phosphorus concentrations exceeds the sodium concentration to such a degree, that salt formation cannot fully explain its presence. This circumstance, combined with the simultaneous observation of high contents of oxygen, iron, and phosphorus, suggest the formation of water insoluble nickel-and iron phosphate on the cathode surface. These findings were also supported by an additional XPS analysis of the same spots in subsection 3.4.5.

3.4.3. Nafion Membrane

Next, figure 3.15 displays the Nafion membranes of all four tests and compares them to the pristine Nafion membrane.

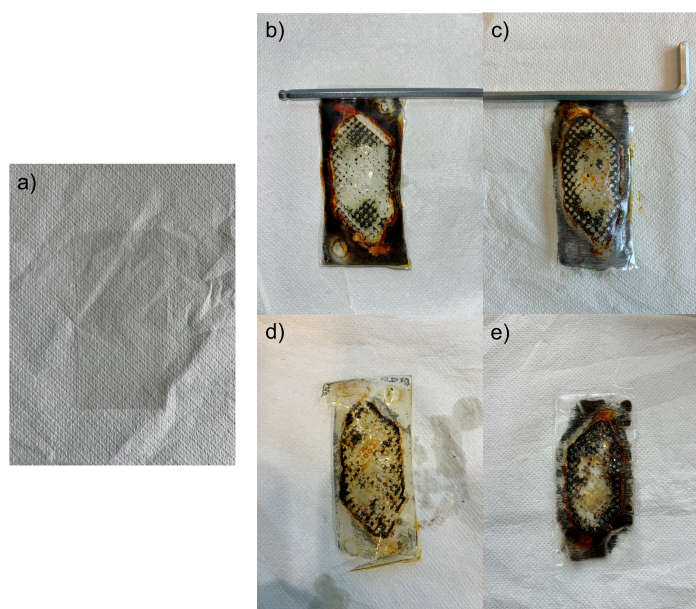


Figure 3.15: Pristine Nafion membrane shown in a); Nafion membranes after testing: b) Cell without seawater at 25 mA/cm²; c) Cell with seawater at 25 mA/cm²; d) Cell without seawater at 62.39 mA/cm²; e) Cell with seawater at 62.39 mA/cm²

As can be seen in figure 3.15, almost all Nafion membranes show extensive discoloration outside the flow field area after testing. Only the test at high current density without seawater shown in part (c)

of figure 3.15 does not exhibit this discoloration. On all membranes, black to greenish precipitate that has formed on the cathode around the perforations is clearly discernible. While the total amount of precipitate on the membranes varies between the different tests, no conclusions can be drawn from this observation, as different amounts of precipitate remain on the Nafion membrane during removal from the cathode. Generally, all membranes exhibit a slight yellowish tint after testing, compared to the initially clear membrane.

To check the Nafion membranes for surface morphology changes, for examples due to the formation of cracks, all Nafion membranes were cleaned and investigated using SEM. Figure 3.16 presents the results of these SEM investigations. No high magnification SEM pictures were taken due to the high static loading of the membrane during testing. All membranes were investigated on the cathode side, as this side showed the highest degree of precipitation formation for all tests.

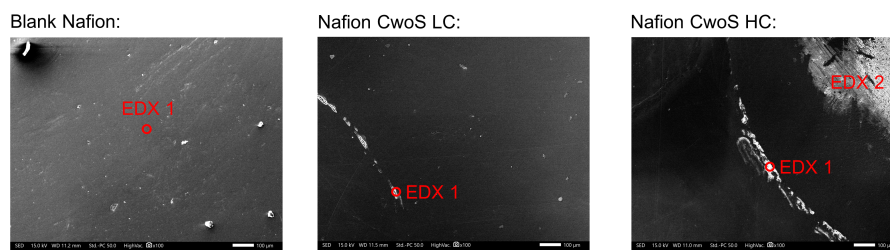


Figure 3.16: SEM results of the investigated Nafion membranes

As evident from figure 3.16, the Nafion membrane initially exhibits a relatively smooth and homogeneous surface. At some spots, the surface is blocked by impurities. In comparison, the test without seawater at low current density shows evidence of small fissures after testing. Apart from these fissures, however, the surface is still quite homogeneous and only sporadically blocked by impurities. A fundamentally different picture emerges when looking at the test without seawater at high current density. Here, large parts of the surface are blocked by precipitates.

Next, the spots marked in figure 3.16 were investigated using EDX. The results of this EDX analysis are given in table 3.11.

Table 3.11: EDX results of investigated Nafion membranes

	EDX Spot:						
	Nafion - EDX 1	Nafion - Area	CwoS LC - EDX 1	CwoS LC - Area	CwoS HC - EDX 1	CwoS HC - EDX 2	CwoS HC - Area
Element [in Atom%]:							
F	83.23±3.86	60.33±0.45	48.28±1.90	59.71±0.45	47.76±0.51	44.67±0.56	43.96±0.46
O	10.87±1.51	10.05±0.21	7.48±0.97	8.88±0.21	18.64±0.34	22.22±0.40	23.58±0.33
C	6.57±0.32	27.92±0.33	39.15±2.03	27.89±0.34	11.91±0.34	10.69±0.34	23.23±0.34
S	5.90±0.77	1.71±0.05	5.09±0.39	1.75±0.05	2.42±0.08	1.94±0.08	1.40±0.05
Na	-	-	-	1.77±0.08	5.36±0.17	6.91±0.22	2.89±0.10
Fe	-	-	-	-	5.21±0.17	6.89±0.22	1.39±0.08
P	-	-	-	-	6.70±0.13	5.02±0.12	2.78±0.07
Ni	-	-	-	-	2.01±0.14	1.66±0.14	0.41±0.06
Cr	-	-	-	-	-	-	0.37±0.04

Initially, an EDX analysis of the pristine membrane shows large amounts of fluorine, followed by smaller concentrations of carbon, oxygen, and finally sulfur. Given that Nafion consists of sulfonated tetrafluoroethylene, this initial composition was expected. The fact that only these four elements are measured also confirms the high initial purity of the Nafion membrane. After testing without seawater and at low current density, another element is measured: sodium. As previously hypothesised, sodium was expected to have migrated from anolyte to catholyte through the Nafion during operation. During this migration, sodium has been known to replace the protons of the sulfonate groups, which are responsible for the high proton conductivity of Nafion. Thus, the measurement of sodium after testing confirms

this hypothesis. Unfortunately, the EDX method is incapable of measuring hydrogen concentrations, such that no direct comment on the degree of proton replacement can be made.

Finally, the precipitate observed for the test without seawater at maximum current density is marked by the occurrence of iron, phosphorus, sodium, and, to a lower degree, nickel. The simultaneous appearance of sodium and phosphorus indicates the formation of salts. Furthermore, an EDX area scan shows higher concentrations of phosphorus than sodium. Thus, metal phosphates are assumed to have formed. Lastly, the rise in oxygen concentration compared to the pristine Nafion membrane indicates the formation of metal oxides, metal hydroxides, or metal oxide hydroxides. In summary, the precipitate is attributed to a mixture of compounds already analysed on the cathodes. This was expected, as the Nafion membranes were directly attached to the cathodes during testing.

3.4.4. FO Membrane

Furthermore, the FO membranes used in the two tests with in-situ seawater purification were investigated. First, figure 3.17 shows the two used membranes and compares them to the initial FO membrane.

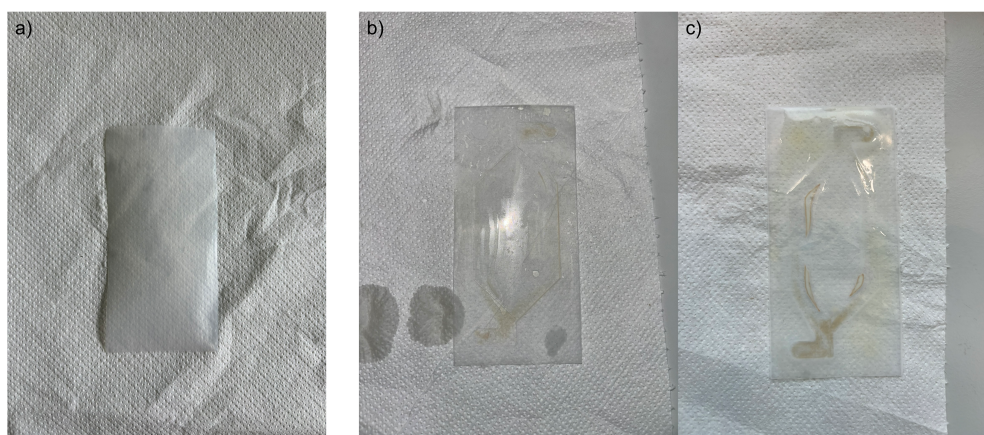


Figure 3.17: Blank FO membrane shown in a); FO membranes after testing: b) Cell with seawater at 25 mA/cm²; c) Cell with seawater at 62.39 mA/cm²

As can be seen from figure 3.17, both membranes exhibit discoloration after testing. As such, the FO membranes show spots with a yellowish-brownish tinge, compared to the clear colour of the pristine membrane. This tinge is attributed to the anolyte of similar colour that flows along the membrane during testing. Furthermore, the imprints of the flow field directly attached to the FO membrane during testing are clearly visible. Nonetheless, no evidence for membrane perforations was found for either membrane. Finally, the FO membrane of the test at maximum current density exhibits some elongated shapes with a dark brown edge and yellowish colouring on the inside. These shapes are all located inside the flow field, at some distance from the flow field edge. Based on the EDX results of this FO membrane introduced later, the dark brown discoloration of these shapes was found to be due to the deposition of iron phosphate.

Next, the FO membranes were investigated using SEM and EDX. Same as for the Nafion membranes, no SEM pictures were taken at high magnification due to the extremely low conductivity of the membrane and its general fragility. The surface morphology of the membrane could not have been accurately characterised using SEM in any case, however, as the membrane needed to be dried out before testing. This drying-out process caused the membrane to shrink and warp considerably. Nonetheless, some low-resolution images were taken of the elongated membrane shapes of the maximum current density shown in figure 3.17, using the backscatter electron detector. This detector visualises density differences in the sample surface, with denser regions appearing brighter. Furthermore, an EDX measurement of the investigated location was taken. The SEM and EDX results of the investigated sample are shown in figure 3.18.

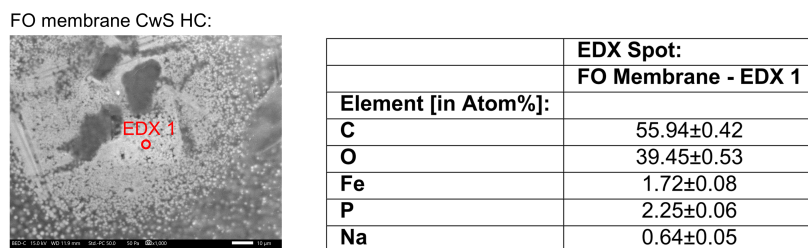


Figure 3.18: SEM and EDX results of the investigated FO membrane

As is evident from figure 3.18, the FO membrane exhibits a density increase at the elongated shapes. This density increase can be identified by the brightness of the white dots that have formed on the membrane surface, compared to the darker membrane background. By investigating one of the bright white spots using EDX, the results of the table shown in figure 3.18 were attained. Based on these EDX results, carbon and oxygen are the by far most common elements at the FO membrane surface. Since the FO membrane is made out of triacetate cellulose, this result was expected. However, the investigated location also exhibits smaller concentrations of sodium, phosphorus, and iron. Assuming that the comparably low sodium concentration is due to the formation of salt crystals with phosphorus, these results suggest the formation of iron phosphate on the FO membrane surface.

3.4.5. XPS

Finally, XPS was used on some of the anode and cathode locations introduced before. Using XPS had the distinct advantage of being able to directly identify some of the chemical compounds that had formed on the electrode surfaces. Furthermore, as opposed to EDX, XPS offered an opportunity to only investigate the composition of the immediate top layer of the samples. Therefore, XPS provided a good way to confirm some of the hypotheses formed during the analysis of the electrochemical results.

Generally, XPS was used for two types of analyses: identifying chemical compounds, and measuring atomic percentages. It is important to note that for chemical state analysis, the XPS curves were aligned on the y-axis to allow for a better comparison of peak shifts. Thus, the corresponding figures do not indicate the measured elemental concentrations.

For the anode, only the location 'no corrosion' was investigated. Figure 3.19 shows the XPS results for iron, chromium, and nickel for the blank anode and the anode of the test with seawater at maximum current density.

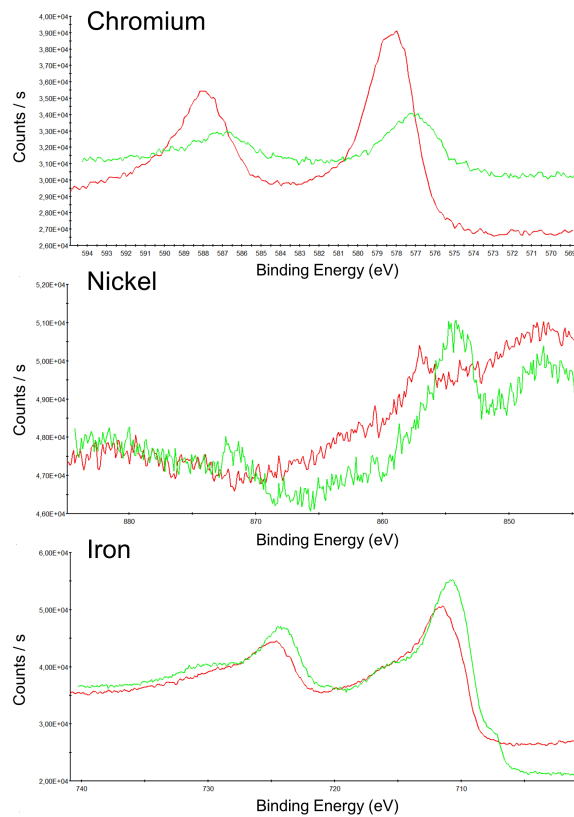


Figure 3.19: Selected XPS data from the blank anode (green) and CwS HC (red)

As can be seen from the figure, the profiles of all three elements show a vertical offset before and after testing. Generally, the area underneath the peak or peaks of each element profile correlate with the concentration of that element on the sample surface. Hence, after testing, the nickel and iron concentrations of the anode surface have decreased. This is evident by the comparably smaller peaks of either element. Simultaneously, a significantly stronger chromium signal is detected, representing a shift towards higher chromium concentrations. Generally, this finding is unsurprising. As is evident from the 316L SS surface profile graph shown in figure E.1 in the appendix, stainless steel tends to have comparably higher concentrations of both iron and nickel at the surface, and a growing chromium concentration deeper inside the layer.

On the cathodes, two locations were analysed via XPS: 'black' and 'brownish deposition (cathode)'. Figure 3.20 displays the results of the location 'brownish deposition (cathode)'. Based on the EDX results, this location had been identified as consisting of nickel- and iron phosphate compounds. Furthermore, the formation of these compounds played a central role in the explanation of the observed stable cathode overpotentials. Thus, the XPS results were expected to confirm these results and strengthen the hypothesis.

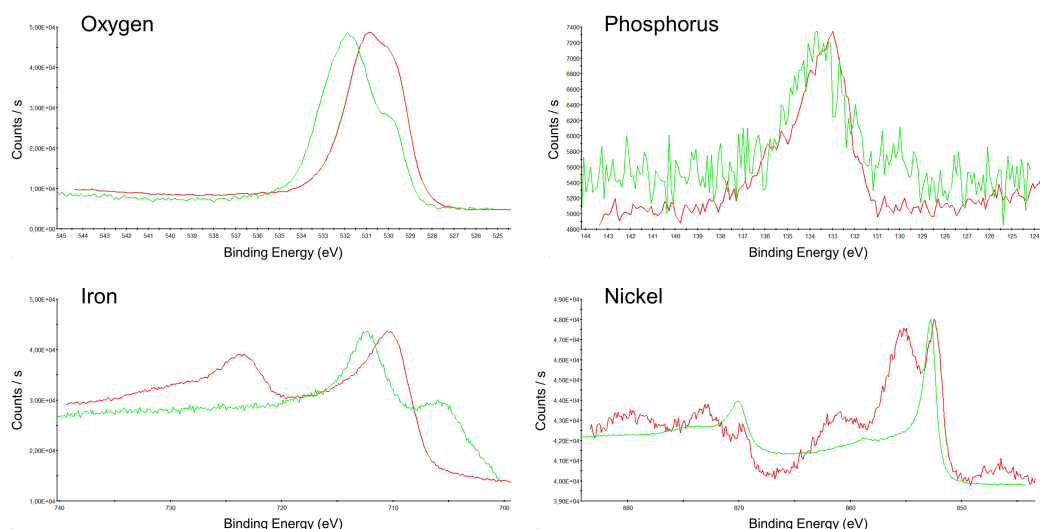


Figure 3.20: Selected XPS data from the blank cathode (green) and CwS LC (red)

As is evident from figure 3.20, the oxygen profile originally exhibits a peak at 531.97 eV with a small adjacent satellite peak. After testing, the oxygen peak has shifted towards lower energies and now lies at roughly 530.58 eV. This value is consistent with the reported oxygen peak values observed in phosphate anions [62]. Next, the singular peak of the phosphorus profile exhibits a shift from 133.63 eV to 133.21 eV. As the metal phosphate peak lies at 133 eV, this is a clear sign for the formation of metal phosphates [63]. Additionally, the iron profile shows the formation of a second peak at higher energies compared to the original profile. The original peak is still present, but shifts to lower energies. Both peaks after testing are consistent with the results commonly found for materials with iron in an oxidation state of +3, such as iron phosphate [64]. Finally, the nickel profile shows massive changes during testing. Initially, a relatively simple profile can be discerned, with peaks at energies that are characteristic for nickel metal. In comparison, after testing both main peaks have turned into multiplet-splits, with clearly discernible satellite peaks at higher energies. The new peaks and their satellites are commonly related to nickel cations in the oxidation states +2 and +3 [65]. This observation is consistent with the occurrence of nickel phosphate, where nickel is present in an oxidation state of +2.

Therefore, the XPS data of all relevant elements showed clear signs of the formation of nickel and iron phosphate compounds at the investigated location. Hence, the previous findings of the EDX analysis were confirmed.

Finally, the location 'black' was investigated on the backside of the cathode of the test with seawater at maximum current density. This black layer had formed on the cathodes of all tests after operation. Based on the EDX results, the layer had been initially identified as a mixture of nickel- and iron oxides. The occurrence of these compounds were a key component in explaining the observed stable cathode overpotentials, as both are good HER catalysts. Figure 3.21 shows the XPS results of this location.

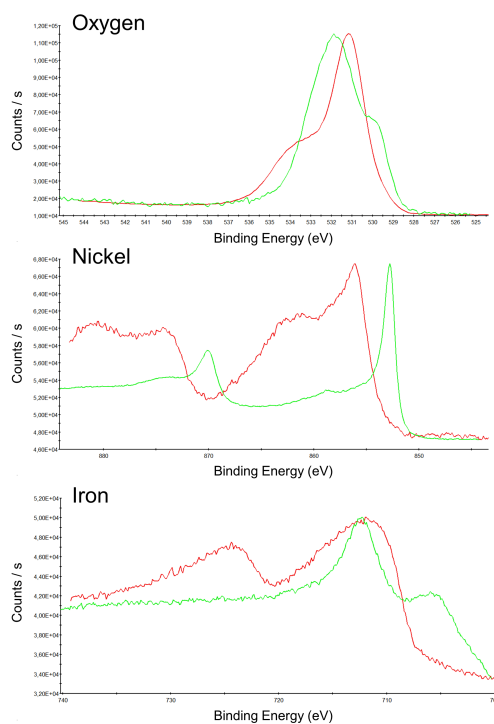


Figure 3.21: Selected XPS data from the blank cathode (green) and CwS HC (red)

As shown in figure 3.21, the oxygen peak after testing has shifted to lower energies, from an initial 531.97 eV to roughly 531.24 eV. Generally, the oxygen peak for metal oxides commonly appears at between 529-530 eV [66]. Thus, while the shift to lower energies indicates the formation of metal oxides, the peak is still at a relatively high energy. However, the peak fits well to the values commonly observed for iron oxide hydroxide (530.9 eV), or nickel- and iron hydroxide (both at 531.3 eV) [62]. Notably, a small satellite peak appears at an energy of around 533.82 eV after testing. This satellite peak was not present in the pristine nickel cathode. A peak at this location is also associated with the formation of metal hydroxides [67].

The nickel profile again exhibits massive changes after testing. Both original peaks have shifted to the left to higher energies and both contain adjacent satellite peaks. As such, the profile resembles the one measured for the 'brownish deposition (cathode)' location and thus indicates the existence of nickel in oxidation states of +2 and +3. Crucially, however, the low-energy multiplet-split has disappeared, with the sole peak having shifted so slightly higher energies. This observation is typical for the formation of both nickel hydroxide and nickel oxide hydroxide [68].

Lastly, with regard to the iron profile, the occurrence of a second peak can be observed after testing. After testing, the lower peak has shifted slightly from 712.29 eV for the blank nickel to 711.85 eV for the used cathode. Thus, the locations of the peaks agree relatively well between the two samples. However, the energies of both peaks are also significantly above the peak energy 706.7 eV commonly observed for metal iron [69]. The observed peak locations at higher energies thus indicate the occurrence of either iron oxide or iron oxide hydroxide for both samples [70]. Furthermore, the pristine nickel cathode exhibits another small peak at lower energy, close to the energy level observed in iron metal. This peak has completely disappeared after testing, suggesting a lack of pure iron metal. Lastly, the secondary peak found after testing is located at 724.34 eV. As previously mentioned, a secondary peak at this energy is commonly associated with the occurrence of iron cations in an oxidation state of +3, such as in iron(III) oxide or iron oxide hydroxide.

Therefore, the XPS data does not confirm the initial assumption of metal oxide formation. Instead, evidence was found for the formation of both iron- and nickel hydroxide, as well as iron- and nickel oxide hydroxide at the investigated location.

3.5. Combined Results Analysis

When combining all results found during the water mass flux and electrochemical tests, as well as the solution, membrane, and electrode analyses, a self-reinforcing degradation cycle can be identified that drives the corrosion processes observed in all tests. This degradation cycle is shown in figure 3.22.

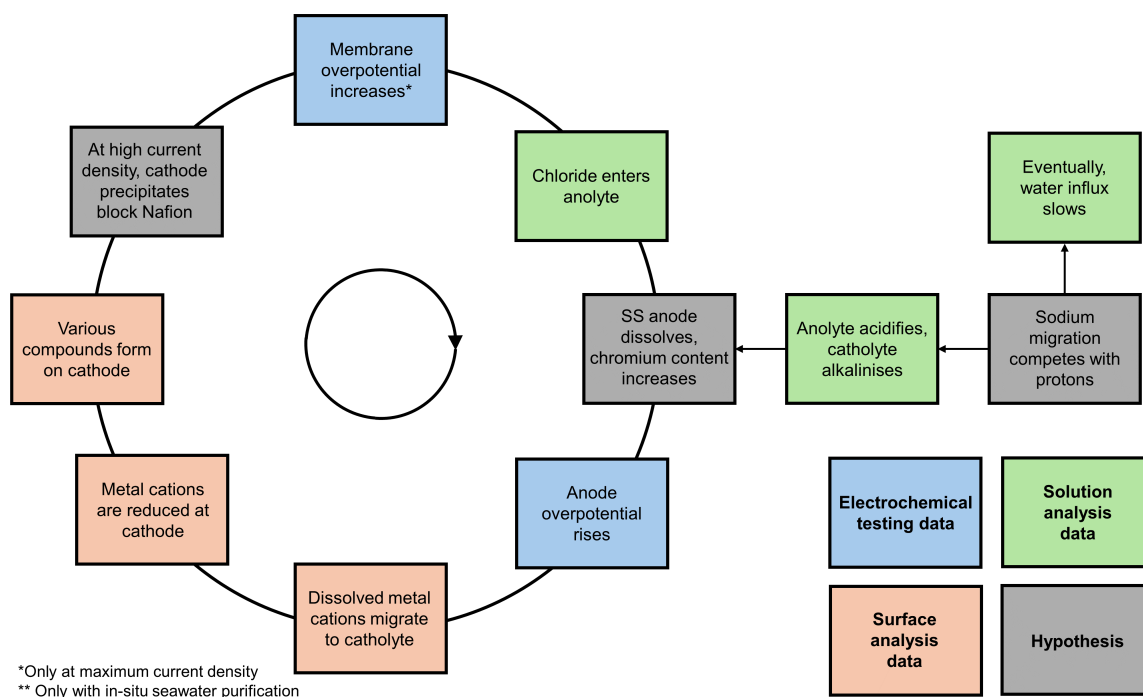


Figure 3.22: The degradation cycle governing the corrosion processes

Looking at figure 3.22, the sodium versus proton migration competition across the Nafion membrane is identified as the key process that kicks off the degradation cycle. Due to the sodium migration, not all protons formed in the anolyte are able to migrate to the catholyte side. Thus, the anolyte slowly starts to acidify (see table 3.1). This acidification process enables the breakdown of the protective passivation layer on top of the stainless steel anode. Consequently, the nickel- and iron-rich surface layer of the stainless steel is dissolved and replaced by a chromium-rich surface layer, as shown by the XPS anode results of subsection 3.4.5. Due to the poorer catalytic properties of the chromium-rich surface, the anode overpotential starts rising. The metal ions, specifically nickel and iron cations, that dissolve into the anolyte migrate through the Nafion and deposit on the cathode. Based on the EDX and XPS results, these cations form a variety of compounds, such as iron- and nickel phosphate, iron- and nickel-hydroxide, and iron oxide hydroxide. Some of these compounds increase the catalytic properties of the cathode for the HER, and thereby stabilise the cathode overpotential (not shown in figure 3.22). However, at maximum current density, the deposits also start blocking some of the Nafion membrane area, leading to increased membrane overpotentials. The substitution of protons on the sulfonic groups by sodium cations is hypothesised to also contribute to the membrane overpotential rise (also not shown in figure 3.22). Next, for those tests with in-situ seawater purification, chloride slowly leeches into the system through the FO membrane and causes additional SS degradation. In consequence, the anode overpotential and keeps rising. This increases the central driving force behind the metal dissolution and thereby reinforces the cycle. Finally, the cycle starts anew.

Crucially, the sodium migration from anolyte to catholyte also decreases the osmotic pressure of the anolyte, despite increasing metal dissolution and water consumption via water oxidation. This is evident from the stable seawater weight measurements for the test at low current density seen in table 3.3.3. Hence, the water mass flux across the FO membrane slows. Eventually, the process stabilises as the anolyte continues losing water and thus experiences an increase in osmotic pressure. However, this stabilisation occurs at a markedly different anolyte composition compared to the initial solution.

4

Conclusion

The massive amounts of hydrogen needed for a successful energy transition are bound to put additional strain on already scarce global freshwater sources. One approach to eliminate the dependence of water electrolysis on freshwater is through the use of seawater as a process feed. However, innovative and efficient cell designs and purification methods are needed to enable the use of seawater. One such approach is to utilise in-situ seawater purification via FO membranes. While the general concept has been proved viable, previous research on this topic has only been performed at low current densities, while simultaneously demonstrating high cell overpotentials. Therefore, the goal of this research was to quantify the attainable current density of the FO-based purification method, and to optimise the cell performance through use of a zero-gap design. Furthermore, this research aimed to quantify the material and performance degradation exhibited by such a zero-gap design.

To this end, the water migration across an FO membrane in the given system was measured. From this measurement, the achievable maximum current density was attained. Next, long-term electrochemical tests were performed on an electrochemical cell, both with and without water purification, and at different current densities. Afterwards, the voltage measurements before and after these long-term tests were broken down into their individual contributions. Finally, all cell parts and solutions were investigated on their degradation utilising a range of analyses methods.

A summary of the results of this research leads to a number of conclusions. First, based on the measured water mass flux across the chosen FO membrane and solutions, the chosen FO-based cell design can at best reach a current density of 62.39 mA/cm^2 . While an improvement on the previous state-of-the-art cell design, this value is still an order of magnitude off from the current densities observed in industrial scale water electrolysis systems. Thus, to attain competitive current densities, fundamental changes have to be made to the cell design.

Next, the system initially exhibited lower overpotentials for both OER and HER compared to the previous state-of-the-art FO water electrolysis cell at equal current densities of 25 mA/cm^2 . These improvements were attributed to improved flow conditions, decreasing bubble and concentration overpotentials. Additionally, the new design allowed for an effective separation of the oxygen and hydrogen products through use of a Nafion membrane, a crucial capability that the previous system lacked.

However, all tested cells also showed strong signs of performance and material degradation. The performance degradation was traced back to two developments. First, the dissolution of a catalytically active iron- and nickel-rich SS anode surface, and its replacement by a chromium-rich layer. This dissolution, in turn, was traced back to gradual acidification of the cell anolyte, causing a breakdown of the SS passivation layer. For the tests with in-situ water purification, this breakdown process was also reinforced by the presence of chloride in the anolyte. Second, a mixture of conductivity-detrimental membrane effects such as sodium-proton substitution and membrane blockage. The second effect was only observed for tests at the maximum current density.

In contrast, the performance degradation was attenuated by the formation of superior HER-catalysts on

the cathode surface, leading to stable, and even improving, cathode overpotentials. These compounds were identified as nickel hydroxide, nickel phosphate, and iron phosphate. Similarly, the FO membrane was found to still function as intended after testing, despite encountering working conditions outside its specifications, and even showed an increase in measured water flux. This demonstrates the general resilience of FO membranes based on cellulose triacetate.

Overall, the cell design proved an improvement on the previous state-of-the-art cell with regard to system performance and product separation. However, severe system degradation appeared after only 40 hours of testing, which would eventually cause the cell to stop operating properly. Therefore, a number of cell and system changes have to be made to improve the process. Consequently, the next chapter provides a list of recommendations both with regard to proposed future research focuses, as well as cell and system improvements.

5

Recommendations

5.1. Hypotheses Validation

A variety of hypotheses were put forward during the analysis of the testing results. This subsection presents some testing methods that could be used in future research to confirm or disprove these hypotheses.

Electrode Overpotential Changes

First, it was hypothesised that the observed increase in anode overpotential was due to the dissolution of a thin and catalytically active nickel- and iron-rich layer on the SS anode surface. However, no direct connection was made between the assumed change in catalytic properties and the observed overpotential. Similarly, the comparably stable, or even improving, cathode overpotentials were attributed to the formation of catalytically superior compounds on the nickel cathode surface. However, this hypothesis also lacks a direct link to the observed overpotential change.

Such a direct link between the metal dissolution and metal phosphate formation, and changes in the observed overpotentials, could be established by performing Tafel analysis on the electrodes. This Tafel analysis would enable a direct quantification of the change in catalytic properties of the electrodes. Even better, these tests could be performed immediately after long-term tests on the fully assembled cell, and thus prevent the aforementioned risk of electrode surface changes that accompany cell disassembly.

Membrane Overpotential Changes

Another set of hypotheses concerned changes in membrane overpotential. First, the membrane conductivity could be tested separately after testing, to ensure that it is indeed the change in conductivity that causes the measured overpotential change. This could also be done by replacing only the membrane after long-term testing, and repeating cell voltage and electrode potential measurements. One of these test should be done in any case, as the membrane overpotential was not a directly measured value, but instead constructed from the measured cell voltages and potentials. Additionally, the hypothesis that improvements in Nafion protonation cause the observed overpotential decrease could be tested by placing the Nafion in an acid bath, and comparing its conductivity with that of a regularly pre-treated Nafion membrane.

Chromic Acid Formation

Lastly, a hypothesis was formed that the observed anolyte colour change for some tests was due to the formation of chromic acid. This hypothesis should be confirmed by investigating the anolyte composition via detailed solution analysis methods such as stripping voltammetry or atomic absorption spectroscopy. Confirming the hypothesis and identifying the concentration of chromic acid is of crucial importance for operating safety of the system, as chromic acid is a toxic and carcinogenic substance.

5.2. Cell and System Design

Based on the observed system degradation, a variety of cell and system design, as well as operational changes are recommended. All of these changes are introduced and described in this subsection.

Anolyte Acidification

The gradual acidification of the anolytes was identified as the main cause for the observed metal dissolution. Generally, the pH swings of both anolyte and catholyte can both be traced back to the use of a cation-exchange membrane in the cell. This cation-exchange membrane prevents the hydroxide ions that form in the catholyte from migrating to the anolyte, and thus from stabilising the pH of both solutions. Based on this finding, two potential solutions are proposed.

The first solution consists of mixing the anolyte and catholyte solutions before feeding them back into the cell. Mixing the two solutions would lead to an overall neutralisation, thus avoiding the problematic pH swings. However, a variety of things have to be considered before pursuing this solution. First, anolyte and catholyte solutions were originally separated in this research to avoid safety risks connected to the mixing of dissolved gaseous hydrogen and oxygen. Thus, the setup design would have to be expanded by adding phase separators, which ensure that only trace amounts of dissolved oxygen and hydrogen are left before mixing. This, however, would significantly increase the complexity of the system. Next, mixing anolyte and catholyte would also entail spreading the chloride influx previously limited to the anolyte also to the catholyte. Thus, corrosive processes caused by the presence of chloride would then no longer be limited to the anode.

As part of the second solution, the cation-exchange membrane could be replaced by a non-selective diaphragm. By using a non-selective diaphragm, hydroxide ions in the catholyte could migrate to the anolyte, again leading to a neutralisation of both solutions. Nonetheless, this solution also entails a number of challenges. First, as one of the crucial tasks of the membrane consists of preventing gas-crossover between anolyte and catholyte, a non-selective membrane with good gas blockage properties would have to be used. Additionally, switching to a non-selective diaphragm would likely also lead to an increase in the observed cell voltage due to their comparably low conductivities. Finally, the switch would again allow chloride to enter the catholyte, possibly worsening the observed corrosion at the cathode.

Cell Changes

Next to acidification, the observed cell degradation was assumed to also be strongly influenced by the relatively high applied electrode overpotentials. Thus, any steps that could be taken to decrease the applied potentials at either electrode should also lead to a significant decrease in system degradation. Therefore, it is recommended to replace the perforated metal plate electrodes by either metal mesh or metal foam electrodes. Mesh and foam electrodes contain a much larger active surface area at which the targeted reactions can take place. Thus, they should lead to a significant decrease in concentration overpotentials, as well as preventing the entrapment of large bubbles. Thereby, the electrode potentials, and correspondingly the driving force behind the corrosive processes, would be minimised. Originally, mesh and foam electrodes were considered for this research, but ultimately dropped due to the difficulty of bubble removal from them. However, this engineering challenge should ultimately be resolvable, for example by designing a flow-through cell rather than a flow-by design.

Next, switching from the current-zero gap design to a so-called near-zero gap design with a small gap between membrane and electrode is proposed. Previous research has shown near-zero gap cells to exhibit lower overpotentials, which is usually attributed the previously described blanketing effect in zero-gap cells. Furthermore, introducing a small gap between membrane and electrode should prevent the formation of locally stagnant flow zones which are assumed to enhance metal dissolution.

Setup Changes

Moreover, with regard to simultaneous measurements, it is advised that hardware changes are made to enable the real-time measurement of all four voltages inside the cell in future research. Such a continuous and simultaneous measurement would greatly improve insight into the cell behaviour, and allow for an accurate analysis and explanation of what causes the observed cell voltage fluctuations and trends.

Generally, adding phase separators to the anolyte and catholyte outlets would also allow for the evaluation of the product gas streams in a gas chromatograph. Thereby, the influence of side-reactions such as chloride oxidation and metal cation reduction on the OER and HER Faradaic efficiencies, respectively, could be quantified. Previously, the findings of this research assumed a 100% Faradaic efficiency for either reaction. However, in light of the extensive observed corrosion reactions, which are in essence redox reactions competing with the OER and HER, this assumption is easily challenged. Thus, measuring the impact of parasitic reactions would be valuable for in-depth system performance analysis.

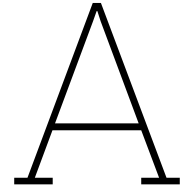
References

- [1] Hoesung Lee et al. "CLIMATE CHANGE 2023 synthesis report summary for policymakers". In: *CLIMATE CHANGE 2023 Synthesis Report: Summary for Policymakers* (2024).
- [2] Pami Aalto et al. "Introduction: electrification and the energy transition". In: *Electrification*. Elsevier, 2021, pp. 3–24.
- [3] Alexandra M Oliveira, Rebecca R Beswick, and Yushan Yan. "A green hydrogen economy for a renewable energy society". In: *Current Opinion in Chemical Engineering* 33 (2021), p. 100701.
- [4] Rebecca R Beswick, Alexandra M Oliveira, and Yushan Yan. "Does the green hydrogen economy have a water problem?" In: *ACS Energy Letters* 6.9 (2021), pp. 3167–3169.
- [5] Samuel S Veroneau et al. "Direct seawater splitting by forward osmosis coupled to water electrolysis". In: *ACS Applied Energy Materials* 5.2 (2022), pp. 1403–1408.
- [6] Ibrahim Dincer. *Comprehensive energy systems*. Elsevier, 2018.
- [7] Marian Chatenet et al. "Water electrolysis: from textbook knowledge to the latest scientific strategies and industrial developments". In: *Chemical Society Reviews* 51.11 (2022), pp. 4583–4762.
- [8] Josue M Goncalves et al. "Nanoporous gold-based materials for electrochemical energy storage and conversion". In: *Energy Technology* 9.5 (2021), p. 2000927.
- [9] Julie C Fornaciari et al. "Mechanistic Understanding of pH Effects on the Oxygen Evolution Reaction". In: *Electrochimica Acta* 405 (2022), p. 139810.
- [10] Takahiro Naito et al. "Water Electrolysis in Saturated Phosphate Buffer at Neutral pH". In: *ChemSusChem* 13.22 (2020), pp. 5921–5933.
- [11] Alfredo Ursua, Luis M Gandia, and Pablo Sanchis. "Hydrogen production from water electrolysis: current status and future trends". In: *Proceedings of the IEEE* 100.2 (2011), pp. 410–426.
- [12] Dmitri Bessarabov and Pierre Millet. *PEM water electrolysis*. Vol. 1. Academic Press, 2018.
- [13] Marcelo Carmo et al. "A comprehensive review on PEM water electrolysis". In: *International journal of hydrogen energy* 38.12 (2013), pp. 4901–4934.
- [14] IEA. *Global Installed Electrolysis Capacity by Technology, 2015-2020*. 2021. URL: <https://www.iea.org/data-and-statistics/charts/global-installed-electrolysis-capacity-by-technology-2015-2020>. (accessed: 24.05.2024).
- [15] Frano Barbir. "PEM electrolysis for production of hydrogen from renewable energy sources". In: *Solar energy* 78.5 (2005), pp. 661–669.
- [16] Katherine E Ayers et al. "Research advances towards low cost, high efficiency PEM electrolysis". In: *ECS transactions* 33.1 (2010), p. 3.
- [17] Keisuke Obata et al. "In situ observation of pH change during water splitting in neutral pH conditions: impact of natural convection driven by buoyancy effects". In: *Energy & Environmental Science* 13.12 (2020), pp. 5104–5116.
- [18] Shao-Wen Xu et al. "Recent advances in direct seawater splitting for producing hydrogen." In: *Chemical Communications (Cambridge, England)* (2023).
- [19] Thomas P Keane and Daniel G Nocera. "Selective production of oxygen from seawater by oxidic metallate catalysts". In: *ACS omega* 4.7 (2019), pp. 12860–12864.
- [20] Frank J Millero et al. "The composition of Standard Seawater and the definition of the Reference-Composition Salinity Scale". In: *Deep Sea Research Part I: Oceanographic Research Papers* 55.1 (2008), pp. 50–72.
- [21] Fabio Dionigi et al. "Design criteria, operating conditions, and nickel–iron hydroxide catalyst materials for selective seawater electrolysis". In: *ChemSusChem* 9.9 (2016), pp. 962–972.

- [22] Yun Kuang et al. "Solar-driven, highly sustained splitting of seawater into hydrogen and oxygen fuels". In: *Proceedings of the National Academy of Sciences* 116.14 (2019), pp. 6624–6629.
- [23] Carl W White and James G Martin. "Chlorine gas inhalation: human clinical evidence of toxicity and experience in animal models". In: *Proceedings of the American Thoracic Society* 7.4 (2010), pp. 257–263.
- [24] Norio Sato. "Basics of corrosion chemistry". In: *Green Corrosion Chemistry and Engineering* 1 (2012).
- [25] Heping Xie et al. "A membrane-based seawater electrolyser for hydrogen generation". In: *Nature* 612.7941 (2022), pp. 673–678.
- [26] Sudesh Kumari et al. "Solar hydrogen production from seawater vapor electrolysis". In: *Energy & Environmental Science* 9.5 (2016), pp. 1725–1733.
- [27] Joshua M Spurgeon and Nathan S Lewis. "Proton exchange membrane electrolysis sustained by water vapor". In: *Energy & Environmental Science* 4.8 (2011), pp. 2993–2998.
- [28] R Pärnamäe et al. "Bipolar membranes: A review on principles, latest developments, and applications". In: *Journal of Membrane Science* 617 (2021), p. 118538.
- [29] Daniela H Marin et al. "Hydrogen production with seawater-resilient bipolar membrane electrolyzers". In: *Joule* 7.4 (2023), pp. 765–781.
- [30] Muhammad Qasim et al. "Water desalination by forward (direct) osmosis phenomenon: A comprehensive review". In: *Desalination* 374 (2015), pp. 47–69.
- [31] Donald A. McQuarrie, Peter A. Rock, and Ethan B. Gallogly. *General Chemistry*. Fourth. University Science Books Mill Valley, 2011.
- [32] Qingchun Ge, Mingming Ling, and Tai-Shung Chung. "Draw solutions for forward osmosis processes: Developments, challenges, and prospects for the future". In: *Journal of membrane science* 442 (2013), pp. 225–237.
- [33] Tzahi Y Cath, Amy E Childress, and Menachem Elimelech. "Forward osmosis: Principles, applications, and recent developments". In: *Journal of membrane science* 281.1-2 (2006), pp. 70–87.
- [34] ElectroCell. *Micro Flow Cell*. URL: <https://www.electrocell.com/products/electrochemical-flow-cells/micro-flow-cell>. (accessed: 11.06.2024).
- [35] Sterlitech. *FTSH2O Flat Sheet Membrane*. 2024. URL: <https://www.sterlitech.com/ftsh2o-flat-sheet-membrane-cta-fo-305-x-305-mm-1-pk.html>. (accessed: 25.05.2024).
- [36] Asif Matin et al. "Biofouling in reverse osmosis membranes for seawater desalination: phenomena and prevention". In: *Desalination* 281 (2011), pp. 1–16.
- [37] Robert J. Beynon. *Calculator for pH Buffers*. 2023. URL: <http://phbuffers.org/BufferCalc/Buffer.html>. (accessed: 02.06.2024).
- [38] Gaskatel. *Mini Hydrogen Reference Electrode Mini-HydroFlex*. 2024. URL: <https://gaskatel.de/en/shop/mini-hydrogen-reference-electrode-mini-hydroflex/>. (accessed: 25.05.2024).
- [39] Gregory Jerkiewicz. "Standard and reversible hydrogen electrodes: Theory, design, operation, and applications". In: *ACS Catalysis* 10.15 (2020), pp. 8409–8417.
- [40] Anders B Laursen et al. "Electrochemical hydrogen evolution: Sabatier's principle and the volcano plot". In: *Journal of Chemical Education* 89.12 (2012), pp. 1595–1599.
- [41] Paola Quaino et al. "Volcano plots in hydrogen electrocatalysis—uses and abuses". In: *Beilstein journal of nanotechnology* 5.1 (2014), pp. 846–854.
- [42] Leigang Li et al. "Recent progress in advanced electrocatalyst design for acidic oxygen evolution reaction". In: *Advanced Materials* 33.50 (2021), p. 2004243.
- [43] MF Montemor et al. "Chemical composition and electronic structure of the oxide films formed on 316L stainless steel and nickel based alloys in high temperature aqueous environments". In: *Corrosion Science* 42.9 (2000), pp. 1635–1650.

- [44] Fernando Rocha et al. "Effect of pore size and electrolyte flow rate on the bubble removal efficiency of 3D pure Ni foam electrodes during alkaline water electrolysis". In: *Journal of Environmental Chemical Engineering* 10.3 (2022), p. 107648.
- [45] Juergen Fischer et al. "Fundamental investigations and electrochemical engineering aspects concerning an advanced concept for alkaline water electrolysis". In: *AIChE Journal* 26.5 (1980), pp. 794–802.
- [46] The Chemours Company. *Product Bulletin P-12: Nafion N115, N117, N1110*. 2016. URL: <https://fuelcellearth.com/pdf/nafion-N115-N117-N1110.pdf>. (accessed: 25.05.2024).
- [47] Shahbaz Ahmad et al. "An overview of proton exchange membranes for fuel cells: Materials and manufacturing". In: *International Journal of Hydrogen Energy* 47.44 (2022), pp. 19086–19131.
- [48] Samuel S Veroneau and Daniel G Nocera. "Continuous electrochemical water splitting from natural water sources via forward osmosis". In: *Proceedings of the National Academy of Sciences* 118.9 (2021), e2024855118.
- [49] Ray F Egerton et al. *Physical principles of electron microscopy*. Vol. 56. Springer, 2005.
- [50] Banshi D Gupta, Vivek Semwal, and Anisha Pathak. "Nanotechnology-based fiber-optic chemical and biosensors". In: *Nano-Optics: Fundamentals, Experimental Methods, and Applications* (2020), p. 163.
- [51] Jill Chastain and Roger C King Jr. "Handbook of X-ray photoelectron spectroscopy". In: *Perkin-Elmer Corporation* 40 (1992), p. 221.
- [52] Tery L Barr. *Modern ESCA principles and practice of X-ray photoelectron spectroscopy*. CRC press, 2020.
- [53] Cheng Zhong et al. "A review of electrolyte materials and compositions for electrochemical supercapacitors". In: *Chemical Society Reviews* 44.21 (2015), pp. 7484–7539.
- [54] JW Haverkort and H Rajaei. "Voltage losses in zero-gap alkaline water electrolysis". In: *Journal of Power Sources* 497 (2021), p. 229864.
- [55] Sengeni Anantharaj et al. "High-performance oxygen evolution anode from stainless steel via controlled surface oxidation and Cr removal". In: *ACS Sustainable Chemistry & Engineering* 5.11 (2017), pp. 10072–10083.
- [56] Liuxiang Huo et al. "Applications of nickel-based electrocatalysts for hydrogen evolution reaction". In: *Advanced Energy and Sustainability Research* 3.4 (2022), p. 2100189.
- [57] Jaun An et al. "Cobalt-Doped Iron Phosphate Crystal on Stainless Steel Mesh for Corrosion-Resistant Oxygen Evolution Catalyst". In: *Catalysts* 12.12 (2022), p. 1521.
- [58] Syed Muhammad Zain Mehdi et al. "Synthesis of nickel phosphate nanowires as a bifunctional catalyst for water electrolysis in alkaline media". In: *Journal of Alloys and Compounds* 988 (2024), p. 174250.
- [59] James C Bendert, Dionissios D Papadias, and Deborah J Myers. "The effect of Na⁺ impurities on the conductivity and water uptake of Nafion 115 polymer electrolyte fuel cell membranes". In: *Journal of The Electrochemical Society* 157.10 (2010), B1486.
- [60] Mohammad Bagher Karimi, Fereidoon Mohammadi, and Khadijeh Hooshyari. "Recent approaches to improve Nafion performance for fuel cell applications: A review". In: *International Journal of Hydrogen Energy* 44.54 (2019), pp. 28919–28938.
- [61] P Millet. "Chlor-alkali technology: fundamentals, processes and materials for diaphragms and membranes". In: *Handbook of Membrane Reactors*. Elsevier, 2013, pp. 384–415.
- [62] M. C. Biesinger. *X-ray Photoelectron Spectroscopy (XPS) Reference Pages: Oxygen*. 2021. URL: <https://www.xpsfitting.com/search/label/Oxygen>. (accessed: 30.06.2024).
- [63] Thermo Fisher Scientific. *Table of Elements: Phosphorus*. 2024. URL: <https://www.thermofisher.com/nl/en/home/materials-science/learning-center/periodic-table/non-metal/phosphorus.html>. (accessed: 30.06.2024).
- [64] Toru Yamashita and Peter Hayes. "Analysis of XPS spectra of Fe²⁺ and Fe³⁺ ions in oxide materials". In: *Applied surface science* 254.8 (2008), pp. 2441–2449.

- [65] Abdulmajid Abdallah Mirghni et al. "A high energy density asymmetric supercapacitor utilizing a nickel phosphate/graphene foam composite as the cathode and carbonized iron cations adsorbed onto polyaniline as the anode". In: *RSC advances* 8.21 (2018), pp. 11608–11621.
- [66] Hiroshi Nohira et al. "Characterization of ALCVD-Al₂O₃ and ZrO₂ layer using X-ray photoelectron spectroscopy". In: *Journal of non-crystalline solids* 303.1 (2002), pp. 83–87.
- [67] Thermo Fisher Scientific. *Table of Elements: Oxygen*. 2024. URL: <https://www.thermofisher.com/nl/en/home/materials-science/learning-center/periodic-table/non-metal/oxygen.html>. (accessed: 30.06.2024).
- [68] M. C. Biesinger. *X-ray Photoelectron Spectroscopy (XPS) Reference Pages*. 2021. URL: <https://www.xpsfitting.com/>. (accessed: 01.07.2024).
- [69] Thermo Fisher Scientific. *Table of Elements: Iron*. 2024. URL: <https://www.thermofisher.com/nl/en/home/materials-science/learning-center/periodic-table/transition-metal/iron.html>. (accessed: 30.06.2024).
- [70] M. C. Biesinger. *X-ray Photoelectron Spectroscopy (XPS) Reference Pages: Iron*. 2021. URL: <https://www.xpsfitting.com/search/label/Iron>. (accessed: 30.06.2024).
- [71] L-F Huang et al. "Improved electrochemical phase diagrams from theory and experiment: the Ni–water system and its complex compounds". In: *The Journal of Physical Chemistry C* 121.18 (2017), pp. 9782–9789.
- [72] Samuel C Perry et al. "Pourbaix diagrams as a simple route to first principles corrosion simulation". In: *Journal of the Electrochemical Society* 166.11 (2019), p. C3186.
- [73] Jia Chen and Yongqiang Tian. "Hexavalent chromium reducing bacteria: mechanism of reduction and characteristics". In: *Environmental Science and Pollution Research* 28 (2021), pp. 20981–20997.
- [74] Anne Helmenstine. *Transition Metal Ion Colors*. 2020. URL: <https://sciencenotes.org/transition-metal-ion-colors/>. (accessed: 23.06.2024).



Pourbaix Diagrams

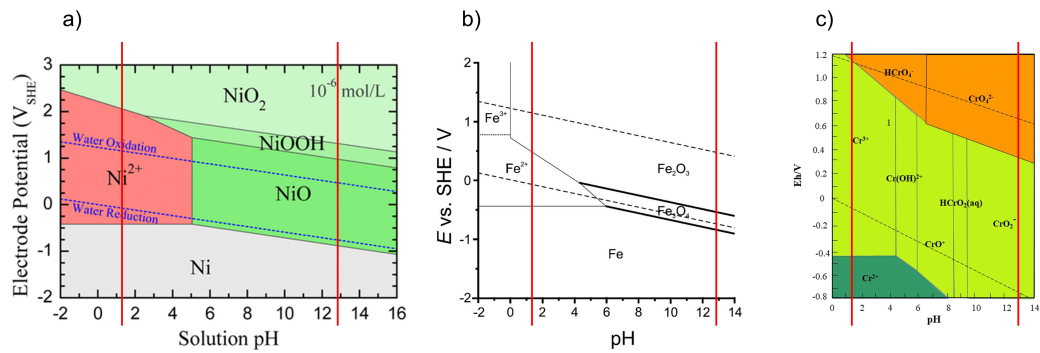


Figure A.1: Pourbaix diagrams of: a) Nickel [71]; b) Iron [72]; c) Chromium [73]. The vertical red bars mark the lowest and highest pH values observed in the anolyte and catholyte, respectively.

B

Testing Protocols

1. Prepare 250 ml of artificial seawater and sodium phosphate buffer for each test anew.
2. Pump each solution through one of the cell flow fields until the first drops appear in the tubing outlets, then reverse the pumping direction to flush it out again. After the first air bubbles appear in the bottles, keep the pump on for sixty extra seconds to ensure that all liquid has been pumped out. This step is for the initial wetting of the cell.
3. Afterwards, detach the bottles from the setup and weigh them. Mark the bottle caps to ensure always measuring the bottle weight with the same cap.
4. Next, reconnect the bottles to the setup and restart the pump so that liquid is pumped continuously through each cell compartment. Let the pump run for 24 hours.
5. After 24 hours, reverse the pumping direction to pump out the solutions and, after the first bubbles appear in the bottles, keep the pump on for another sixty seconds.
6. Finally, disconnect the bottles from the setup and measure the weight again.
7. Attain the solution weight changes by comparing the weight change of each bottle before and after 24 hours of testing.

Figure B.1: Water mass flux testing protocol

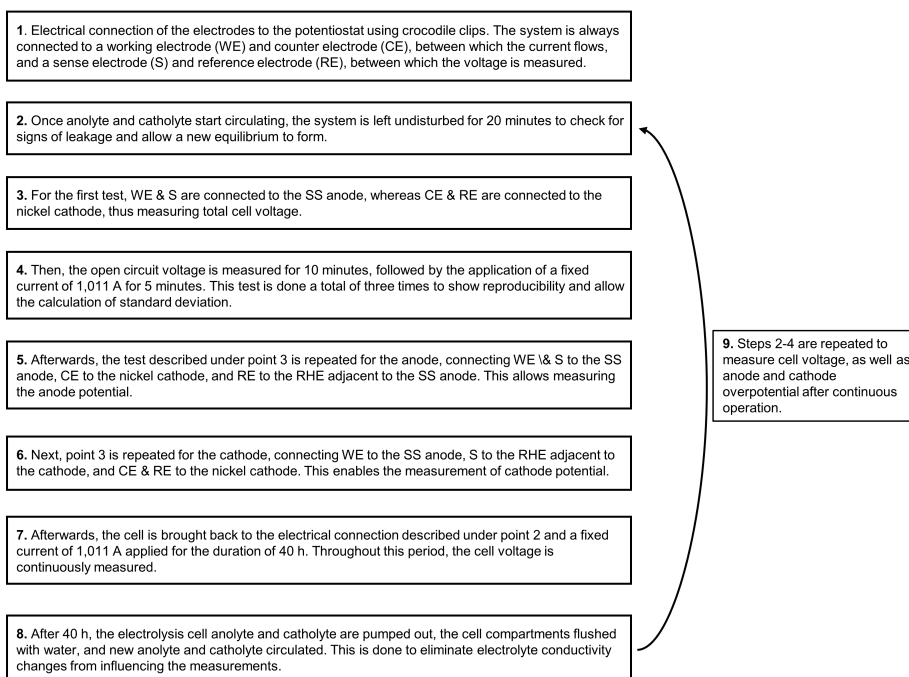


Figure B.2: Galvanostatic electrolysis testing protocol

C

Testing Solutions

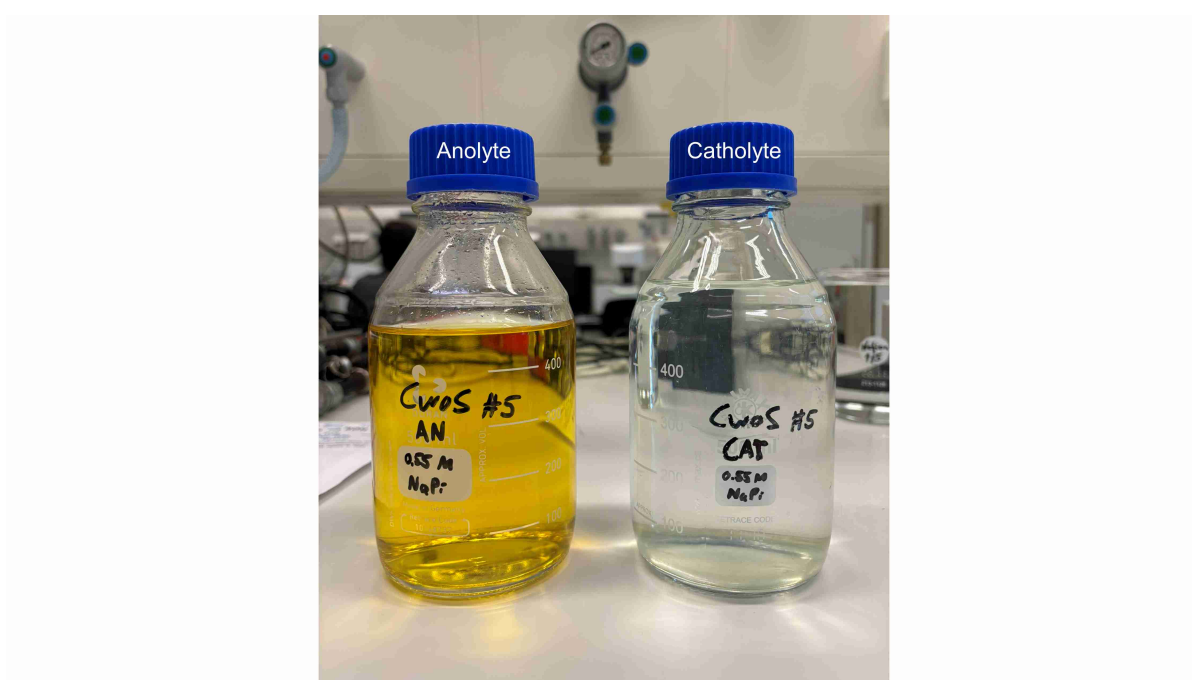


Figure C.1: CwoS LC solutions after 40 h test



Figure C.2: CwoS HC solutions after 40 h test



Figure C.3: CwoS LC solutions after 40 h test



Figure C.4: Cws HC solutions after 40 h test

D

SEM/EDX Locations

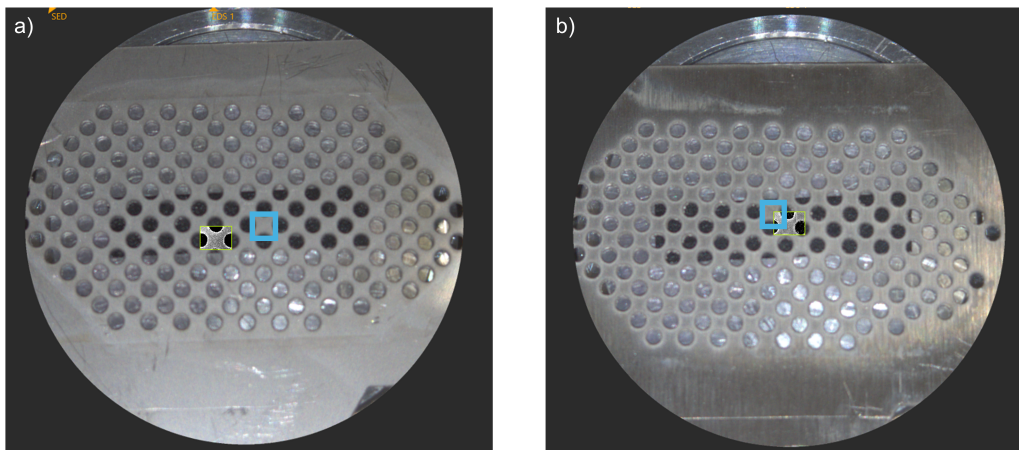


Figure D.1: Blank anode and cathode SEM/EDX locations

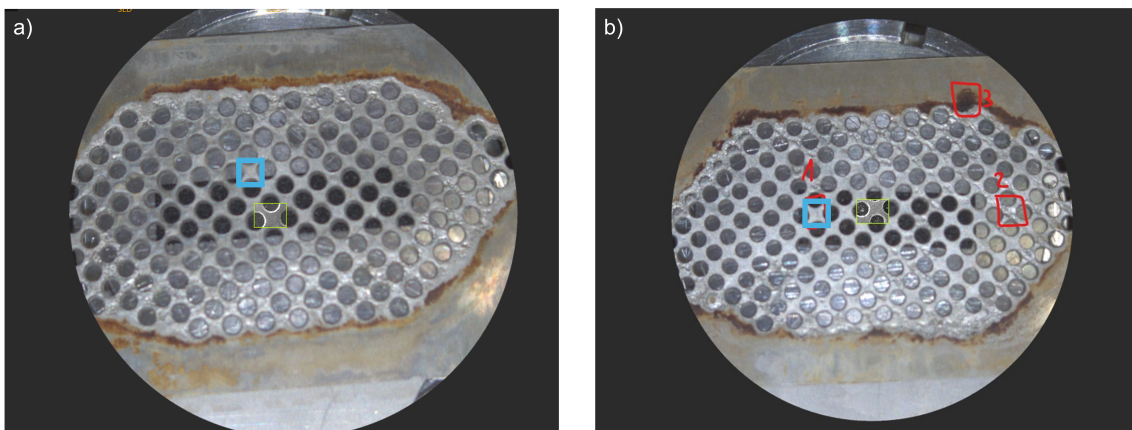


Figure D.2: SEM/EDX locations 'no corrosion' (only the spots marked a blue rectangle)

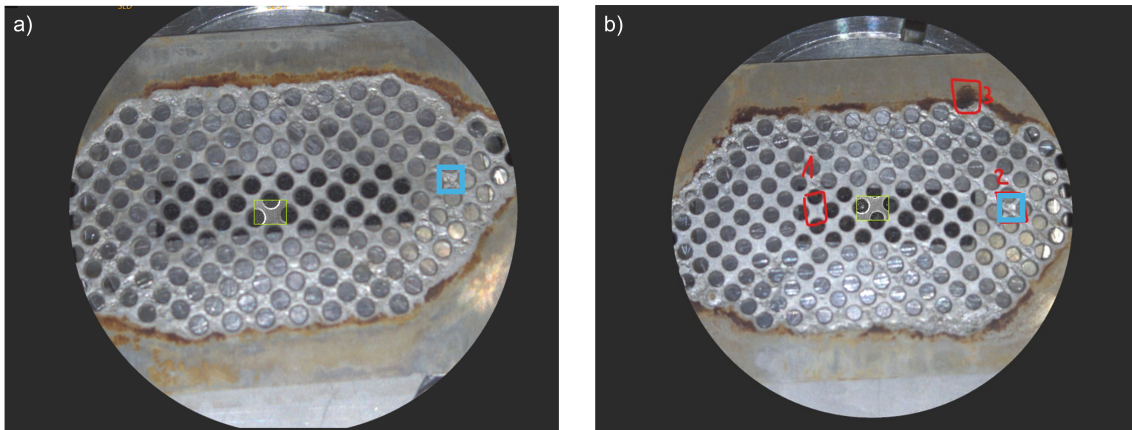


Figure D.3: SEM/EDX locations 'strong corrosion' (only the spots marked a blue rectangle)

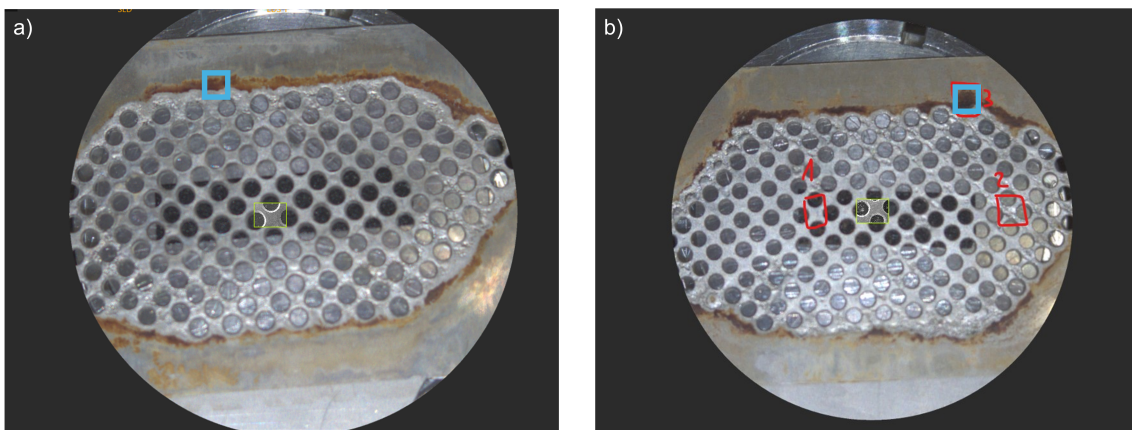


Figure D.4: SEM/EDX locations 'brown precipitate (anode)' (only the spots marked a blue rectangle)

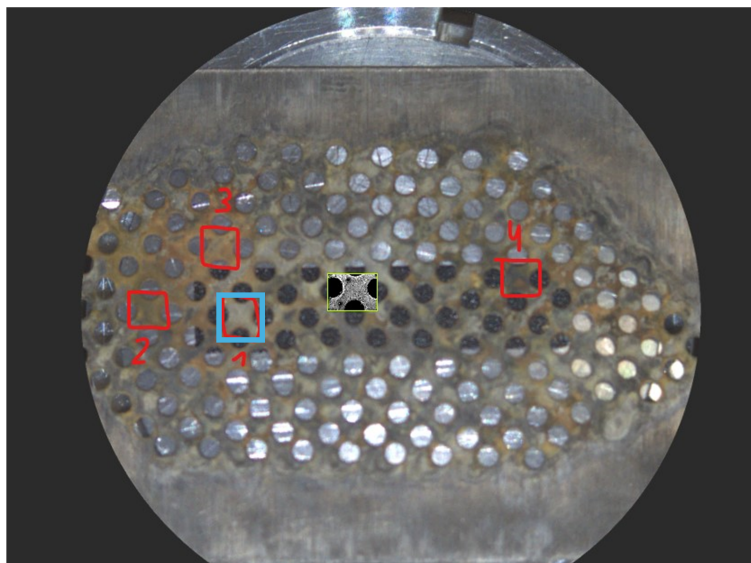


Figure D.5: Cathode SEM/EDX location 'light grey' (only the spots marked a blue rectangle)

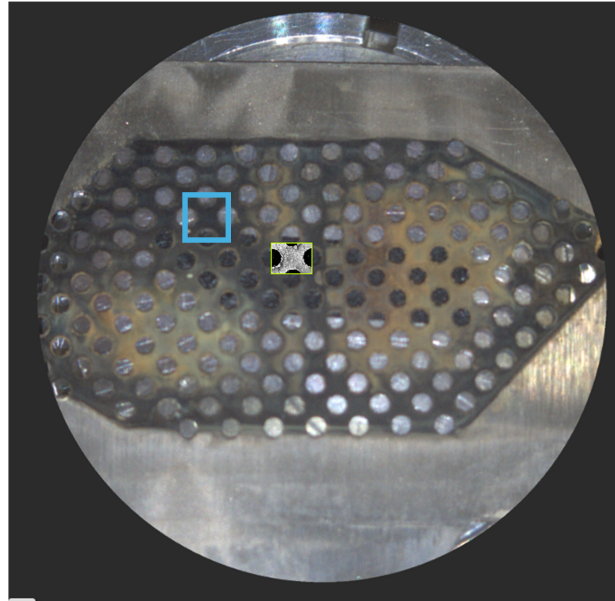


Figure D.6: Cathode SEM/EDX location 'black'

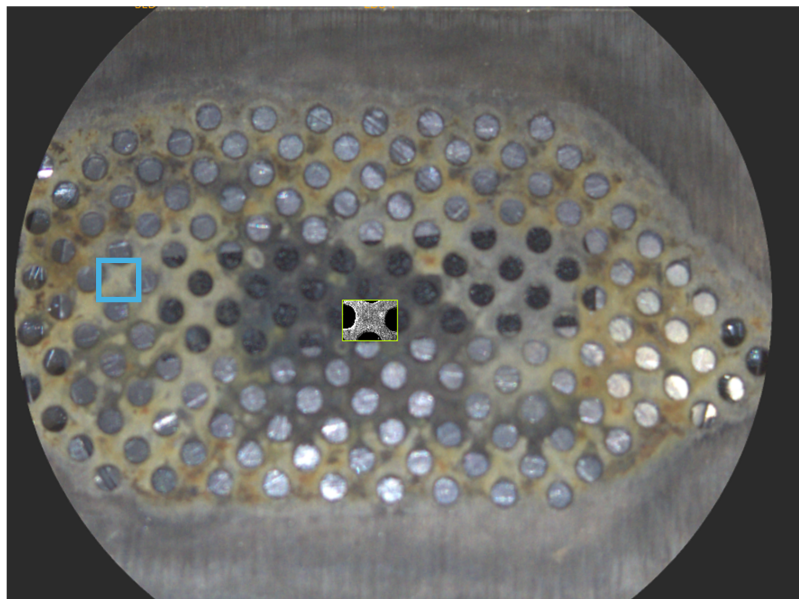


Figure D.7: Cathode SEM/EDX location 'light green'

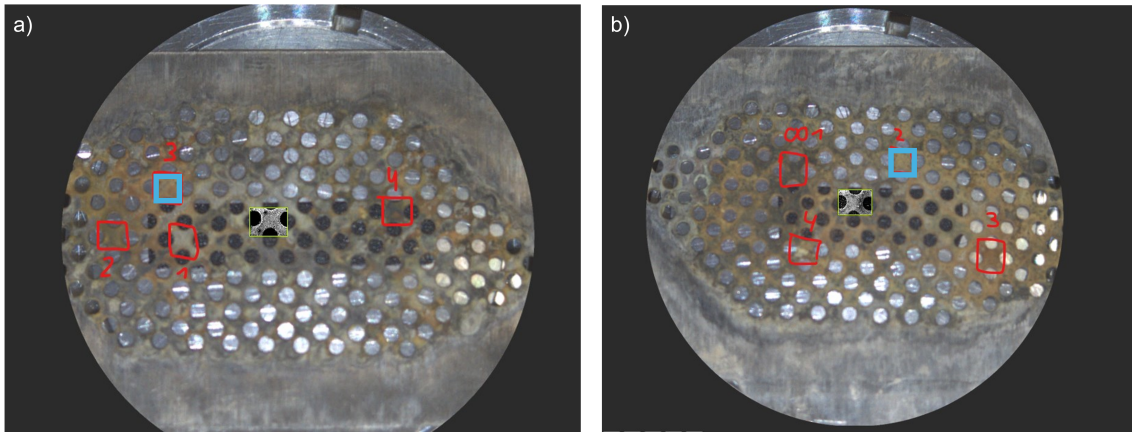


Figure D.8: SEM/EDX locations 'brown precipitate (cathode)' (only the spots marked a blue rectangle)

E

Supplementary Information

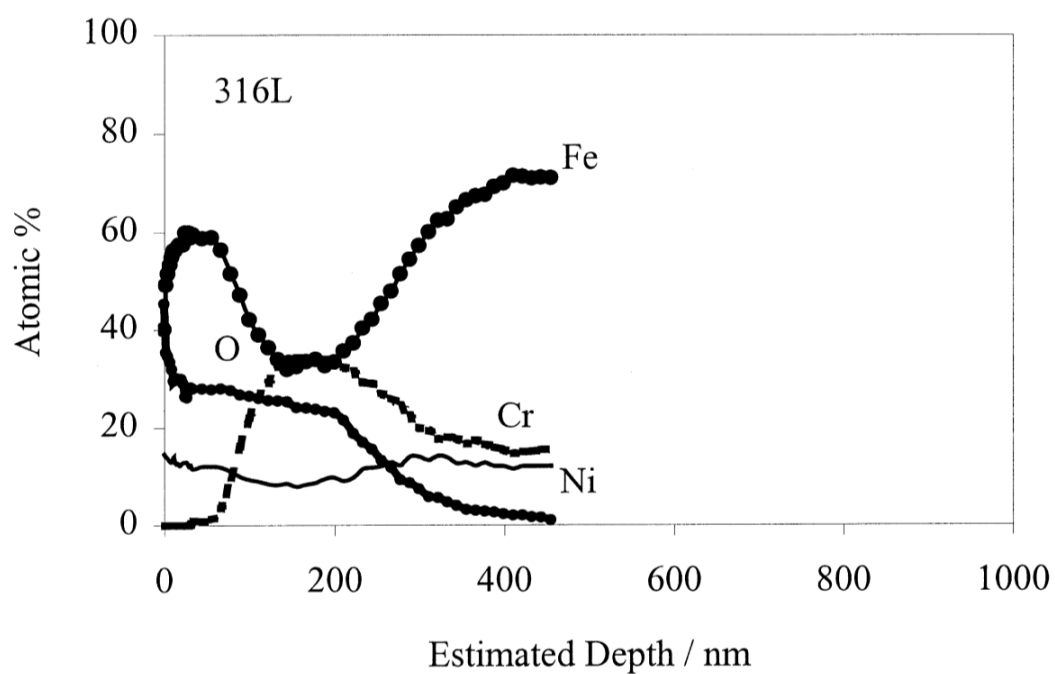


Figure E.1: 316L stainless steel surface composition [43]

Transition Metal Ion Colors in Aqueous Solution

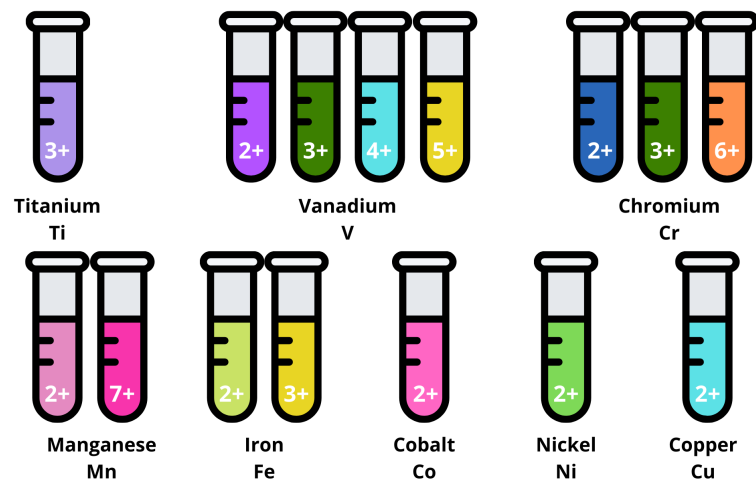


Figure E.2: Transition metal ion colours [74]